

NON-THERMAL PROCESSES ON ICE AND LIQUID MICRO-JET SURFACES

A Thesis
Presented to
The Academic Faculty

by

Babajide O. Olanrewaju

In Partial Fulfillment
of the Requirements for the Degree
Doctor of Philosophy in the
School of Chemistry and Biochemistry

Georgia Institute of Technology
May 2011

NON-THERMAL PROCESSES ON ICE AND LIQUID MICRO-JET SURFACES

Approved by:

Dr. Thomas M. Orlando, Advisor
School of Chemistry and Biochemistry
Georgia Institute of Technology

Dr. Paul H. Wine
School of Chemistry and Biochemistry
Georgia Institute of Technology

Dr. Lawrence A. Bottomley
School of Chemistry and Biochemistry
Georgia Institute of Technology

Dr. Facundo M. Fernandez
School of Chemistry and Biochemistry
Georgia Institute of Technology

Dr. Greg Huey
School of Earth and Atmospheric
Science
Georgia Institute of Technology

Date Approved: 14 January 2011

To my parents,

Koyejo and Adesola Olanrewaju

ACKNOWLEDGEMENTS

I could not have completed my thesis without the consistent support of certain people. I would like to express my deepest gratitude to my advisor, Professor Thomas Orlando, for his invaluable guidance, support and mentorship throughout my graduate school experience. I would like to show extreme gratitude to Dr. Gregory Grieves, Dr. Alexandr Alexandrov and Dr. Christopher Lane for their help. I have benefited immensely from their advice and assistance over the years. I would also like to gratefully thank Dr. Kristin Shepperd, who as a very good friend, always rendered a helping hand and a shoulder to lean on in times of despair. Special thanks goes to other members of the EPICS lab (both present and past); Dr. Jason McLain, Dr. Heather Abbott-Lyon, Dr. Janine Captain, Dr. Haiyan Chen, Dr Yanfeng Chen, Dr. Doogie Oh, Dr. Taishan Fan, Irene Anestis-Richard, Denis Sokolov, Michele Dawley, Michael Poston, Marcus Johnson, Joshua Symonds, Hannah Barks, Kenneth Kite, Lan Sun, Alice Johnson and Torri Rose for their friendship, intellectual conversations and invaluable assistance.

Many thanks go to Dr. Nikolay Petrik and Dr Greg Kimmel for allowing me to work with them at the Pacific Northwest National Laboratory. I would also like to thank other scientists I interacted with during my 15 months stay. I am grateful for the unique and rare opportunity of working with these reputable scientists from different parts of the world.

I have been extraordinarily fortunate to have close friends I can rely on, their friendship has been source of strength through out graduate school and I would be forever indebted to them. I would like to specifically thank Olajide Durosinmi and Frank Onyemauwa for their friendship and help every step of the way.

Lastly, I would like to thank my parents, Desola and Koyejo Olanrewaju without whom the feat of successfully finishing graduate school would have been impossible. It is their love, sacrifice and advice that provides me with the strength to face life challenges including the uncertainties and stress of graduate school. I would also like to thank my siblings, Olaitan, Odunayo and Eniola Olanrewaju for their understanding and corporation during this period away from home. You are all source of joy and encouragement to me.

TABLE OF CONTENTS

DEDICATION	iii
ACKNOWLEDGEMENTS	iv
LIST OF TABLES	viii
LIST OF FIGURES	ix
SUMMARY	xiii
I INTRODUCTION	1
1.1 Low temperature studies of ice	2
1.2 Probing liquids in vacuum	4
II PHOTODISSOCIATION OF METHYL IODIDE ADSORBED ON LOW-TEMPERATURE AMORPHOUS ICE SURFACES	5
2.1 Introduction	5
2.2 Experimental Details	6
2.3 Results	9
2.3.1 Temperature programmed desorption of 0.1 ML CH ₃ I on ice	9
2.3.2 Photodissociation of methyl iodide adsorbed on ice	10
2.4 Discussion	17
2.4.1 Structure of methyl iodide adsorbed on ice and the effect of ice morphology	17
2.4.2 Electronic Structure of CH ₃ I and adsorbed CH ₃ I	19
2.4.3 Photodissociation mechanism	21
2.4.4 I ₂ formation and release	23
2.5 Conclusion	24
III PROBING THE INTERACTION OF HYDROGEN CHLORIDE WITH LOW-TEMPERATURE WATER ICE SURFACES USING THERMAL AND ELECTRON-STIMULATED DESORPTION	25
3.1 Introduction	25
3.2 Experimental Details	26

3.3	Results	29
3.3.1	Cations from ice surfaces containing HCl.	29
3.3.2	H ⁺ kinetic energy distributions with/without HCl.	32
3.3.3	TPD of HCl: Ice at several growth temperatures.	34
3.4	Discussion	37
3.4.1	Mechanisms for cation ESD	37
3.4.2	Mechanism of HCl effects on cation ESD.	39
3.4.3	Temperature programmed desorption	40
3.5	Conclusions	43
IV	PHOTOIONIZATION OF LIQUID WATER AND AQUEOUS SOLUTIONS USING A MICROJET.	45
4.1	Introduction	45
4.2	Experimental Details	47
4.3	Results	51
4.4	Discussion	57
4.4.1	Characterization of liquid jet	57
4.4.2	Ion ejection mechanism	62
4.5	Conclusions	64
V	PHOTOIONIZATION OF LIQUID MICRO-JET CONTAINING ALKALINE EARTH METAL CHLORIDE, MCl₂ (M=Mg²⁺, Ca²⁺, Sr²⁺ and Ba²⁺).	66
5.1	Introduction	66
5.2	Experimental Details	67
5.3	Results	68
5.4	Discussion	73
5.5	Conclusion	76
VI	CONCLUSION	77
	REFERENCES	81

LIST OF TABLES

2.1	Effective temperature of Maxwell Boltzmann distribution with corresponding translational kinetic energy.	17
5.1	Second ionization potentials of alkaline-earth metal.	75

LIST OF FIGURES

2.1	Schematic of UHV chamber designed at the Georgia Institute of Technology.	7
2.2	Diagram of the REMPI-Time-of-flight mass spectrometer experimental setup with the pulse sequence of both the desorption and ionization (REMPI) laser. This setup was used to detect neutral iodine atoms released during the photodissociation of adsorbed methyl iodide on ice.	8
2.3	Temperature programmed desorption of 0.1 L CH ₃ I adsorbed on a) 50 ML of PASW ice b) 50 ML of ASW ice c) trapped between two 50 ML layers of PASW ice. The lower spectrum (d) represents the TPD of 50 ML of PASW ice. The heating rate for all TPD spectra was $\sim 3 \text{ K s}^{-1}$. CH ₃ I was detected as $m/z=142$ for all spectra while H ₂ O was detected as $m/z=18$	10
2.4	Representative TOF mass spectra for iodine photofragments from CH ₃ I adsorbed on a) PASW and b) ASW. Spectra were taken with a 3 μsec interval between the dissociation laser ($\lambda = 290 \text{ nm}$) and REMPI laser. Non-resonant production of I ₂ ⁺ is observed only when CH ₃ I is adsorbed on ASW.	11
2.5	Summation of multiple Maxwell-Boltzmann distributions (solid line) fit to I(² P _{3/2}) TOF data for 0.1 L CH ₃ I adsorbed on 50 ML of a) ASW and b) PASW. Laser light with 290 nm (top panel) and 260 nm (bottom panel) wavelength was used to irradiate the surface. The dotted lines represent the thermal Maxwell-Boltzmann distribution with an effective temperature of 90 K. The dashed lines represent energetic nonthermal components.	13
2.6	Summation of multiple Maxwell-Boltzmann distributions (solid line) fit to I(² P _{1/2}) TOF data for 0.1 L CH ₃ I adsorbed on 50 ML of a) ASW and b) PASW. Laser light with 290 nm (top panel) and 260 nm (bottom panel) wavelength was used to irradiate the surface. The dashed lines represent energetic nonthermal components. Unlike I(² P _{3/2}) TOF data, the dotted lines that represent the thermal Maxwell-Boltzmann distribution is absent.	14
2.7	Maxwell-Boltzmann distributions fit to non-resonant I ₂ TOF data for 0.1 L CH ₃ I adsorbed on ice grown at 130 K (ASW) for both 290 nm and 260 nm.	16
2.8	Desorption pathways of CH ₃ I from amorphous solid water (ASW) and porous amorphous solid water (PASW) ice from amorphous.	19

2.9	Schematic one-dimensional potential energy diagram involved in CH ₃ I A-band photodissociation. Gas phase A-band photo-excitation occurs primarily from the ground state to ³ Q ₀ excited state, however, due to spin-orbit coupling the ³ Q ₀ state mixes with the ¹ Q ₁ state at the curve crossing.	20
3.1	Schematic of UHV chamber used for probing interaction of HCl on ice.	27
3.2	Cations produced and desorbed during 250 eV electron impact of pure (solid line) and HCl (dashed gray line) dosed PASW (bottom panel), ASW (middle panel), and CI (top panel). Upon addition of HCl there is a large decrease in the H ⁺ and H ₂ ⁺ yields and an increase in the cluster yields.	30
3.3	Relative increase in cluster yield with HCl coverage for H ⁺ (H ₂ O) (filled symbols) and H ⁺ (H ₂ O) ₂ (open symbols) for (A) PASW, (B) ASW, and (C) CI.	32
3.4	H ⁺ velocity distribution from pristine (squares) and HCl dosed (circles) (A) CI and (B) ASW ice samples collected under field-free conditions. The dotted and dashed lines in are the Gaussian fit to the fast and slow velocity components for pristine and HCl dosed ice, respectively. The solid lines are the sum of the Gaussian fit which accurately describe the data.	34
3.5	Temperature programmed desorption spectra of HCl dosed on ice at (A) 150 K, (B) 110 K, and (C) 80 K on CI, ASW, and PASW, respectively. The dashed line is the water desorption (divided by 5 for comparison) and the solid line is the HCl desorption. There are three different desorption features seen under the dosing conditions used. All TPD spectra of the samples used in the ESD measurements showed only one desorption feature (I) attributed to an ionized species. . . .	36
4.1	Schematic of a 10 μm liquid jet. The liquid jet (A) is surrounded by a collisional atmosphere (B), the size of which depends upon the jet diameter, and beyond which the number density of evaporating molecules drops as 1/r in a collision free zone (C). The density of B as well as the liquid temperature can be modeled by Clausius-Clapeyron evaporative cooling model. [40]	46
4.2	Custom made liquid jet chamber designed at Pacific Northwest National Laboratory (PNNL). The liquid jet streams downward into a liquid nitrogen cold trap. The liquid jet is adjusted with respect to the focused laser beam in the middle of the repeller and extraction plate of the TOF mass spectrometer to optimize ion yield.	49
4.3	The custom-built Liquid jet Chamber at PNNL with a new time-of-flight optics.	50

4.4	Time-of-flight mass spectrum of ions ejected during photoionization of a) D ₂ O and b) pure water . Cation clusters of the type H ⁺ (H ₂ O) _n and D ⁺ (D ₂ O) _n are observed respectively for H ₂ O and D ₂ O, with n ≤ 6. .	52
4.5	Typical TOF spectrum of ions ejected during photoionization of 10 ⁻⁴ , 10 ⁻³ and 5×10 ⁻³ M NaCl and NaOH. Unsolvated H ₃ O ⁺ and Na ⁺ and both water clusters of the type H ⁺ (H ₂ O) _n and Na ⁺ (H ₂ O) _m are observed (n, m ≤ 6). H ₃ O ⁺ and protonated water clusters decreases with concentration while Na ⁺ and sodium water clusters increases with concentration.	53
4.6	Experimentally observed ion yield as a function of concentration of aqueous NaCl (top panel) and NaOH (bottom panel) solutions. Shown are yields of unsolvated ions: H ₃ O ⁺ and Na ⁺ ; protonated water clusters H ⁺ (H ₂ O) _n , n = 2–4 and sodium water clusters Na ⁺ (H ₂ O) _m , m = 1–3. Both the hydronium ion and protonated water clusters yield varied inversely with increasing concentration while both sodium ion and sodium water clusters yield was proportional to concentration. . .	55
4.7	Experimentally observed H ₃ O ⁺ and H ⁺ (H ₂ O) _n n = 2–5 yields as a function of concentration for aqueous solution of HCl. Unlike aqueous solution of NaCl and NaOH, the protonated water cluster yield remains constant with increasing HCL concentration.	56
4.8	Plots of the ratio of unsolvated hydronium ion (H ₃ O ⁺) and the sum of measurable protonated water clusters as a function of concentration for HCl (solid square), NaCl (solid circle) and NaOH (open circle). Each data set represents H ₃ O ⁺ / ΣH ⁺ (H ₂ O) _n for >2. While the yield of both H ₃ O ⁺ and protonated water cluster decreases with concentration, their ratios increases with concentration for both NaOH and NaCl but remains constant for HCl solutions(dashed lines serve as guides). . . .	57
4.9	a) Intensities of unsolvated H ₃ O ⁺ ejected from photoionization of pure water (solid circle) and 5×10 ⁻³ M NaCl (open circle); and bare Na ⁺ (open square) ejected from the photoionization of 5×10 ⁻³ M NaCl plotted as a function of the distance between the centers of the focused laser beam and the liquid jet. Other water clusters have similar trends. b) Schematic of the effective overlap of the liquid jet (~ 6μm) and the focused laser beam (~ spot size 35 μm).	59
4.10	Power dependence measurement. a) Ion yield for each ion, H ₃ O ⁺ (open circle), H ⁺ (H ₂ O) ₂ (solid circle) and H ⁺ (H ₂ O) ₃ (open square) plotted as a function of laser power; a threshold exists around 100μJ. b) Log-log plot with a slope of 2.	62
4.11	Mechanism for photoejection of water clusters from aqueous solutions of NaCl and NaOH.	64

5.1	Time-of-flight mass spectrum of ions ejected during photoionization of MgCl ₂ solution a) 10 ⁻⁴ M; b) 10 ⁻³ M; c) 5×10 ⁻³ M and d) 10 ⁻² M. Cation clusters of the type H ⁺ (H ₂ O) _n (n = 1–6) MgOH ⁺ (H ₂ O) _m (m = 0–4) and Mg ⁺ (H ₂ O) _x (x=1,2) are observed.	69
5.2	Time-of-flight mass spectrum of ions ejected during photoionization of CaCl ₂ solution a) 10 ⁻⁴ M; b) 10 ⁻³ M; c) 5×10 ⁻³ M and d) 10 ⁻² M. Cation clusters of the type H ⁺ (H ₂ O) _n (n = 1–6) and CaOH ⁺ (H ₂ O) _m (m = 0–4) are observed.	70
5.3	Time-of-flight mass spectrum of ions ejected during photoionization of SrCl ₂ solution a) 10 ⁻⁴ M; b) 10 ⁻³ M; c) 5×10 ⁻³ M and d) 10 ⁻² M. Cation clusters of the type H ⁺ (H ₂ O) _n (n = 1–4) and SrOH ⁺ (H ₂ O) _m (m = 0–7) are observed.	71
5.4	Time-of-flight mass spectrum of ions ejected during photoionization of BaCl ₂ solution a) 10 ⁻⁴ M; b) 10 ⁻³ M; c) 5×10 ⁻³ M and d) 10 ⁻² M. Cation clusters of the type H ⁺ (H ₂ O) _n (n = 1–4) and BaOH ⁺ (H ₂ O) _m , (m = 0–7) are observed.	72
5.5	The relative yield of M ⁺ compared to MOH ⁺ . Mg gives mainly Mg ⁺ with a small MgOH ⁺ . Approximately equal amount of M ⁺ and MOH ⁺ are observed for both Ca and Sr while Ba yields mainly BaOH ⁺ and a considerably small amount of Ba ⁺ . This trend appears to be independent of the salt concentration.	73

SUMMARY

The primary focus of this research is to investigate non-thermal processes occurring on ice surfaces and the photo-ejection of ions from liquid surfaces. Processes at the air-water/ice interface are known to play a very important role in the release of reactive halogen species with atmospheric aerosols serving as catalysts. The ability to make different types of ice with various morphologies, hence, different adsorption and surface properties in vacuum, provide a useful way to probe the catalytic effect of ice in atmospheric reactions. Also, the use of the liquid jet technique provides the rare opportunity to probe liquid samples at the interface; hitherto impossible to investigate with traditional surface science techniques.

In Chapter 2, the effect of ice morphology on the release of reactive halogen species from photodissociation of adsorbed organic halides on ice will be presented. Quantum state resolved measurements of neutral atomic iodine from the photon irradiation of submonolayer coverages of methyl iodide adsorbed on low temperature water ice were conducted. Temperature programmed desorption (TPD) studies of methyl iodide adsorbed on ice were performed to provide information on the effect of ice morphology on the adsorption of submonolayer methyl iodide.

The interaction and autoionization of HCl on low-temperature (80–140 K) water ice surfaces has been studied using low-energy (5–250 eV) electron-stimulated desorption (ESD) and temperature programmed desorption (TPD). A detailed ESD study of the interactions of low concentrations of HCl with low-temperature porous amorphous solid water (PASW), amorphous solid water (ASW) and crystalline ice (CI) surfaces will be presented in Chapter 3. The ESD cation yields from HCl adsorbed

on ice, as well as the coverage dependence, kinetic energy distributions and TPD measurements were all monitored.

Probing liquid surface using traditional surface science technique is usually difficult because of the problem of keeping the liquid surface clean and the distortion of information by the interference of equilibrium dense vapor above the liquid. By using the liquid jet technique the ejection of ions from surface of micron sized liquid can be adequately probed with a linear time-of-flight mass spectrometer. The photoionization of pure water and aqueous solutions of NaOH, NaCl and HCl is presented in Chapter 4. The aim of this investigation was to provide a fundamental understanding of the structure of water/vacuum interfaces. In Chapter 5, the ejection of ions from salt solutions containing divalent cations is also presented. The goal of the experiment was to figure out the solvation structure and reaction dynamics of divalent metal ions, M^{2+} on the surface of aqueous solution. A lot of work has been done in the gas phase either by a pickup-type cluster source or by collision induced dissociation of ejected ions from electrospray. For the first time the direct monitoring of ions ejected from liquid into gas phase is explored. Possible ejection mechanisms for the ejection of cations are discussed extensively in both Chapters 4 and 5.

The results presented in this thesis is a combination of experiments performed at the Georgia Institute of Technology and the Pacific Northwest National Laboratory (PNNL) which includes experiments on ice and micro-jet respectively. The results in Chapters 2 and 3 have been submitted to the Journal of Chemical Physics and the Journal of Physical Chemistry respectively. It is important to note that the data presented in Chapter 3 was originally taken by Dr Janine Herring-Captain as part of her thesis work. It is also presented in this thesis due to effort in analyzing the data and preparation of the submitted manuscript. Chapter 4 and 5 represents papers which will also be submitted for publication in the open scientific literature. All the work leading to the results presented in these two chapters were done during my

visit to PNNL and I would like to acknowledge that the instrumentation and data acquisition were done in collaboration with Nikolai Petrik and Greg Kimmel.

CHAPTER I

INTRODUCTION

Heterogeneous processes on both ice [1-4] and liquid water interfaces [5] play very important roles in atmospheric chemistry. Important atmospheric reactions such as the hydrolysis of SO_2 [6-8] and the reaction of ClONO_2 with HCl [9] occur on the surfaces of atmospheric aerosols. The presence of atmospheric surfaces such as polar stratospheric clouds (PSCs) provide alternative reaction pathways compared to the gas phase for the photolysis of chlorine-containing species involved in stratospheric ozone depletion.[10] Reactive halogen species involved in tropospheric ozone depletion episodes during Polar Sunrise are also known to be formed from either adsorbed halogenated hydrocarbon on ice surfaces or sea salt aerosols. [11] For all of the aforementioned reactions and other relevant atmospheric reactions, the reactivity of gases is strongly influenced by the surface properties of the ice and liquid aerosols. However, despite the ease of obtaining information on the bulk properties (such as pH and solute concentration) of multiphase systems found in the atmosphere, developing a model surface with well defined composition and structure is always difficult. Studies of reactions on both ice and liquid surfaces at ambient conditions are usually complicated by the rapid desorption and adsorption processes due to the high evaporation rates at the surface. To develop a better understanding and improve modeling of several atmospheric relevant reactions, it is important to develop laboratory techniques that provide an opportunity to investigate non-thermal reactions on both ice and liquid surfaces. The focus of this research is to investigate the adsorption of molecules, solvation of ions and the non-thermal processes at the surfaces of ice and aqueous solutions.

1.1 *Low temperature studies of ice*

Quantitative understanding of how the air-ice interface influences important atmospheric reactions is critical in developing relevant models for the prediction of important global atmospheric changes. Low temperature ice studies provide insight into the interactions of adsorbates on ice surfaces.[12] The decrease in evaporation rates of the ice permits detailed investigations of how the bulk properties of ice affects the interaction of molecules on its surface, albeit at temperatures lower than that observed in the atmosphere. Extensive studies have been done on the reactions of atmospheric relevant molecules on water ice at low temperature in ultrahigh vacuum (UHV) conditions. These interactions on ice have been investigated using different techniques such as temperature programmed desorption (TPD),[13-15] electron stimulated desorption (ESD),[16] X-ray photoelectron spectroscopy (XPS) [17, 18] and reflection absorption infrared absorption spectroscopy (RAIRS). [19, 20] These studies show that the adsorption, bulk diffusion and desorption of adsorbed molecules depend largely on the morphology of the ice substrate.

Ice grown in vacuum can exist in different structural forms depending on the temperature of the cold substrate.[21] Deposition of water vapor at substrate temperatures below 130 K results in the formation of low density porous amorphous ice (PASW) while dosing water vapor at higher temperatures (≥ 130 K) results in formation of amorphous solid water (ASW). Another form of ice, crystalline ice, is formed by dosing water vapor at temperature ≥ 140 K. Porous amorphous solid water (PASW) and amorphous solid water (ASW) grown at 90 K and 130 K, respectively, are both used in this study. The PASW, unlike ASW, is known to be porous with a high density surface defects that facilitate trapping of adsorbates in the bulk of the ice films.[22]

The adsorption, desorption and photodissociation dynamics of alkyl halides on the surface of ice are relevant to the understanding ozone depletion episodes in both the

stratosphere and marine boundary layers. The investigation of organic compounds such as alkyl halides adsorbed on the surface of ice films in ultrahigh vacuum environments provide information on the various degree of interaction of the adsorbate molecules with dangling OH bonds on the surface of ice.[20] Previous studies also reveal the effect of ice morphology on the photochemistry of trapped alkyl halides in ice. [14] These alkyl halide molecules are weakly bound to the surface of the ice because of the dipole-dipole coupling between the alkyl halide molecules and the water molecules. As shown in Chapter 2, the reactive halogen species released during photon irradiation depend on the interactions of the adsorbed alkyl halide molecules with the ice surface.

PSC surfaces are known to create reaction pathways that enhance ozone depletion episodes in the stratosphere.[10] A critical unknown factor in these reactions is the extent of ionization of HCl molecules adsorbed on PSC. Kang et al. used reactive ion scattering (RIS) and low energy secondary ion mass spectrometry (SIMS) to measure the extent of ionization as a function of temperature and found mostly molecular HCl at temperatures below 70 K, a mixture of the ionized and molecular forms of HCl from 90–120 K, and complete ionization above 140 K.[23] Molecular beam experiments [24] and temperature programmed desorption (TPD) [25-28] have found two types of HCl adsorption at temperatures between 100–170 K, assigned as molecular HCl adsorption and a second ionized or hydrated species. Spectroscopic studies shows evidence of complete ionization at 80 K on ice films,[29, 30] while others report molecular bands that exist up to 125 K.[31] In addition, the kinetics and rate of adsorption of HCl on ice have been investigated as function of the ice phase.[32] Despite these reported findings, the controversy surrounding the molecular and ionic states of HCl on ice still prevails and extensive work is required to understand the chemical state of HCl on ice.

1.2 *Probing liquids in vacuum*

Unlike probing reactions on ice surfaces, investigating air/liquid interfaces present several challenges. This is because traditional surface science techniques require an ultra high vacuum environment to prevent distortion of information due to interference from equilibrium vapor above the liquid surface during data acquisition. In order to circumvent this problem, Faubel et al. developed the liquid jet technique for introducing a continuous micron-sized liquid jet in vacuum.[33-35] The liquid jet technique also facilitates the direct study of continually renewed liquid surfaces in high vacuum, thereby preventing the constant changing of the properties and composition of the liquid surface due to the aging process (diffusion of impurities or liquid constituent). With the liquid jet technique, traditional surface science techniques such as ultraviolet photoelectron spectroscopy (UPS) [36-38] and X-ray spectroscopy (XPS) [39-41] have been used to investigate liquids in an ultrahigh vacuum environment. The liquid jet technique is also valuable for laser ionization of liquid surfaces in vacuum, and has been employed to examine the gas-liquid interface of organic solutions. [42-45] Monitoring ejected ions from UV laser ionization of liquid jets with time of flight mass spectrometry was pioneered by Kondow and co-workers.[44] However, this body of work was done exclusively on solutions of relatively high concentration and on organic solvents. The primary focus of this research is to investigate the photo-ejection of ions from pure water and aqueous salt solutions. In particular, the ions ejected during laser irradiation ($\lambda = 193$ nm) of liquid jet containing aqueous solutions of NaCl, NaOH, HCl and MCl_2 ($M=Mg^{2+}$, Ca^{2+} , Sr^{2+} and Ba^{2+}) were monitored using a linear time-of-flight mass spectrometer.

CHAPTER II

PHOTODISSOCIATION OF METHYL IODIDE ADSORBED ON LOW-TEMPERATURE AMORPHOUS ICE SURFACES

2.1 *Introduction*

Extensive work has been done on photodissociation studies of both gas phase [46-54] and adsorbed methyl iodide (CH_3I) on different solid substrates.[55-64] This wealth of information, and the recent discovery of iodine containing organic compound as the source of reactive halogen species during the ozone depletion processes,[11] has renewed interest in the investigation of photodissociation studies of methyl iodide adsorbed on ice. The surface enhanced catalytic effect of ice (snow) during ozone depletion is believed to be the long sought link in understanding the mechanism involved in the initial release of reactive halogen species.[65] However some questions remain unresolved, the possible mechanism for the direct release of reactive halogen species involved in ozone depletion episodes at polar sunrise is not fully understood. Other questions include the quantum yield of these reactive halogen species and how factors like radiation and ice morphology affect the uptake and release of reactive halogen species.

The present study is designed to provide information on the state resolved measurement of the ground state $\text{I}(^2\text{P}_{3/2})$ and excited state $\text{I}(^2\text{P}_{1/2})$ photofragments released during photodissociation of methyl iodide adsorbed on ice. With the present experimental setup, wavelengths within (290 nm) and outside (260 nm) the actinic flux are used to irradiate the CH_3I adsorbed on ice. TPD is used to probe the general structure and coverage of methyl iodide adsorbed on ice.

2.2 *Experimental Details*

The UHV chamber used is shown in Figure 2.1 and operates at a base pressure of 5.0×10^{-10} Torr and it is equipped with a rotatable, polycrystalline zirconia substrate (99.94 % purity) and a dosing system consisting of two leak valves coupled to a differentially pumped dosing manifold. The chamber is equipped with a linear time of flight mass spectrometer (ToF-MS) for neutral atomic and molecular fragment detection using resonance enhanced multiphoton ionization (REMPI). The system is also equipped with and a quadrupole mass spectrometer (QMS) to analyze desorbing species during temperature programmed desorption (TPD) analysis. The temperature of the zirconia substrate can be varied from 90 K to 900 K via liquid nitrogen cooling and resistive heating. The temperature is monitored with a type-K thermocouple attached to the substrate.

Prior to deposition, de-ionized water was subjected to several freeze-pump-thaw cycles. High purity (99.5 %) CH_3I was also passed through liquid nitrogen traps to remove any possible condensable contaminants. To prevent mixing of the adsorbates before deposition, two separate effusive dosing systems were used for dosing interested gases into the vacuum chamber. The surface of the polycrystalline zirconium substrate is cleaned by flash heating to 900 K and then cooling back down to 90 K. This annealing process removes any chemisorbed iodine atoms and other contaminants from the surface of the substrate. All experiments were done with approximately 50 ML of ice, assuring that interactions associated with the polycrystalline zirconia substrate are removed or minimized. The 50 ML of ice were deposited by background dosing water vapor at 5.0×10^{-8} Torr for 17 minutes with a backing pressure of approximately 1 Torr. Methyl iodide was adsorbed on porous amorphous solid water (PASW) grown at 90 K and on amorphous solid water (ASW) grown at 130 K. The ice temperature was then kept at 90 K to achieve a sticking coefficient close to unity for CH_3I and submonolayer coverages were deposited by dosing the vapor at 1×10^{-8}

Torr for 10 seconds. For TPD experiments, the substrate was heated linearly using a rate of 3 K/s and the desorbing neutrals were monitored by QMS.

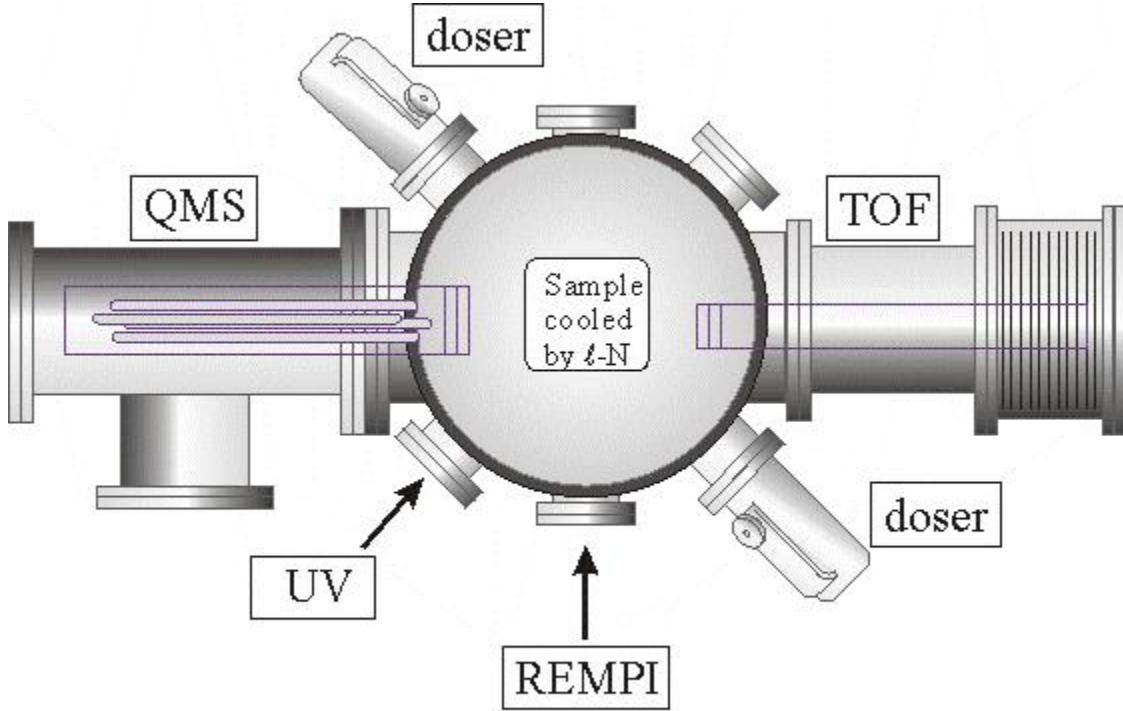


Figure 2.1: Schematic of UHV chamber designed at the Georgia Institute of Technology.

For the state resolved measurements, a plume of neutrals are created by irradiating the methyl iodide adsorbed on ice with either a 290 or 260 nm laser beam generated by frequency doubling the output of a Nd:YAG (yttrium aluminum garnet) master oscillator power oscillator (MOPO) with a barium borate (β -BBO) doubling crystal. To ensure a single photon process, a defocused laser beam ($6 \mu\text{J}/\text{pulse}$) was used to irradiate the sample. Both ground and excited state atomic iodine species can then be detected by focusing a tunable pulsed laser beam ($\sim 1 \text{ mm}$) above and parallel to the surface as shown in Figure 2.2. The ground state $\text{I}(^2\text{P}_{3/2})$ and excited state of neutral iodine $\text{I}(^2\text{P}_{1/2})$ were detected using the $\text{I}(6\text{p}[3]_{5/2} \leftarrow 5\text{p}^2\text{P}_{3/2})$ at 304.67 nm

and $I(6p[1]_{3/2} \leftarrow 5p^2P_{1/2})$ at 305.57 nm (2+1) REMPI schemes, respectively.[66] The laser wavelength required for this detection scheme was generated by frequency doubling the output of a Nd:YAG pumped dye laser with a potassium dehydrate phosphate (KDP) crystal. The typical pulse energies were ~ 1.5 mJ/pulse.

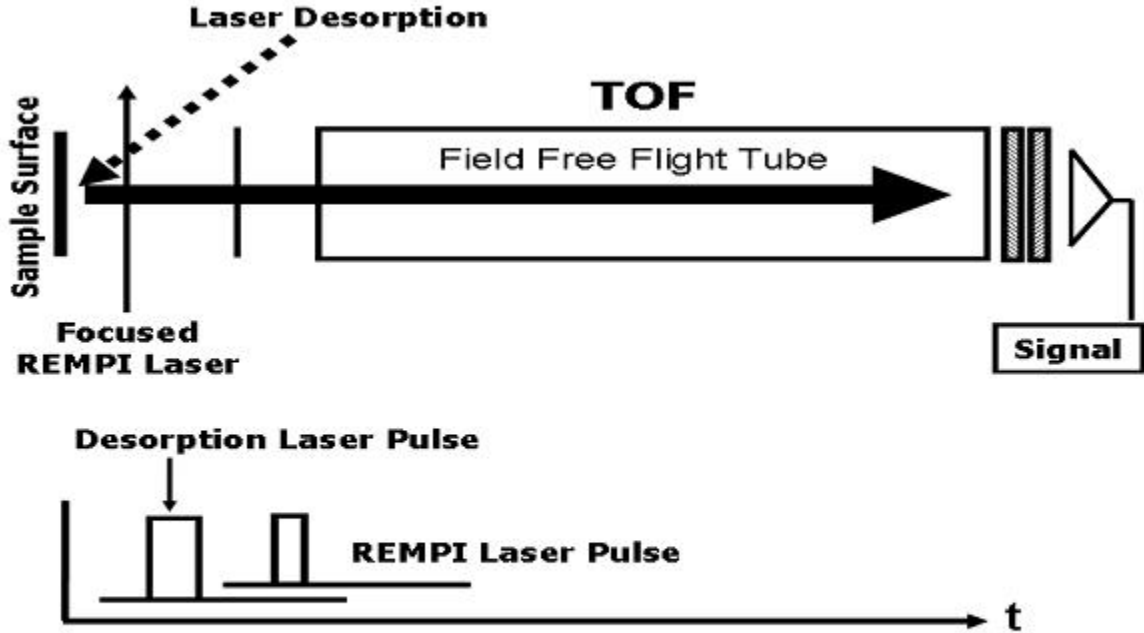


Figure 2.2: Diagram of the REMPI-Time-of-flight mass spectrometer experimental setup with the pulse sequence of both the desorption and ionization (REMPI) laser. This setup was used to detect neutral iodine atoms released during the photodissociation of adsorbed methyl iodide on ice.

TPD studies of CH_3I adsorbed on ice were performed in the same UHV chamber to provide information on the coverage and the affect of ice morphology on the adsorption of submonolayer CH_3I . Using the REMPI scheme described above, the quantum state resolved velocity distribution of the desorbing neutral iodine photofragments was detected by varying the delay time between the photodissociating laser pulse and the

ionization laser pulse as shown in Figure 2.2. This technique was used for determining the quantum states of iodine. All velocity distributions reported were acquired at 200 ns delay increments.

2.3 Results

2.3.1 Temperature programmed desorption of 0.1 ML CH₃I on ice

Figure 2.3a shows TPD spectra of 0.1 ML CH₃I adsorbed on PASW with three desorption states at 120 K, 150 K and 160 K. For methyl iodide adsorbed on ASW, the TPD spectrum (Figure 2.3b) shows one desorption state at 120 K. A comparison of the two TPD spectra shows that in case of ASW, all methyl iodide desorbed before water. In both cases, the desorption state corresponding to multilayer formation at 130 K is negligible.[16] At this coverage, this implies that there is limited amount of clustering of the methyl iodide molecules on the surface of ice. However, in the case of PASW it appears that the CH₃I may adsorb into the pores and possibly become trapped. To test this, the TPD of CH₃I deposited on a 25 ML film of PASW and then capped with a 25 ML overlayer of PASW is shown in figure 2.3c. The trapped methyl iodide in 50 ML of PASW has the same desorption states at 150 K and 160 K as methyl iodide adsorbed on PASW, however, no feature was observed at 120 K. The feature at 150 K corresponds to rapid release of trapped CH₃I during the crystallization of amorphous ice. This molecular volcano effect has been described in detail by others using trapped CCl₄ in ice.[67] As shown in Figure 2.3d, the small feature in the CH₃I TPD at 160 K corresponds to the desorption of amorphous ice.

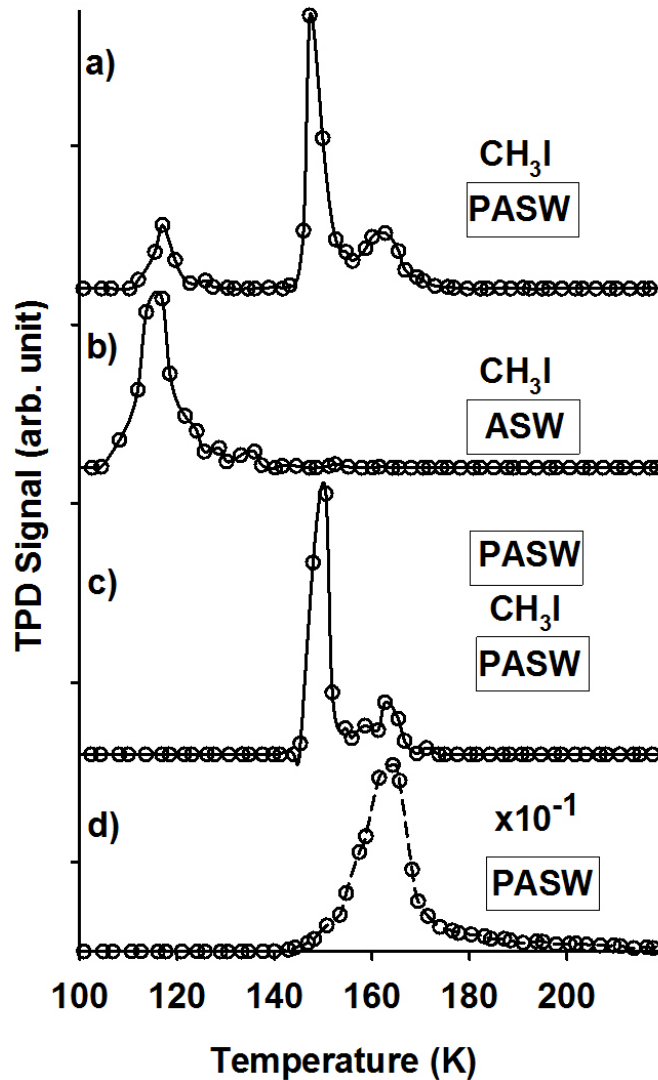


Figure 2.3: Temperature programmed desorption of 0.1 L CH_3I adsorbed on a) 50 ML of PASW ice b) 50 ML of ASW ice c) trapped between two 50 ML layers of PASW ice. The lower spectrum (d) represents the TPD of 50 ML of PASW ice. The heating rate for all TPD spectra was $\sim 3 \text{ K s}^{-1}$. CH_3I was detected as $m/z=142$ for all spectra while H_2O was detected as $m/z=18$.

2.3.2 Photodissociation of methyl iodide adsorbed on ice

A typical time-of-flight mass spectrum obtained from ionization of neutral atomic or molecular iodine released after laser irradiation of adsorbed CH_3I on ice is shown in

Figure 2.4. Both ground state $I(^2P_{3/2})$ and excited state $I(^2P_{1/2})$ iodine photofragments were observed using both 260 and 290 nm photodissociation wavelengths. Typically, these were the only products detected using the 304.67 and 305.57 nm REMPI wavelengths. However as shown in Figure 2.4, for the case of CH_3I adsorbed on ASW, formation of I_2 was also detected as I_2^+ via non-resonant ionization. The I_2^+ formation is referred to as non-resonance because the signal is independent of the wavelength of the ionization laser. In other words, the I_2^+ signal observed by using 304.67 nm REMPI wavelength is also observed when a non-resonant wavelength (for example 305 nm) is used. It is important to point out that the non-resonant I_2^+ yield is approximately two times higher when 260 nm is used for dissociation compared to 290 nm (data not shown).

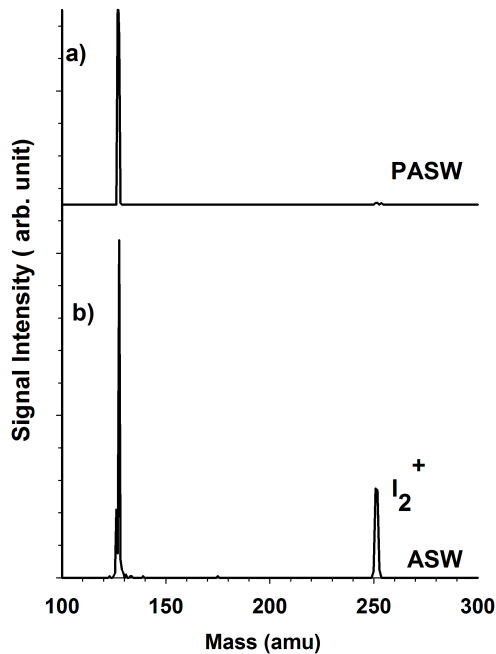


Figure 2.4: Representative TOF mass spectra for iodine photofragments from CH_3I adsorbed on a) PASW and b) ASW. Spectra were taken with a 3 μ sec interval between the dissociation laser ($\lambda = 290$ nm) and REMPI laser. Non-resonant production of I_2^+ is observed only when CH_3I is adsorbed on ASW.

The time of flight distribution (ToF) for $I(^2P_{3/2})$ and $I(^2P_{1/2})$ photofragments obtained during photodissociation are shown in Figures 2.5 and 2.6 respectively. The time-of-flight spectra have been normalized for the sake of comparison and have been fit using the Maxwell-Boltzmann expression

$$I(t) = C_1 t^{-3} \exp \left[-\frac{m}{2kT_1} \frac{d^2}{t^2} \right] + C_2 t^{-3} \exp \left[-\frac{m}{2kT_2} \frac{d^2}{t^2} \right] \quad (1)$$

The fitting procedure to this Maxwell-Boltzmann expression has been previously described in [68]. The time-of-flight data is fit to multiple components where C_1 and C_2 are proportionality constants, T_1 and T_2 are the effective temperatures, m is the mass of the desorbing neutral fragment, d is the distance from the surface to the laser beam, k is the Boltzmann constant, and t is the delay time between the electron beam and laser beam. Though the fits in figures 2.5 and 2.6 to multiple distributions are not unique, these empirical fits demonstrate the complexity of the photodissociation event and subsequent desorption trajectories. The least number of distributions was employed to yield the best overall fit to the experimental spectra.

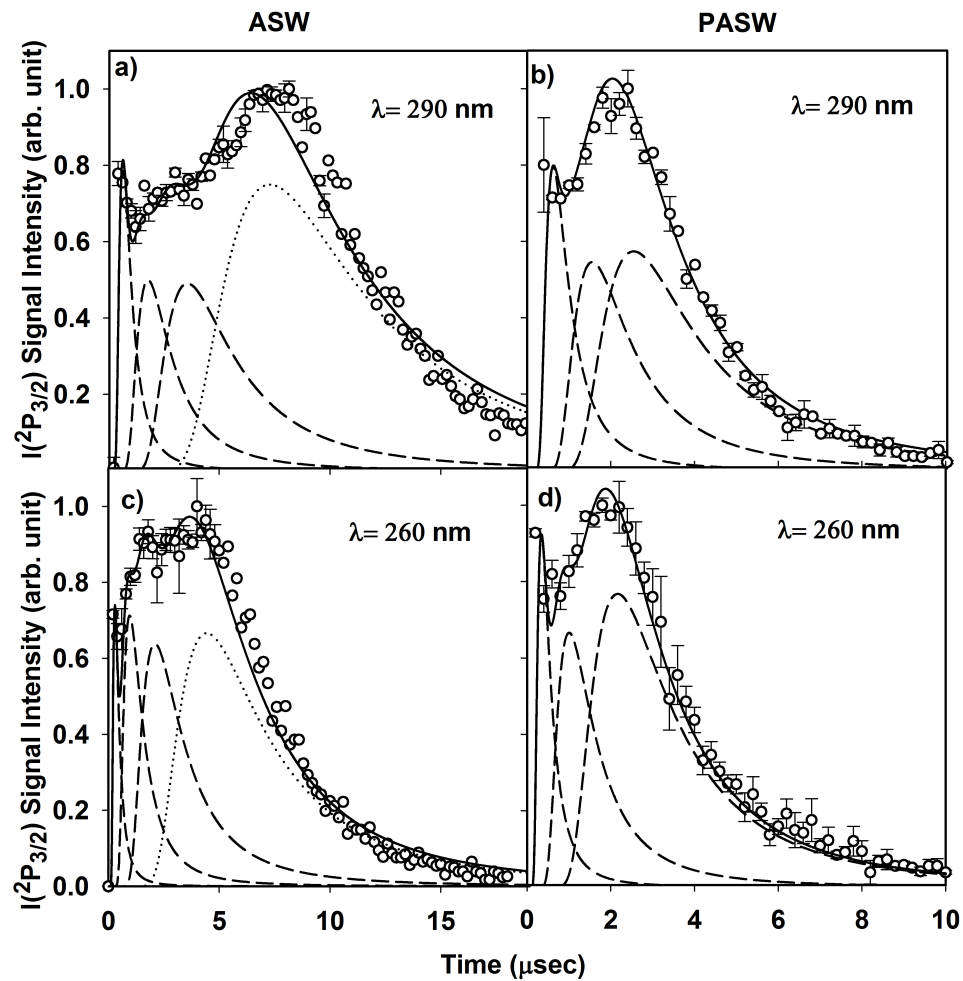


Figure 2.5: Summation of multiple Maxwell-Boltzmann distributions (solid line) fit to $I(^2P_{3/2})$ TOF data for 0.1 L CH_3I adsorbed on 50 ML of a) ASW and b) PASW. Laser light with 290 nm (top panel) and 260 nm (bottom panel) wavelength was used to irradiate the surface. The dotted lines represent the thermal Maxwell-Boltzmann distribution with an effective temperature of 90 K. The dashed lines represent energetic nonthermal components.

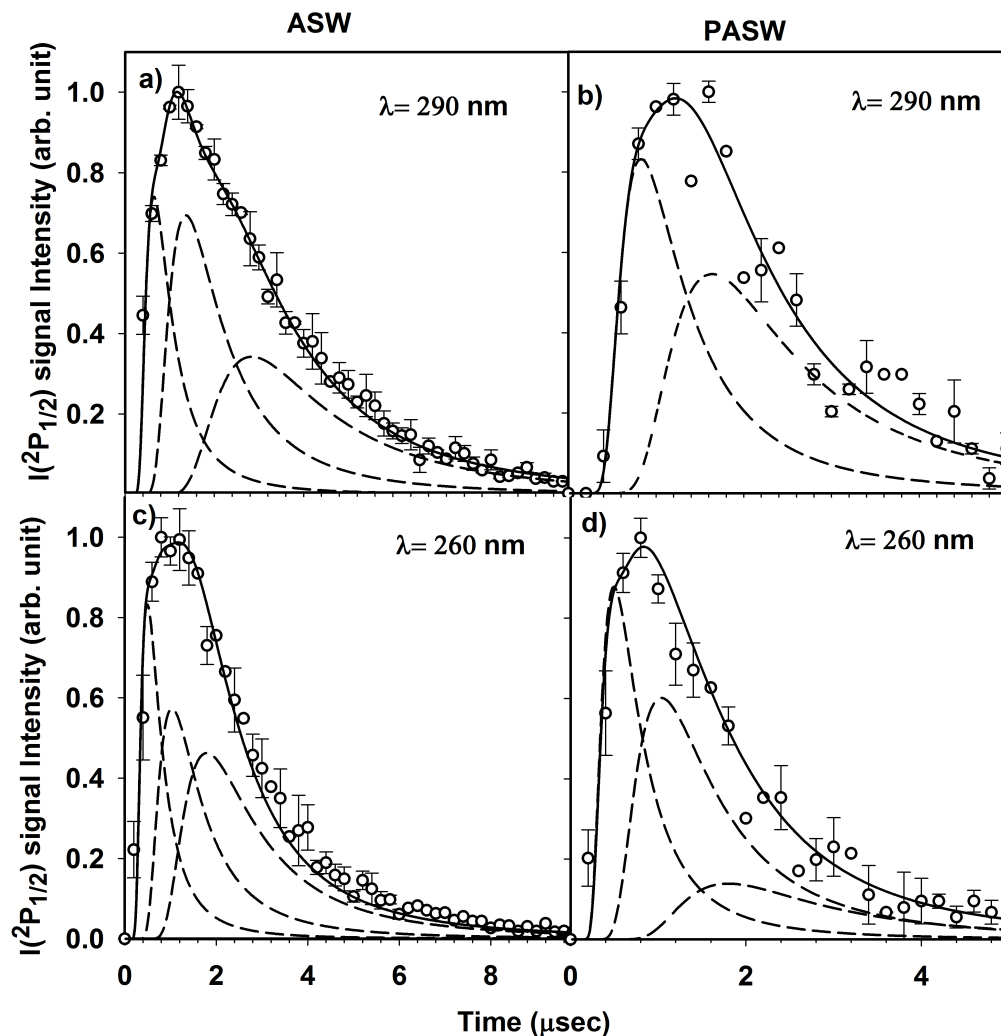


Figure 2.6: Summation of multiple Maxwell-Boltzmann distributions (solid line) fit to $I(^2P_{1/2})$ TOF data for 0.1 L CH_3I adsorbed on 50 ML of a) ASW and b) PASW. Laser light with 290 nm (top panel) and 260 nm (bottom panel) wavelength was used to irradiate the surface. The dashed lines represent energetic nonthermal components. Unlike $I(^2P_{3/2})$ TOF data, the dotted lines that represent the thermal Maxwell-Boltzmann distribution is absent.

Photodissociation (290 nm) of CH_3I on ASW produces $I(^2P_{3/2})$ with an energetic nonthermal component corresponding to an effective temperature of 12500 K (1.6 eV) with intermediate components at 1550 K (0.2 eV) and 380 K (0.05 eV) and a slow component at 90 K (0.01 eV). Photodissociation (290 nm) of CH_3I adsorbed on

PASW (figure 2.5b) yields a fast component 12500 K (1.6 eV) as well as intermediate distributions at 2000 K (0.25 eV) and 750 K (0.09 eV). Photodissociation of CH₃I adsorbed on ASW (figure 2.5c) using 260 nm photons yields a ToF distribution with an energetic nonthermal component at 19500 K (\sim 2.5 eV) and intermediate components at 1900 K (\sim 0.25 eV) and 400 K (\sim 0.05 eV). 260 nm photodissociation of CH₃I adsorbed on PASW (figure 2.5d) yields a fast component 19500 K (\sim 0.25 eV) and intermediate components of 2300 K (\sim 0.3 eV) and 500 K (0.06 eV). The thermal Maxwell-Boltzmann distribution is only observed with I(²P_{3/2}) photofragment when CH₃I is adsorbed on ASW. The effective thermal temperature (90 K) is represented by dotted lines.

The I(²P_{3/2}), the I(²P_{1/2}) time of flight distribution for CH₃I adsorbed on either PASW or ASW are composed of only nonthermal components. As shown in figure 2.6, the ToF distribution can be fitted using at most three Maxwell-Boltzmann distributions. With 290 nm, CH₃I adsorbed on ASW (Figure 2.6a) has a highly energetic nonthermal component with an effective temperature of 11500 K (\sim 1.5 eV) and intermediate components of 2600 K (\sim 0.34 eV) and 600 K (0.08 eV). For CH₃I adsorbed on PASW (Figure 2.6b), the highly energetic nonthermal component is 7000 K (\sim 0.9 eV) with an intermediate nonthermal component of 1800 K (\sim 0.23 eV). When 260 nm photons are used to irradiate the methyl iodide, the nonthermal component of the ToF distribution is the same for both ASW (Figure 2.6c) and PASW (Figure 2.6d). The highly nonthermal component is 7200 K (\sim 0.93 eV) and the intermediate nonthermal components are 1650 K (\sim 0.21 eV) and 550 K (\sim 0.07 eV).

The ToF data can be summarized as follows: 1) The I(²P_{3/2}) and I(²P_{1/2}) distributions for CH₃I adsorbed on either ASW or PASW surfaces have fast nonthermal, intermediate, thermalized and slow components using both 290 and 260 nm excitation wavelengths; 2) The relative contribution of nonthermal velocities is much higher for the I(²P_{1/2}) relative to I(²P_{3/2}) fragment using both 290 and 260 nm excitation; 3)

the ToF distributions are generally narrower for CH_3I adsorbed on PASW relative to ASW; and 4) the ToF distributions are generally faster and narrower using 260 nm excitation.

The ToF distributions for the non-resonant I_2^+ signal observed during 290 and 260 nm photodissociation of CH_3I adsorbed on ASW is shown in Figure 2.7. The I_2^+ signals were detected using 305 nm as well as the 304.67 and 305.57 nm $\text{I}(^2\text{P}_{3/2})$ and $\text{I}(^2\text{P}_{1/2})$ REMPI wavelengths.

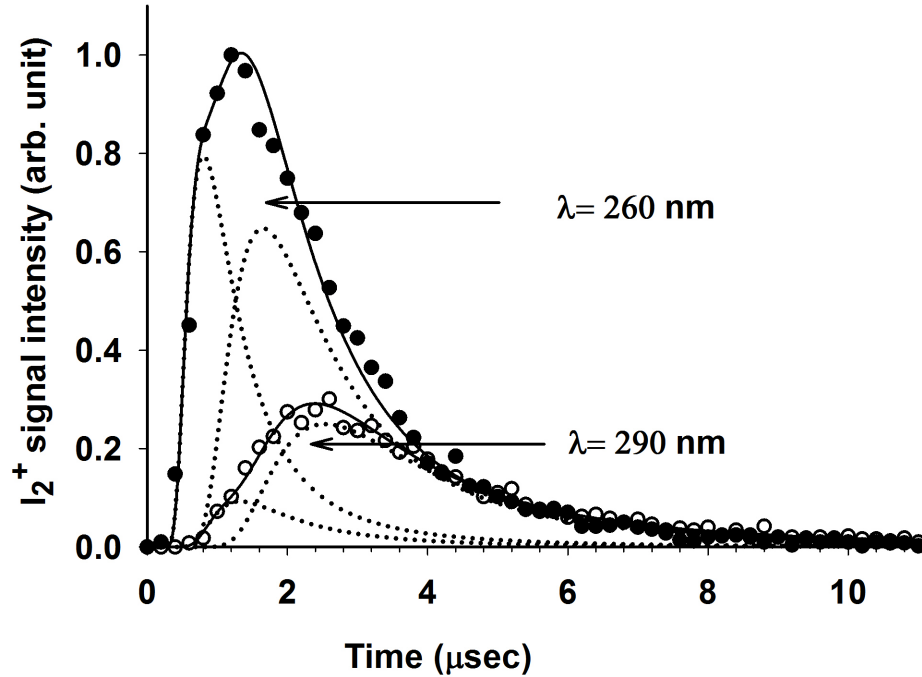


Figure 2.7: Maxwell-Boltzmann distributions fit to non-resonant I_2 TOF data for 0.1 L CH_3I adsorbed on ice grown at 130 K (ASW) for both 290 nm and 260 nm.

The ToF distributions at 290 nm (open circles) and 260 nm (solid circles) are fit with to two Maxwell-Boltzmann distributions (dotted lines) that have a highly energetic nonthermal component with an effective temperature of 5500 K (~ 0.71 eV)

for both wavelengths and intermediates component with effective temperatures of 1500 K (~ 0.19 eV) for 290 nm and 1300 K (~ 0.17 eV) for 260 nm. The atomic and molecular iodine ToF data is compiled and presented in Table 2.1.

Table 2.1: Effective temperature of Maxwell Boltzmann distribution with corresponding translational kinetic energy.

$\lambda(nm)$	Ice type	Photofragment	Non-thermal T(K),(eV)	Intermediate T(K),(eV)	Slow T(K),(eV)	Thermal T(K),(eV)
290	ASW	$I(^2P_{3/2})$	12500,(1.62)	1550,(0.2)	380,(0.05)	90,(0.01)
		$I(^2P_{1/2})$	11500,(1.49)	2600,(0.34)	600,(0.08)	
		I_2	5500,(0.71)	1500,(0.19)		
	PASW	$I(^2P_{3/2})$	12500,(1.62)	2000,(0.26)	750,(0.1)	
		$I(^2P_{1/2})$	7000,(0.90)	1800,(0.23)		
260	ASW	$I(^2P_{3/2})$	19500,(2.52)	1900,(0.25)	400,(0.05)	90,(0.01)
		$I(^2P_{1/2})$	7200,(0.93)	1650,(0.21)	550,(0.07)	
		I_2	5500,(0.71)	1300,(0.17)		
	PASW	$I(^2P_{3/2})$	19500,(2.52)	2300,(0.30)	500,(0.06)	
		$I(^2P_{1/2})$	7200,(0.93)	1650,(0.23)	550,(0.07)	

In summary, photodissociation of adsorbed CH_3I shows the following important differences relative the gas-phase: 1) The yields of the $I(^2P_{3/2})$ and $I(^2P_{1/2})$ fragments are similar using both 260 nm and 290 nm; 2) The kinetic energies of these photofragments are substantially higher than those produced in the gas-phase; 3) The production and release of I_2 is a significant product channel.

2.4 Discussion

2.4.1 Structure of methyl iodide adsorbed on ice and the effect of ice morphology

The temperature programmed desorption (TPD) of 0.1 ML of CH_3I adsorbed on either ASW or PASW is similar to that of CCl_4 adsorbed on the same type of ice.[69] The feature at 120 K, shown in Figure 2.3, represents the desorption of isolated CH_3I monomers from the ice surface. At the low coverage used in this study, the multilayer desorption feature (130 K) is negligible for ASW and completely absent for

PASW. This indicates that CH_3I molecules are primarily isolated on both ice surfaces, implying that there is very limited molecule-molecule (i.e $\text{CH}_3\text{I}:\text{CH}_3\text{I}$) interaction.

The effect of ice morphology on the desorption of CH_3I can also be deduced from the TPD data. For CH_3I adsorbed on ASW, the CH_3I exists in the form of two dimensional islands.[70] The absence of the multilayer desorption state ($\sim 130\text{K}$) in the TPD data indicates only the desorption of free monomers of CH_3I from the ASW ice surface. However, according to previous studies done on adsorption of CCl_4 on ice,[22] the porosity of PASW ice could lead to the formation of three dimensional CH_3I clusters trapped in the near surface region of the ice. When CH_3I is deposited on PASW, the micropores are filled before the CH_3I proceeds to form 2 dimensional islands as observed on ASW ice. The trapped CH_3I molecules are released at a much higher temperature (150 K) as shown in Figure 2.3a due to the restructuring of the ice. CH_3I trapped in 50 ML of PASW had TPD features at 150 K and 160 K that were similar to that of CH_3I adsorbed on PASW. The rapid release observed at 150 K has previously been reported and attributed to the phase transition of ice, in this case from amorphous to crystalline ice.[67] The overlap of the CH_3I desorption peak at 160 K and the TPD peak of H_2O suggests that not all trapped CH_3I molecules escape into the gas phase during the phase transition from amorphous to crystalline ice. These remaining CH_3I molecules are trapped at the grain boundaries in the bulk crystalline ice and desorbed simultaneously with the crystalline ice (Figures 2.3a,c).

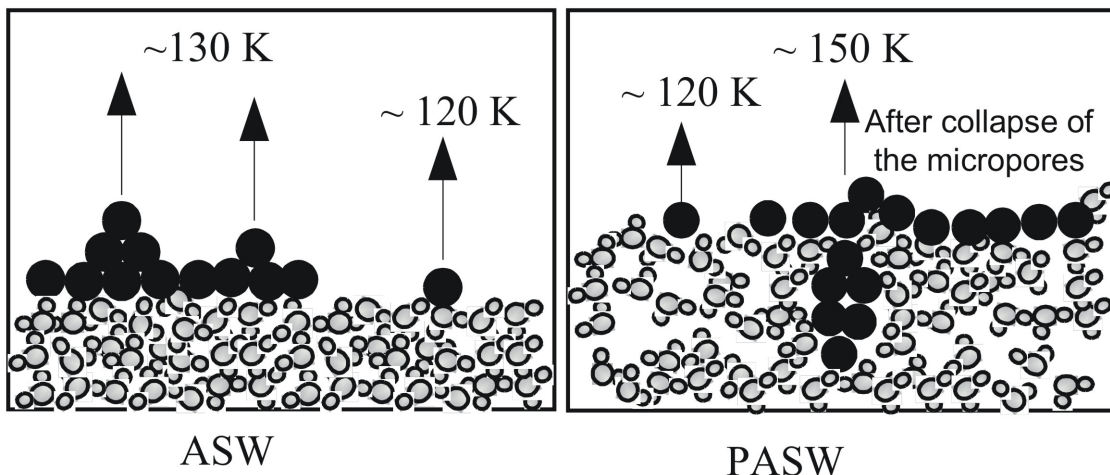


Figure 2.8: Desorption pathways of CH_3I from amorphous solid water (ASW) and porous amorphous solid water (PASW) ice from amorphous.

2.4.2 Electronic Structure of CH_3I and adsorbed CH_3I

The electronic structure and gas phase dissociation of CH_3I in the A band ($320 \text{ nm} < \lambda < 210 \text{ nm}$) has been widely studied.[71] Photodissociation of CH_3I in the A band involves overlapping Frank Condon transitions to three excited states, $^3\text{Q}_1$, $^3\text{Q}_0$ and $^1\text{Q}_1$ (Mulliken's notation). It has been shown that the $^3\text{Q}_0$ correlates asymptotically with the $\text{I}(^2\text{P}_{1/2})$ state while the $^1\text{Q}_1$ and $^3\text{Q}_1$ correlate with the $\text{I}(^2\text{P}_{3/2})$. However, as shown in Figure 2.9, molecules that are photoexcited to the $^3\text{Q}_0$ state can mix with the $^1\text{Q}_1$ states corresponding to the ground spin-orbit state $\text{I}(^2\text{P}_{3/2})$. Previous gas phase dissociation studies show that the system curve crosses over the $^1\text{Q}_1$ curve with about 25 % probability,[72] and according to figure 2.8, 260 nm excitation photodissociation of gas phase CH_3I should yield predominantly $\text{I}(^2\text{P}_{1/2})$.

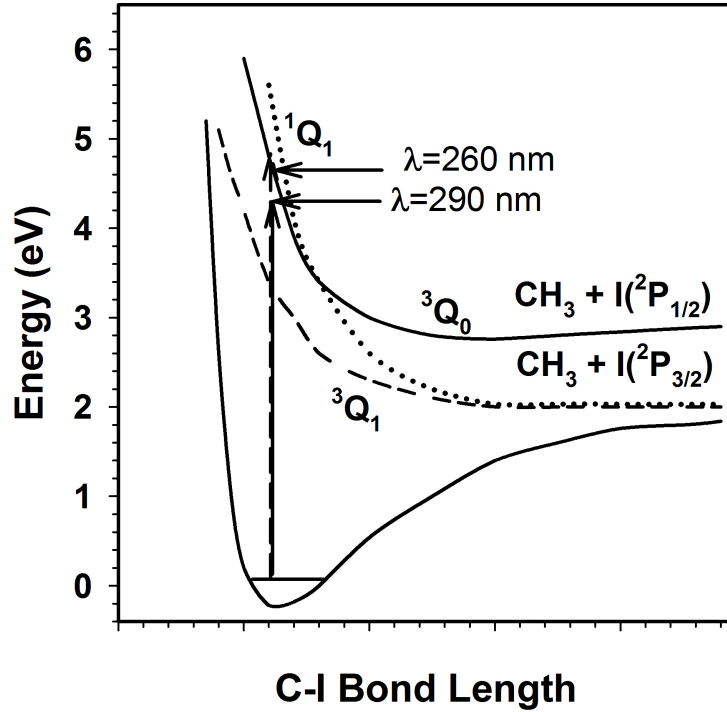


Figure 2.9: Schematic one-dimensional potential energy diagram involved in CH_3I A-band photodissociation. Gas phase A-band photo-excitation occurs primarily from the ground state to $^3\text{Q}_0$ excited state, however, due to spin-orbit coupling the $^3\text{Q}_0$ state mixes with the $^1\text{Q}_1$ state at the curve crossing.

Though this is not shown in figure 2.9, CH_3I can also dissociate at lower energies via a well known process known as dissociative electron attachment. This involves an inelastic scattering event with a low-energy electron typically produced by excitation of the underlying metal substrate. DEA can yield both I and CH_3 fragments with non-thermal energy distributions. However, the present study was carried on a 50 ML thick layer of ice, thereby eliminating the effects due to the underlying polycrystalline zirconia substrate. Also, the bulk band gap of the polycrystalline zirconia (>5 eV)[73] is larger than the incident energy of the laser (4.28 or 4.77 eV). Therefore the photodissociation of adsorbed CH_3I by single photon-induced electron attachment can be considered largely eliminated.

The excited electronic states (3Q_1 , 3Q_0 and 1Q_1) which contribute to the A band dissociation of CH_3I involves transitions from the lone pair of the iodine to the anti-bonding carbon-iodine orbital. Due to surface interactions, the p-orbitals of adsorbed CH_3I molecules are not degenerate since the p_z orbital is lowered by the surface binding energy (~ 0.6 eV) thereby shifting the 3Q_0 state higher in energy.[74] Therefore when CH_3I is adsorbed and oriented towards the ice water molecules, the electronic coupling of the p_z orbital can reduce the initial accessibility of the 3Q_0 state.

2.4.3 Photodissociation mechanism

There are two possible pathways by which atomic iodine can be formed. An atomic iodine photofragment can be formed by photodissociation of photodesorbed CH_3I or photodissociation of CH_3I adsorbed on ice. Ice is transparent at the two wavelengths used [75] and most of the incident photons are absorbed by the polycrystalline zirconia substrate. With a laser fluence of $\sim 300 \mu\text{J}/\text{cm}^2$ and a pulse width of 10 ns the calculated maximum average temperature rise is insufficient to induce any appreciable thermal desorption.

The observed difference in the photodissociation dynamics of adsorbed CH_3I on ice surface compared to gas phase is controlled by the coupling of the adsorbate to the surface and the iodine photofragment velocity and orientation. The predominance of the lower spin state can be understood in terms of the above mentioned substrate and orientation induced state-mixing.[76]. The 0.6 eV surface induced higher energy shift of the 3Q_0 state clearly inhibits the direct accessibility of the 3Q_0 state. Since the 3Q_0 asymptotically correlates to the $\text{I}(^2\text{P}_{1/2})$ product, the inability to directly populate this state reduces the $\text{I}(^2\text{P}_{1/2})$ production probability to only trajectories that cross with the directly accessible 1Q_1 surface.

The reduction of the $\text{I}(^2\text{P}_{1/2})$ signal compared to gas phase may also be explained if the $\text{I}(^2\text{P}_{1/2})$ photofragment scatters into the ice and remains trapped or undergoes a

non-spin conserving collision with the ice. This implies that surface photodissociation produces $\text{I}(^2\text{P}_{1/2})$ with a smaller recoil velocity relative to $\text{I}(^2\text{P}_{3/2})$.^[77] In addition to the change in the spin-state distribution, the results presented here show a deviation from the kinematics of the gas-phase photodissociation of CH_3I . For example, the maximum available energy of the iodine fragment monitored at 260 and 290 nm wavelength should be ~ 0.24 eV due to conservation of energy during photodissociation and the mass ratio between methyl (m/z 15) and iodine (m/z 127).^[78] Figure 3 shows non-thermal components as high as 2.5 eV for the $\text{I}(^2\text{P}_{3/2})$ fragment from photodissociation of CH_3I adsorbed on ASW at 260 nm. Heavy halogen photofragments (bromine and iodine) with high velocities that are in excess of those expected from gas phase photodissociation have been previously reported.^[79] Unlike the light fragment of the photodissociation process (methyl $m/z = 15$), heavy fragments [Br ($m/z = 79$) and I ($m/z = 127$)] are known to violate conservation of momentum.^[72] Cowin and coworkers explained this deviation from gas phase photolysis in terms of a simple dynamic model in which light methyl fragments transfer some of their translational energy to the heavy halogen fragments.^[80] The intermediate components of the energy distributions presumably belong to iodine atoms that suffer collisions before escaping into the vacuum at different trajectories.

The ground state iodine fragment $\text{I}(^2\text{P}_{3/2})$ that has fully thermalized with the ice substrate is only observed when CH_3I is adsorbed on ASW (Figures 2.5a and 2.5c). In contrast, CH_3I adsorbed on PASW shows no contribution from iodine atoms that have equilibrated with the ice substrate before escaping (thermal temperature 90 K). As explained in Section 2.4.1, the presence of pores in PASW could either make the trapped CH_3I molecule unavailable for photodissociation or trap iodine photofragments formed during photodissociation within the ice substrate.

The spin state population and broad kinetic energy distribution of iodine photofragments observed provides a strong evidence for different orientations of the adsorbed

CH₃I molecules on ice. Though the present experimental setup can not distinguish whether the preferred orientation is CH₃I molecules adsorbed with iodine atoms up or down or with the C–I bond lying parallel on the ice surface, previous theoretical calculations and experiments of methyl iodide adsorbed on insulators like LiF [81-83] and MgO [77] surfaces predict a perpendicular orientation with the halogen atoms pointing down. Since we are working at low CH₃I coverage (i.e. where cluster formation and dipole-dipole coupling is minimal), the trajectory of the iodine photofragments must be directed towards the surface before escape. As discussed below, they can also react to form I₂.

2.4.4 I₂ formation and release

I₂ is produced during the photodissociation of adsorbed CH₃I on ASW. A similar signal is not observed for CH₃I adsorbed on PASW. Since monomers are expected to be the dominant adsorbate, the generally pore free surface of ASW enhances the probability of iodine photofragments colliding and reacting with neighboring CH₃I or adsorbed (surface trapped) I. The I₂ formed from these reactions can either thermally equilibrate with the ice surface or if produced with sufficient energy, escape from the surface. Previous gas phase experiments[84] indicates at least the presence of neutral CH₃I dimers is required to form I₂. Though the TPD data indicates no or minimal dipole-dipole coupling of CH₃I molecules at the low coverage used, the high CH₃I surface concentration on ASW (relative to PASW) increases the number of trapped iodine photofragments. In addition, it increases the probability of reactive scattering events that form I₂. Unlike ASW, the high surface to volume ratio of PASW and the presence of pores limits the possibility of collisions of neighboring iodine species. The observed increase in the yield of I₂ with 260 nm light relative to 290 nm light is also important. Recall that the low yield of the I(²P_{1/2}) from surface photodissociation relative to gas-phase photodissociation using 260 nm was attributed to the coupling

to the surface. The reduced yield and the $I(^2P_{1/2})$ velocity distribution implies that these fragments probably undergo reactive scattering to form trapped I (and hence I_2) more effectively than $I(^2P_{3/2})$. The escaping I_2 bi-modal energy distribution may also reflect multiple collision geometries and/or different precursors.

2.5 Conclusion

The interaction of adsorbed CH_3I on both porous amorphous solid water (PASW) and amorphous solid water (ASW) and subsequent photodissociation have been investigated. The photodissociation dynamics leading to the formation of $I(^2P_{3/2})$ and $I(^2P_{1/2})$ are dependent on the morphology of the ice surface. According to TPD measurements, ASW has a small surface defect density, thereby providing a possible pathway for the photofragments to collide and thermalize with the ice substrate. The relative quantum yield of the formation of I photofragments favors the $I(^2P_{3/2})$ states, a deviation from gas phase photodissociation suggesting a strong interaction of H_3I with the surface of the ice water molecules. The higher velocity possessed by $I(^2P_{3/2})$ photofragments enhances their surface escape probability compared to $I(^2P_{1/2})$ photofragments. Finally, the ability of the ice surface to trap predominantly $I(^2P_{1/2})$ produced during photodissociation and reactive scattering of iodine atoms with neighboring iodine containing species likely accounts for the formation of I_2 .

CHAPTER III

PROBING THE INTERACTION OF HYDROGEN CHLORIDE WITH LOW-TEMPERATURE WATER ICE SURFACES USING THERMAL AND ELECTRON-STIMULATED DESORPTION

3.1 Introduction

Several studies have investigated the interaction of adsorbates such as HCl on low temperature ices under high or ultra-high vacuum conditions. Kang et al. used reactive ion scattering (RIS) and low energy secondary ion mass spectrometry (SIMS) to measure the extent of ionization with temperature and found mostly molecular HCl at temperatures below 70 K, a mixture of the ionized and molecular forms of HCl from 90–120 K, and complete ionization above 140 K.[23] Molecular beam experiments[24] and temperature programmed desorption (TPD) [25-28] have found two types of HCl adsorption at temperatures between 100–170 K, assigned as molecular HCl adsorption and a second ionized or hydrated species. HCl has been shown to aid in further dissolution of HCl molecules, with the Cl^- ion acting to solvate the hydrogen side of the incoming HCl molecule.[85] In addition, spectroscopic studies have shown evidence of complete ionization at 80 K on ice films,[29, 30] while others report molecular bands that exist up to 125 K.[31] Near-edge X-ray absorption fine structures (NEXAFS) spectroscopy has been used with photon-stimulated desorption (PSD) to probe the interaction of HCl and ice in the bulk and on the surface,[86] respectively. These measurements provide evidence of ionization both in the bulk and at the surface; the molecular HCl signal was not observed when 1 L of HCl was adsorbed on 100 L of

crystalline ice at 120 K. Changes due to the solvated Cl^- ion were also observed in the spectra.

Several theoretical and modeling studies have also attempted to describe solvation of HCl on ice surfaces. Gertner and Hynes employed molecular dynamics simulations of HCl on the surface of ice at 190 K and suggested that the HCl was initially incorporated as a molecular species into the ice lattice (not the bulk).[87] In this case, there was a barrier for dissociation since the dynamic lattice response was not taken into account. However, more recent calculations by Bolton et al.[88] and Buch et al.[85] have clearly demonstrated the importance of defect configurations, the amount of HCl, and the dynamic lattice relaxation of the ice.

Electron stimulated desorption (ESD) is an extremely sensitive surface specific probe that has been used to study the near-surface structure of ice.[89-91] The two features that make ESD inherently surface sensitive are the low penetration depth of electrons and the fact that cations must be produced at or near the surface to desorb from the sample. It has been shown that the ESD products can be greatly affected by small changes in the local potential and excited state lifetimes of the surface molecules.[90] Using ESD, we can examine the temperature and phase dependence of the cation yields to gain insight into the dynamic interactions of small molecules with low-temperature ice surfaces.

In this set of experiments, a detailed ESD study of the interactions of low concentrations of HCl with low-temperature porous amorphous solid water (PASW), amorphous solid water (ASW) and crystalline ice (CI) surfaces has been done.

3.2 Experimental Details

The ultra-high vacuum (UHV) chamber used for this experiment (Figure 3.1) operates with a typical base pressure of 2×10^{-10} Torr equipped with a pulsed low-energy electron beam, a quadrupole mass spectrometer (QMS), a time-of-flight (TOF) mass

spectrometer, and a cryogenically cooled sample mount. The substrate was an oxidized zirconia sample that could be varied in temperature from 80 K to 600 K and rotated to face any port in the UHV chamber. The temperature was controlled via a computer and feedback loop for TPD measurements as well as controlling the morphology of the ice sample. The ultra-high vacuum (UHV) chamber used for this experiment (Figure 3.1) operates with a typical base pressure of 2×10^{-10} Torr equipped with a pulsed low-energy electron beam, a quadrupole mass spectrometer (QMS), a time-of-flight (TOF) mass spectrometer, and a cryogenically cooled sample mount.

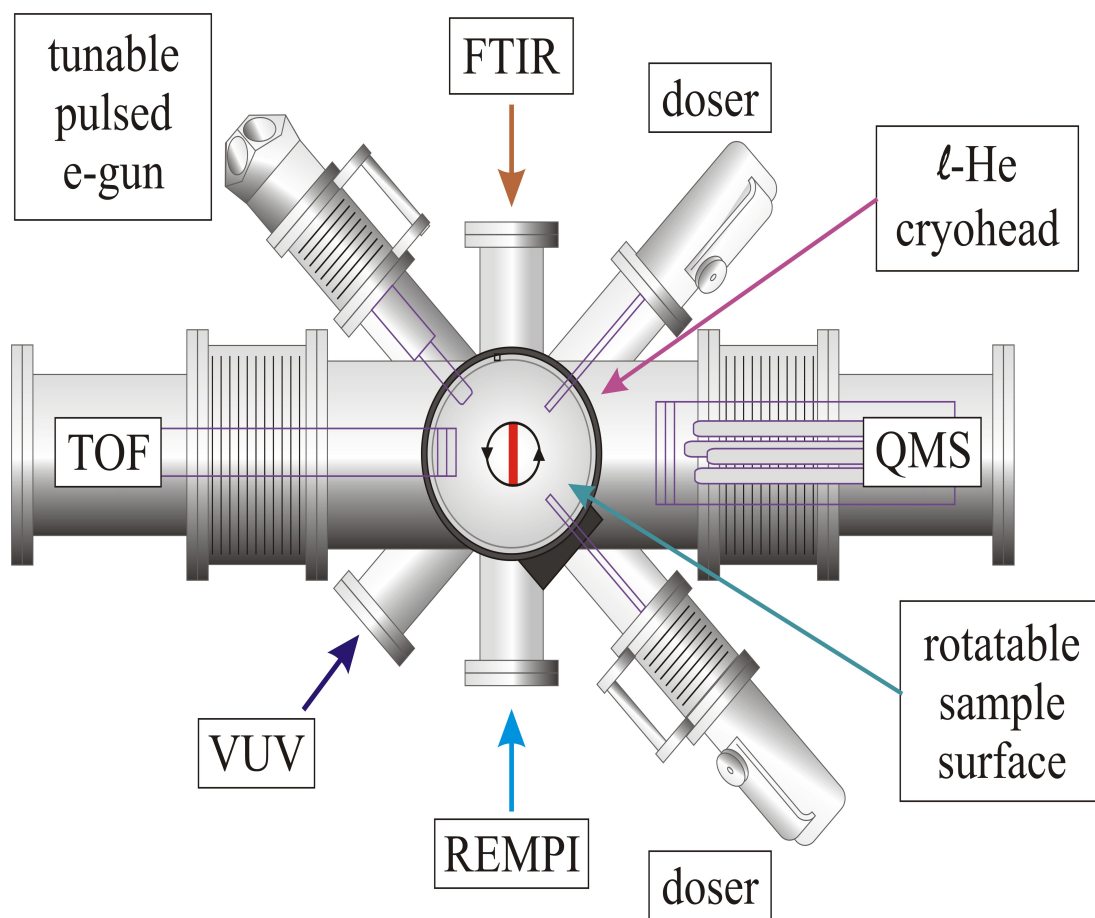


Figure 3.1: Schematic of UHV chamber used for probing interaction of HCl on ice.

The pulsed electron gun was at a 45 degree incident angle relative to the sample substrate normal and the electron beam energy could be varied from 5 to 250 eV.

The electron flux density during a single 200 ns pulse was typically $6 \times 10^{13} \text{ s}^{-1} \text{ cm}^{-2}$. The configuration of the electron gun, time-of-flight (TOF) mass spectrometer and sample was designed to allow field free measurements to be taken with the TOF at a 90 degree angle relative to the sample plane. A 100 V extraction field on the TOF was typically used to collect the desorbing cations unless otherwise stated, such as during the velocity distribution measurements where field free conditions were implemented.

Precautions were taken to eliminate any effects of co-dosing HCl with water since this may lead to the dosing of ionized species. Therefore, the chamber was equipped with two completely separate dosing lines terminated in leak valves with directed dosing tubes. The dosing lines were thoroughly baked and equipped with liquid nitrogen traps. The HCl dosing line was purged to passivate the surface and equipped with a directed glass dosing tube to reduce contamination products from HCl reacting with metal surfaces. Using the QMS, we found the HCl to be free of any contamination. The water samples were purified by several freeze-pump-thaw cycles prior to dosing. The ice samples were vapor deposited at controlled temperatures designed to specifically grow PASW at 80 K, ASW at -110 K, or CI at -140 K.

A minimum of 40 ML was found to be sufficient to decouple the surface of the ice from the substrate, and all samples were >50 ML to ensure the measurements were not affected by the substrate. HCl coverages were determined by measuring the pressure change in the chamber during dosing corrected with an enhancement factor of 10 to account for the directed dosing. This is an upper limit to the amount of HCl and assumes a unit sticking probability. At low temperatures, the HCl sticking probability is close to unity. However at higher temperatures (specifically those samples dosed at 140 K) the coverage of HCl is most likely lower than calculated.

3.3 *Results*

3.3.1 Cations from ice surfaces containing HCl.

The cations produced and desorbed during 250 eV electron impact of pristine ice can be seen in the solid lines of Figure 3.2. The cation yield is dominated by H^+ with a much less H_2^+ , and an even smaller yield of $\text{H}^+(\text{H}_2\text{O})_n$. The cluster yield from PASW is the highest and it is typically 5–6 times larger for CI, and about 2–3 times larger than for ASW.[92]

A very interesting and dramatic change in the cation yields occurs due to the presence of small amounts of HCl.[21] This change can be seen in Figure 3.2 where the dashed gray lines represent the ESD yields after a dose of ~ 0.1 ML of HCl. Dosing PASW with small amounts of HCl increased the cluster yield by approximately 1.3 times compared to that of pristine PASW ice while dosing HCl on ASW increased the cluster yield by 3–5 times. However, the largest relative increase in the cluster yield is observed for HCl on CI. Specifically, the $\text{H}^+(\text{H}_2\text{O})_1$ and $\text{H}^+(\text{H}_2\text{O})_2$ yields increased by over a factor of five and eight, respectively. This large enhancement required the presence of ~ 0.3 ML HCl on H_2O at 140 K. When CI was initially grown at 140 K, then lowered to 80 K for HCl dosing, and finally raised back to 140 K prior to irradiation, approximately the same increase was seen in the clusters for HCl that was both dosed and irradiated at 140 K. The CI sample dosed and irradiated at 80 K also showed an increase in the cluster ion yield, although the change was not as large as with dosing at higher temperatures. As discussed in more detail below, this probably indicates only partial ionization of the HCl at 80K.

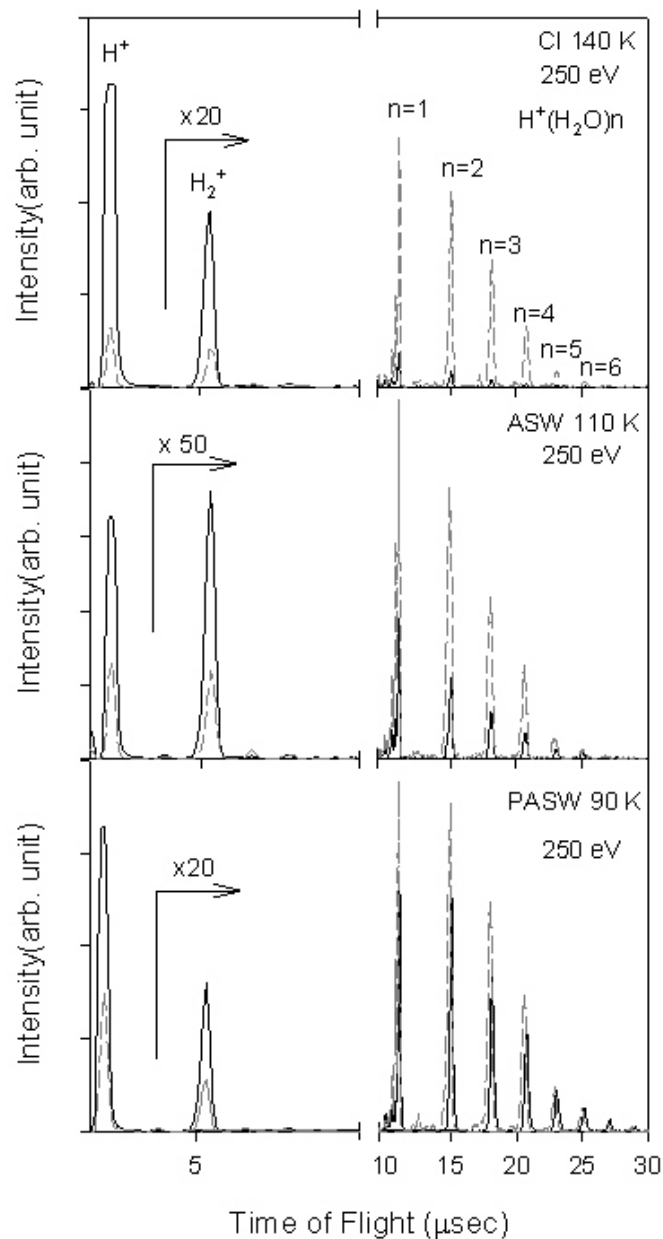


Figure 3.2: Cations produced and desorbed during 250 eV electron impact of pure (solid line) and HCl (dashed gray line) dosed PASW (bottom panel), ASW (middle panel), and CI (top panel). Upon addition of HCl there is a large decrease in the H^+ and H_2^+ yields and an increase in the cluster yields.

Figure 3.3 shows the relative increase in integrated total cluster yields as a function of HCl coverage. The filled symbols correspond to $\text{H}^+(\text{H}_2\text{O})$, and the dimer ($\text{H}^+(\text{H}_2\text{O})_2$) is shown as open symbols for CI (bottom panel), ASW (middle panel) and PASW (top panel). Dosing each phase of ice at different temperatures provided a unique response to increasing amounts of HCl. CI dosed at 140 K shows the largest relative change. The smallest increase is PASW dosed at 80 K, with the clusters approaching twice the value of the pristine ice sample. While this relative increase is the smallest of all samples, it is important to note the PASW had the highest overall cluster yields. The cluster yield from ASW dosed with HCl at 110 K is 3–4 times the value of pure ice, reaching this value at ~ 0.5 ML HCl coverage. Similar to the ASW sample, CI dosed at 140 K also reaches an upper limit for clusters between 0.5–0.6 ML. After the first dose of HCl on PASW, the H_2^+ yield dropped $\sim 30\%$, decreasing by $\sim 80\%$ after ~ 0.75 ML HCl. In summary, the CI shows the most dramatic increase in the cluster yield, followed by the annealed ASW and PASW ice films. In contrast to the cluster yields, the H^+ and H_2^+ yields significantly decrease ($>80\%$) upon adsorption of HCl.

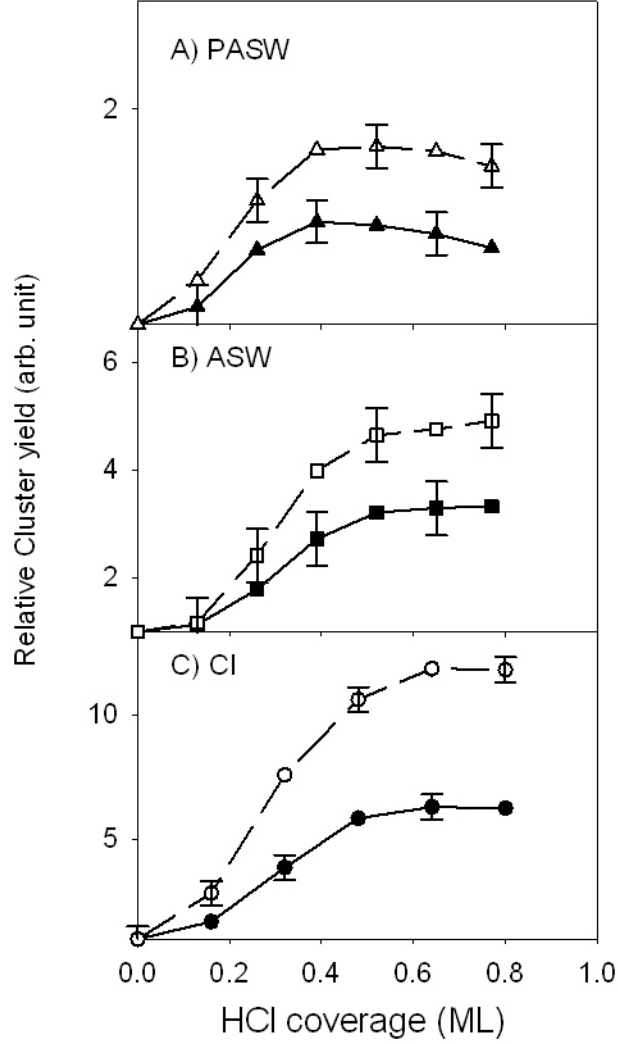


Figure 3.3: Relative increase in cluster yield with HCl coverage for $H^+(H_2O)$ (filled symbols) and $H^+(H_2O)_2$ (open symbols) for (A) PASW, (B) ASW, and (C) Cl.

3.3.2 H^+ kinetic energy distributions with/without HCl.

Due to the large proton yields, time-of-flight (TOF) distributions could be measured under field-free conditions (no extraction potential). The TOF taken under these conditions can be converted into a kinetic energy distribution by using the Jacobian transformation $I(E) = I(t)t^3/(mL^2)$ where $I(t)$ is the intensity as a function of time

(t) , m corresponds to the mass of the ion, and L is the length of the flight path traveled by the ion. The kinetic energy distributions of the proton from CI and PASW are shown in Figure 3.4. The solid squares are the Jacobian transformation of the data for pure ice samples and the open circles are for HCl dosed ices. The dotted and dashed lines in Figure 3.4A (CI) represent the Gaussian curves fit to the data with the sum shown as a solid line. The kinetic energy distribution from CI can be represented by two Gaussian curves with peak kinetic energies of ~ 4 eV and ~ 8 eV, indicating that at least two channels are responsible for proton production and desorption. At lower temperatures, only the first spectrum recorded shows a small contribution from the lower energy channel, most likely the result of efficient removal of dangling bonds during the first several electron pulses. The resulting spectrum is similar to that shown in Figure 3.4B for both pure and HCl dosed PASW. The solid and dashed lines in 3.4B are fits to the data and the Gaussian curves centered at ~ 8 eV describe the data reasonably well. Note that there is no shift in the kinetic energies of the protons with HCl dosing for either CI or PASW, indicating that the surface is not charging.

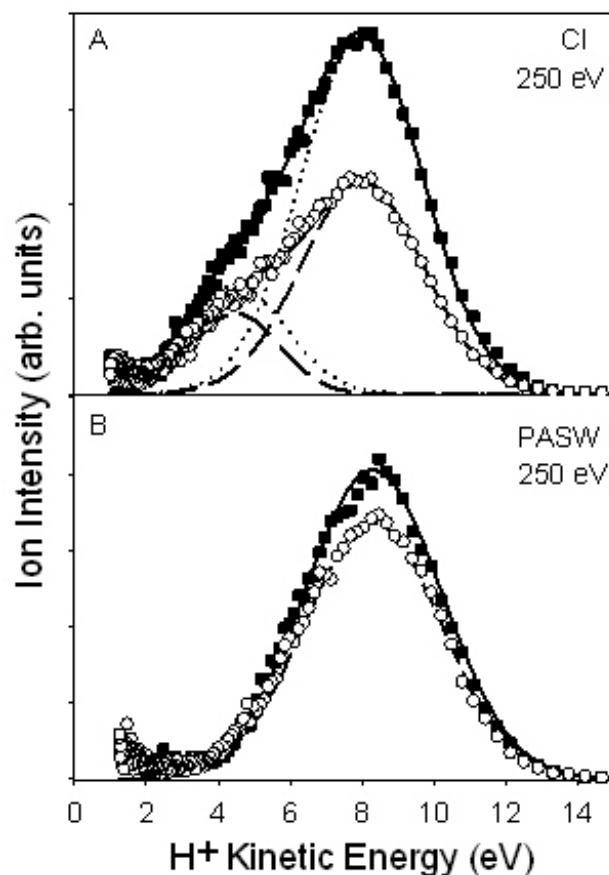


Figure 3.4: H^+ velocity distribution from pristine (squares) and HCl dosed (circles) (A) CI and (B) ASW ice samples collected under field-free conditions. The dotted and dashed lines in are the Gaussian fit to the fast and slow velocity components for pristine and HCl dosed ice, respectively. The solid lines are the sum of the Gaussian fit which accurately describe the data.

3.3.3 TPD of HCl: Ice at several growth temperatures.

TPD was performed after ESD-TOF measurements as well as on non-irradiated samples to ensure the irradiation was not causing the ionization of the adsorbed HCl. Figure 3.5 shows typical TPD traces from HCl dosed ice. The dashed line corresponds to water desorption (divided by 5) and HCl desorption is shown as the solid line. All of the TPD spectra for the corresponding ESD-TOF spectra shown have only one HCl TPD peak which is coincident with the water desorption peak. As discussed

later in this paper, we interpret this as a strong indication of HCl ionization on the ice surface. This does not rule out the possibility of some physisorbed HCl.

Although this is not an in-depth investigation of HCl TPD from ice, it provides useful insight into the interaction of HCl on the ice surface. As shown in Figure 3.5, there are three main desorption features that occur under various dosing conditions for HCl coverages greater than 0.5 ML. The first is feature (I) which is coincident with water desorption. The second feature (II) is a shoulder (non-resolved peak) which can start between 110 K and 130 K depending on HCl dosing temperature and leads into the first feature. The lowest temperature feature (III) occurs when dosing HCl below 110 K.

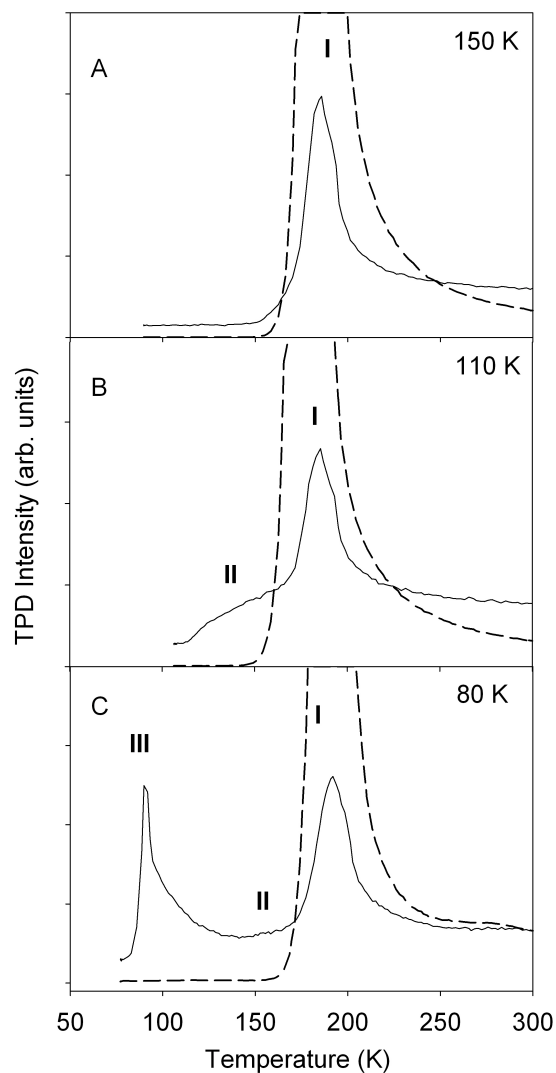


Figure 3.5: Temperature programmed desorption spectra of HCl dosed on ice at (A) 150 K, (B) 110 K, and (C) 80 K on CI, ASW, and PASW, respectively. The dashed line is the water desorption (divided by 5 for comparison) and the solid line is the HCl desorption. There are three different desorption features seen under the dosing conditions used. All TPD spectra of the samples used in the ESD measurements showed only one desorption feature (I) attributed to an ionized species.

3.4 *Discussion*

3.4.1 Mechanisms for cation ESD

A brief review of the electronic structure of condensed phase water and the excited states leading to proton desorption is provided. A more detailed description of the electronic structure of water can be found elsewhere.[90, 92] Calculations and photoemission data show the electronic structure of condensed ice retains much of the gas-phase character with some broadening and minor shifting of the energy levels. The largest change in the condensed phase occurs in the a_1 levels which are significantly broadened, (compared to the $1b_1$ and $1b_2$ levels), and are most affected by hydrogen bonding. Specifically, the unoccupied $4a_1$ orbital is in the band gap, spatially extended, and mixed with the $2b_1$ level. All of these two-hole and two-hole one-electron excited states involve bands of a_1 symmetry, which are involved in hydrogen bonding. Since levels with a_1 character are sensitive to the local bonding environment, the proton yields can be used to gather information about the local geometry and dynamic response of the ice surface.[92] At low dosing temperatures, the random orientation of the surface water molecules leads to a low proton yield for PASW compared to CI most likely because the proton undergoes reactive scattering across the ice surface or into the bulk.[93] As the temperature increases, the degree of coupling between water molecules decreases while the number of dangling bonds and mobility of surface water molecules increases.[94] These changes can increase excited state lifetimes and the probability for proton emission.[90, 92] As described in ref 92, the kinetic energy and threshold energy measurements indicate that the production of H^+ involves either two-hole or two-hole one-electron excited states that involve bands of a_1 symmetry. The primary valence configurations $(3a_1)^{-1}(1b_1)^{-1}(4a_1)^1$ and $(3a_1)^{-2}(4a_1)^1$ are known to produce protons with kinetic energy ranging from 0 and 4 eV. The $(1b_1)^{-2}(4a_1)^1$ configurations produce protons with kinetic energy between 4 and 7 eV while the two-hole $(2a_1)^{-1}$ states leads to the formation of fast protons

with kinetic energy greater than 7 eV.

H_2^+ desorption has similar threshold values compared to H^+ but the yield is much lower. Although the branching ratio is small, some of the above mentioned two-hole and two-hole one-electron states responsible for proton desorption can decay to form H_2^+ . This has been observed in the time correlated dissociation of doubly ionized states of water, most likely through a dissociative triplet state.[95] Photoionization near the $\text{O } 1s \rightarrow 2b_2$ resonance[96] was reported to produce H_2^+ . The absorption of four photons to produce $\text{H}_2^+(\text{X } ^1\Sigma_g^+)$ was also reported in a recent multiphoton ionization study.[97] The H_2^+ yield observed from these ices is large relative to the gas phase studies. This indicates that many body interactions and orientational defects may play a role in its production. Reactive scattering may also be a source of H_2^+ .

The mechanism for cluster ion desorption involves production of two holes and a Coulomb explosion resulting from these holes in neighboring water molecules. A detailed description of this model can be found elsewhere. Briefly, the weak ~ 25 eV threshold for $\text{H}^+(\text{H}_2\text{O})$ formation is most likely due to intermolecular Coulomb decay (ICD) or reactive scattering of protons.[98] whereas the primary 70 eV threshold for $\text{H}^+(\text{H}_2\text{O})_n$, $n=1-7$ probably corresponds to direct formation of a localized $2a_1^{-2}$ state. Coupling of this excited state with a neighboring water molecule leads to the final state of one positive charge on each of the two water molecules, most likely with an $\text{OH}^+ \dots \text{H}^+(\text{H}_2\text{O})$ configuration. This can occur either through either ICD or ultrafast dissociation. The surrounding water molecules respond to the charges by reorienting in an attempt to solvate the charges, and finally the unstable configuration undergoes a Coulomb explosion resulting in desorption of a protonated cluster.

The proton yield reflects the bonding configurations of surface molecules with terminal -OH bonds in direct line of sight to the detector. The clusters reflect the behavior of the last several terminal water layers and thus the yields provides information regarding the local hydrogen bonding in these layers. At low HCl dosing

temperatures, the water molecules are randomly oriented in PASW and ASW and there is limited long range order. As stated above, cluster ion formation and ejection requires the localization of holes. Due to the lack of an ordered hydrogen bonding network in PASW, the holes can localize and are less likely to hop beyond a screening distance (1–2 nm) before a Coulomb explosion occurs. This 'localized hole hopping,' where a hole hops to a neighboring water molecule but not far enough to be screened, occurs in the terminal 1–3 water layers of PASW and results in a large cluster yield. Increasing the temperature from 80 K (PASW) to 110 K (ASW) also causes water molecules to rotate/diffuse into configurations that causes micropore collapse and an increased density/order that allows holes to hop further reducing the likelihood of Coulomb explosion occurs. This decreases the cluster yield. As the temperature increases, a more crystalline structure is formed[90, 99] and the holes are more likely to hop even further away from each other through the hydrogen bonding network. Since CI has the most extensive hydrogen bonding network of the samples studied, the efficient hole hopping results in the lowest initial cluster ion yield.

3.4.2 Mechanism of HCl effects on cation ESD.

The solvation of HCl on an ice surface can induce changes in the local molecular structures of the lattice sites surrounding the ionized species.[21] Coupled quantum mechanics/molecular mechanics (QM/MM) simulations of HCl interacting with ice surfaces shows evidence of rapid ionization and changes in the water-water bond lengths upon ionization.[88, 100] The change in the bond lengths is correlated with the disruption of the hydrogen bonding. Solvation of the Cl^- ion decreases the bond lengths in the water molecules closest to the ion and slightly elongate the water-water distances within the next nearest neighbors in the ice lattice.

Since local lattice disruptions and nearest neighbor bond length changes could also effect hole localization probabilities and hence impact the formation rates and

ejection yields of ions, ESD can be a very useful probe of the molecular scale changes induced by the HCl solvation. For example, if the hydrogen bonding network is disrupted such that holes cannot efficiently hop to a distance that allows screening from the second hole, the resulting Coulomb explosion can produce clusters and cause desorption of these charged clusters. This is consistent with the phase dependencies showing the largest HCl induced change for CI, whereas the smallest is observed in the highly disordered PASW. The increase in the cluster yield in PASW and for CI at 80K is evidence that the ice is a dynamic surface and the terminal water molecules can reorient to solvate ions leading to autoionization and separated ion-pair formation.

The reduction in the H^+ and H_2^+ yields upon the addition of HCl also shows the importance of dangling bonds in the solvation and incorporation of HCl into the ice sample. The addition of HCl decreases the proton yield by reducing the number of dangling hydrogen atoms available. This reduction is due to the formation of a solvation shell around the Cl^- . These results also agree with calculations which show that dangling bonds, especially on step and edge sites can play important roles in HCl solvation.[88, 100] If one assumes that the proton comes solely from surface defects, the experimental yield at 90K indicates an intrinsic CI surface defect density of $\sim 10^{12} \text{ cm}^{-2}$. Assuming $10^{15} \text{ sites/cm}^{-2}$ for a hexagonal bilayer, this is 10^{-3} of the total surface sites available. The reduced proton signal and the HCl low coverage dependence implies HCl ionization involves multiple hexagons and sub-surface lattice displacements. The increased cluster ion yields at increased HCl dosing temperatures also indicate that ionization is not complete at 80 K. This is consistent with previous results using different techniques.[23]

3.4.3 Temperature programmed desorption

There are numerous investigations into the TPD of HCl from ice over a wide range of dosing temperatures, HCl dose rates, ice phase, and annealing history of the ice.[24,

29-32, 101-104] Both Harnett et al.[30] and Graham and Roberts[29] measured lower temperature features which were dependent on several factors such as total HCl dose, saturation of the underlying ice film, annealing history, and dosing temperature. Harnett et al.[30] found that HCl dosing below 130 K results in an HCl enriched surface layer that leads to HCl desorption before water desorption and proposed the formation of HCl trihydrate at the surface. Graham and Roberts[29] show a similar feature in their TPD spectrum and attribute this feature to an adsorbed state only occurring after saturation of the water film to form HCl hexahydrate. Sadtchenko[101] explored HCl interaction with thick films and found that the annealing history of the ice played a major role in the HCl desorption profile.

The variety of conditions used by various groups highlights the importance of understanding the fundamental interaction of the HCl with the ice surface before adding complications such as hydrate formation and HCl-HCl interactions. TPD measurements were taken as a complimentary probe to our ESD measurements and show that with low HCl concentrations, the HCl is strongly interacting with the water molecules and exists in the ionized form at all temperatures studied. The degree of ionization depends upon both the temperature and coverage and is nearly complete except at the lowest HCl dosing temperatures. The desorption feature measured after all of our ESD measurements support the ESD observations of an ionized species which influences the local bonding network of the ice. TPD measurements of non-irradiated ice under the same dosing conditions used for the ESD measurements show identical results, an indication that the electron bombardment is not inducing the HCl ionization on the ice surface.

Some useful information can be gleaned from the higher HCl dose TPD experiments. It is clear that the TPD feature labeled I in Figure 3.5 is evidence of a very strongly interacting HCl species, intimately tied to the water and most likely ionized.

Rising edge analysis of the multilayer water desorption peak gave a zero order activation energy of 41 ± 2 kJ/mol, in agreement with previous studies using TPD[104] and isothermal desorption.[105, 106] The activation energy of the ionized HCl desorption feature (I) was found to be 43 ± 2 kJ/mol using the Polanyi-Wigner equation.[74]

$$I(t) \propto \frac{dm}{dt} = -\frac{d\theta_m}{dt} = V(\theta_m) \cdot \theta_m^n \cdot \exp \left[-\frac{E_{des}(\theta_m)}{R \cdot T} \right] \quad (1)$$

where

$V(\theta_m)$ = the frequency factor

θ_m = instantaneous coverage

n = desorption order

$E_{des}(\theta_m)$ = activation energy

R = gas constant

T = temperature (K)

Assuming second order kinetics and a normal frequency factor of $10^{13} \text{ ML}^{-1}\text{sec}^{-1}$. The calculated activation energy of the HCl desorption is close to that of the water from ice most likely because the water desorption/diffusion is controlling the rate at which the ionized species recombine.

The nature of peak II in Figure 3.5 suggests some interaction of the HCl in which the HCl molecule is interacting with either the water ice or the ionized HCl species that seems to remain on or near the ice surface. The Cl^- ion is most likely located on or near the surface of the ice when the first molecules are initially ionized.[23, 107, 108] The subsequent incoming HCl molecules then find a different surface than the dangling hydrogen bonds present on the pure ice samples. The HCl molecule can interact with the Cl^- ion through the proton, forming a Cl^- -HCl complex. It is also possible that this interaction is a lower hydrate complex $(\text{HCl})(\text{H}_2\text{O})_n$ where $n = 1-3$, as suggested by Sadtchenko et al.[101] However, because this HCl desorbs prior to the

water, it is more likely the HCl molecule interacting with the Cl^- forming a trapped molecule at the surface.

The lowest temperature peak (III) is most likely physisorbed HCl which is only weakly interacting with the surface. This occurs at dosing temperatures below 110 K and is the weakest interaction of HCl with the ice sample. These TPD measurements have shown that the first interaction of HCl with ice forms a strongly interacting and most likely ionized complex, and only at higher doses are subsequent interactions seen. These subsequent interactions can be formation of a hydrated surface species, interaction of the HCl with the ionized Cl^- ions, or physisorption on the ice surface.

3.5 Conclusions

The interaction and autoionization of HCl on ice was probed using low-energy electron stimulated desorption (ESD) and temperature programmed desorption (TPD). The ESD of H^+ , H_2^+ , and $\text{H}^+(\text{H}_2\text{O})_n$, $n = 1-8$ yields provided insight into the dynamic response of the terminal water molecules on an ice surface. Submonolayer concentrations of HCl produced a large reduction in the H^+ and H_2^+ signals as well as an increase in the protonated cluster yield ($\text{H}^+(\text{H}_2\text{O})_n$, $n = 1-8$). These results are interpreted as rapid ionization of HCl at the surface at temperatures as low as 80 K. The surface of the ice becomes disordered as HCl autoionizes and forms contact ion pairs, leading to reduced numbers of dangling bonds at the surface and increased hole localization. The decrease in the proton yield upon HCl dosing shows the importance of dangling bonds in HCl adsorption and ionization, in agreement with recent QM/MM calculations.[88, 100] The increase in the cluster yield with HCl results from the disorder present at the surface of the ice. The results are supported by TPD measurements with HCl desorption occurring ~ 150 K commensurate with bulk ice. TPD measurements show the presence of molecular HCl at dosing temperatures below 120 K however the dose required to adsorb molecular HCl is strongly dependent on the

annealing history of the ice. The results indicate that ice surfaces are very dynamic and can cause the dissociation of acidic molecules at temperatures lower than those expected in the stratosphere. The study also demonstrates the utility of ESD to probe reactions occurring on low temperature ice surfaces.

CHAPTER IV

PHOTOIONIZATION OF LIQUID WATER AND AQUEOUS SOLUTIONS USING A MICROJET.

4.1 *Introduction*

Processes at the air water interface are known to play very important roles in atmospheric chemistry, with liquid aerosol droplets serving as catalysts.[5] Examples of such surface specific reactions include the hydrolysis of SO_2 , [6-8] and the reaction of ClONO_2 with HCl . [9] However, despite its importance, investigating properties of liquid surfaces especially in vacuum has often proved difficult. This is because traditional surface science techniques requires an ultra high vacuum environment to prevent distortion of information due to interference from equilibrium vapor above the liquid surface during data acquisition. In order to circumvent this problem, Faubel et al. developed the liquid jet technique for introducing a continuous micron sized liquid jet in vacuum. [33-35] By using a liquid jet with diameter d , that is comparable to the mean free path in the equilibrium vapor, the chance of a collision with molecules in the vapor for particles leaving or entering the liquid surface is reduced.

$$\lambda(cm) = \frac{c}{P_v(Torr)} \quad (1)$$

Figure 4.1 shows the schematic diagram of a typical liquid jet. To avoid molecular collision with the equilibrium vapor in region B, the diameter of the nozzle must be less than free mean path of the gas phase. Under this condition, the ejected ions from the surface of the liquid jet move directly from the liquid jet mainstream (region A) into region C which is governed by molecular flow. According to equation 1, for pure water with a vapor pressure $P_v = 4.58$ Torr at the freezing point 273 K and c

$= 5.3 \times 10^{-3}$ Torr.cm, the free mean path (λ) = 11.57 μm , therefore, using a liquid jet with 10 μm diameter will eliminate collision of ejected ion with the dense vapor pressure.[33]

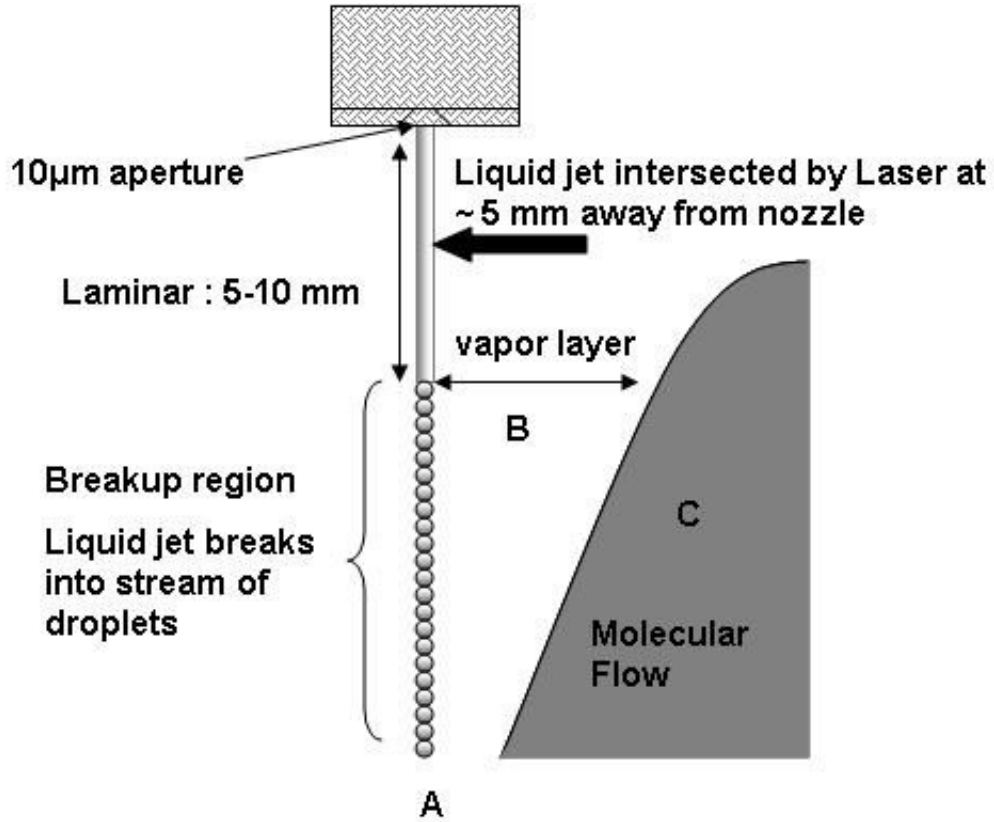


Figure 4.1: Schematic of a 10 μm liquid jet. The liquid jet (A) is surrounded by a collisional atmosphere (B), the size of which depends upon the jet diameter, and beyond which the number density of evaporating molecules drops as $1/r$ in a collision free zone (C). The density of B as well as the liquid temperature can be modeled by Clausius-Clapeyron evaporative cooling model. [40]

The liquid jet techniques also facilitates the direct study of continually renewed liquid surface in high vacuum thereby preventing the constant changing of the properties and composition of the liquid surface due to aging process (diffusion of impurities or liquid constituent).

Several groups have used several versions of this design to study liquid interfaces

using traditional techniques such as ultraviolet photoelectron spectroscopy (UPS)[36-38] and X-ray spectroscopy (XPS).[39-41] The liquid jet technique is also valuable for laser ionization and has been employed to examine the gas liquid interface of aqueous solutions.[42-45] Monitoring ejected ions from UV laser ionization of liquid jets with time of flight mass spectrometry was pioneered by Kondow and co-workers.[44] However, this body of work was done exclusively on relatively high solute concentrations and on organic solvents. In an earlier article, we reported for the first time, the use of the liquid jet technique to probe the ejection water clusters from the gas/liquid interface of aqueous sodium halide (Na^+X^- , $\text{X}=\text{Cl}, \text{Br}, \text{I}$) salt solutions at concentration range between 10^{-4} and 10^{-1}M . [109] The yield of ejected protonated water clusters ($\text{H}^+(\text{H}_2\text{O})_n$) varied inversely with increasing salt concentration, while the solvated sodium ion cluster ($\text{Na}^+(\text{H}_2\text{O})_m$) yield varied by anion type. The distribution of water clusters (for $n, m \geq 2$) at low salt concentration was identical to that observed from low-energy electron irradiated amorphous ice[92] and the production of these clusters was accounted for using a localized ionization/Coulomb expulsion model. Since these clusters are ejected exclusively from the surface of the liquid and the cluster distributions are influenced by the local structure, these experiments provide a sensitive probe of the liquid vacuum interface of these solutions.

The purpose of the present study is to extend the investigation of ion ejection from the interface of aqueous solutions. Specifically, cluster ion ejection from photoionization of aqueous solutions of NaOH , NaCl and HCl are investigated at different concentrations. A detail study of water clusters ejection from pure water, D_2O and mixture of both is also presented.

4.2 *Experimental Details*

The liquid jet chamber used for investigating liquid in vacuum was constructed and used at PNNL in collaboration with Nikolai Petrik and Greg Kimmel. The chamber

consists of three components (Figure 4.2): a liquid jet delivery system mounted on a XYZ translational stage, a vacuum chamber equipped with a time of flight mass spectrometer (~ 120 cm) and a liquid nitrogen cryotrap for maintaining a base pressure between 10^{-6} and 10^{-5} Torr while the liquid jet is running. The liquid delivery system consists of a Shimadzu HPLC pump that delivers solution at a constant flow rate and a 6 way selection valve for dispensing solutions with different concentrations during experiment. In-line filters are employed at different parts of the liquid delivery system to prevent clogging of the aperture. The jet design consists of a $10\text{ }\mu\text{m}$ sized stainless steel aperture clamped between a stainless steel metal cap and PEEK (polyether ether ketone) tubing. With the stainless steel aperture and metal cap, voltage can be applied to the nozzle or grounded if necessary.

The liquid jet is mounted vertically downward on the x-y-z translational stage into the vacuum chamber. Eventually, the liquid jet contracts to $\sim 6\mu\text{m}$ [42, 110, 111] and possess a final velocity of $\sim 78.5\text{ m/s}$ (at a constant flow rate of 0.3 ml/min). The calculated Reynolds number (Re) for a liquid jet that passes through a $10\text{ }\mu\text{m}$ aperture under these conditions is ~ 800 . $\text{Re} < 2000$ indicates the liquid jet under these conditions is operated as a stable laminar flow. However, in practice, the laminar region of the liquid jet only extends to 5–10 mm in length before breaking up into a continuous stream of droplets that could extend several centimeters away from the nozzle.[40] Probing the liquid jet within this laminar flow required redesigning the TOF mass spectrometer that was previously reported.[109] The TOF mass spectrometer was redesigned with adjustable repeller and extraction tubes (diameter ~ 6.25 mm). This design allows the liquid jet to be probed at 5 mm away from the nozzle (figure 4.3).

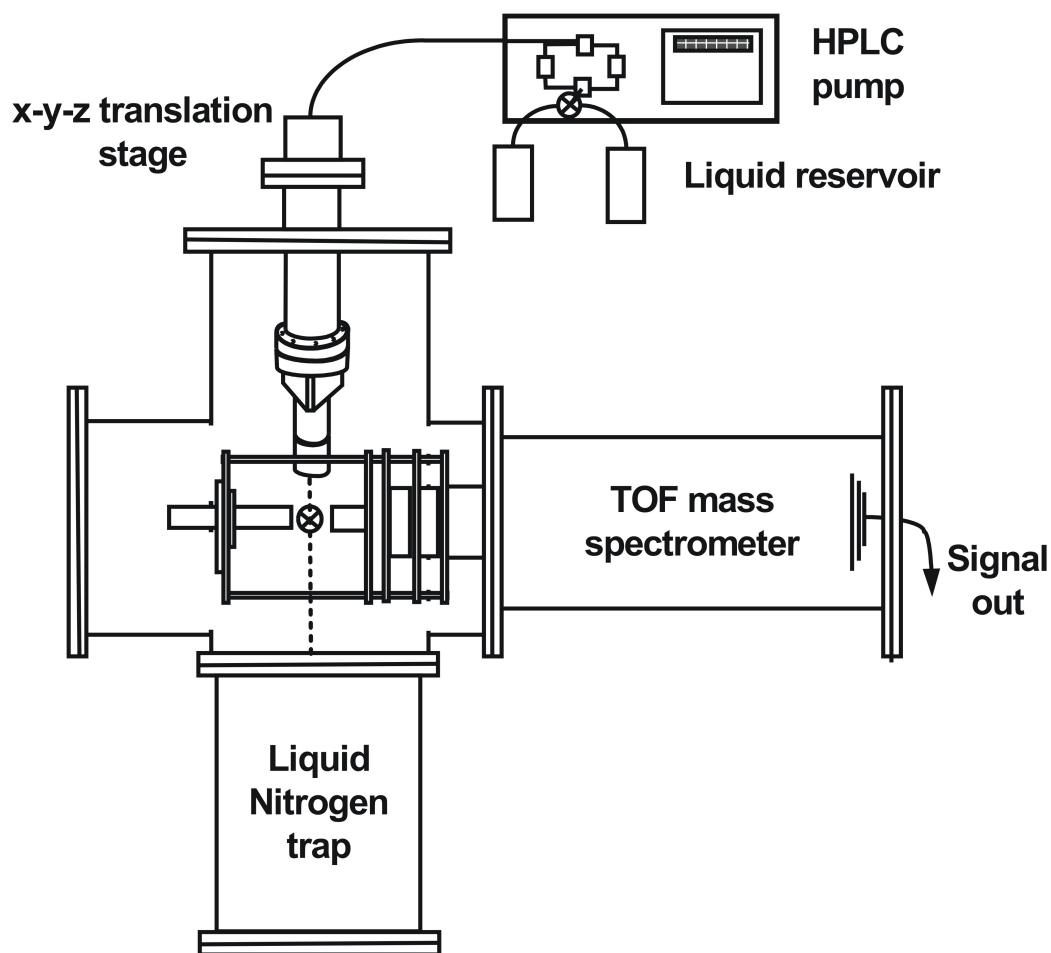


Figure 4.2: Custom made liquid jet chamber designed at Pacific Northwest National Laboratory (PNNL). The liquid jet streams downward into a liquid nitrogen cold trap. The liquid jet is adjusted with respect to the focused laser beam in the middle of the repeller and extraction plate of the TOF mass spectrometer to optimize ion yield.

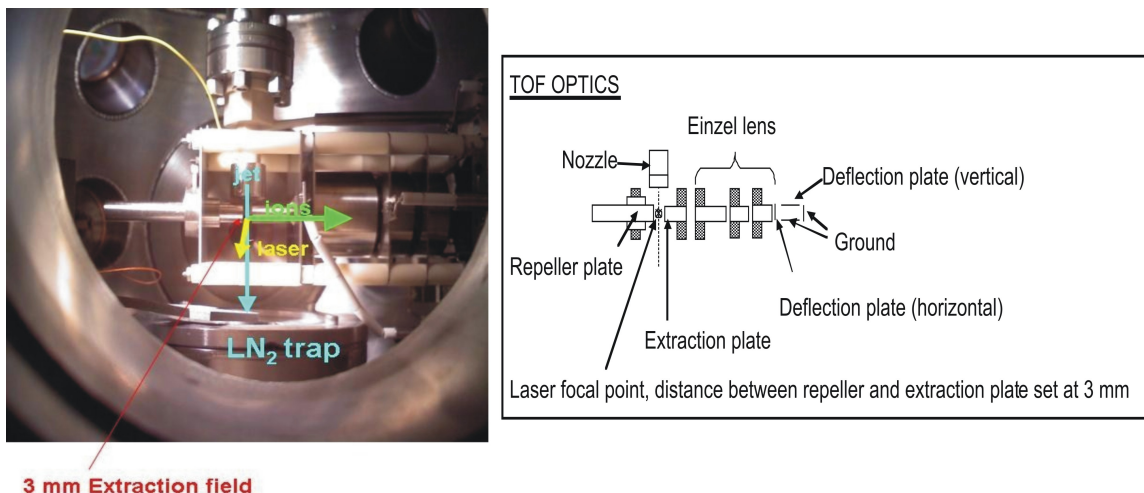


Figure 4.3: The custom-built Liquid jet Chamber at PNNL with a new time-of-flight optics.

Due to evaporative cooling, the liquid jet forms icicles upon touching the surface of the liquid nitrogen cryotrap. Two mechanical choppers were attached above the cryotrap to help reduce the formation of icicles by slicing the frozen ice. In conjunction with the cryotrap, two turbomolecular pumps are used to differentially pump the main chamber to give a pressure of 10^{-5} Torr. The TOF chamber has a pressure of 10^{-6} Torr while running the liquid jet. The calculated temperature of the liquid jet at 5 mm is approximately 277 K.[33]

A GAM ArF EX 10F Excimer laser (193 nm) was used for the photoionization of the liquid jet and was operated between 100 and 400 $\mu\text{J}/\text{pulse}$, with a shot to shot variation of about 10 to 20 $\mu\text{J}/\text{pulse}$. The laser beam is focused on the liquid jet which is positioned geometrically in the middle of the chamber, between the repeller and the extractor plates of the TOF mass spectrometer. Since both the laser and jet are on x-y-z translation stages, different parts of the liquid jet can be effectively sampled either by moving the liquid jet across or up and down with the laser beam position fixed.

Typical experiments involve irradiating the liquid jet (at 5 mm distance away

from the nozzle) with a focused laser beam ($\sim 250 \mu\text{J}/\text{pulse}$). The jet was placed in the middle of a 3 mm extraction field (distance between repeller and extraction plate). Ejected ions were detected using the linear TOF mass spectrometer. For photoionization of aqueous solutions of different concentration, the six-way valve attached to the HPLC pump was employed to switch from one solution to another. A complete flushing of previous solution takes approximately 10 minutes at a constant flow rate of 0.3 ml/min. Liquid jets containing pure water and aqueous solutions of NaCl, NaOH and HCl at concentrations ranging between 10^{-4} M and 2.5×10^{-2} M were investigated at a constant flow rate of either 0.3 or 0.5 ml/min. Blank experiments involving the photoionization of pure water was carried out in between switch out to a different concentration.

4.3 Results

A typical mass spectrum of positively charged ions ejected from laser irradiation of the liquid jet containing deuterium oxide and pure water is shown in figure 4.4 a and 4.4 b respectively. In each case, the most prominent ion ejected is unsolvated D_3O^+ and H_3O^+ with intensity that is ~ 10 times higher than the next water cluster ion. Other cation water clusters of the type $\text{D}^+(\text{D}_2\text{O})_n$ and $\text{H}^+(\text{H}_2\text{O})_n$ were observed with cluster size $(n) \leq 6$.

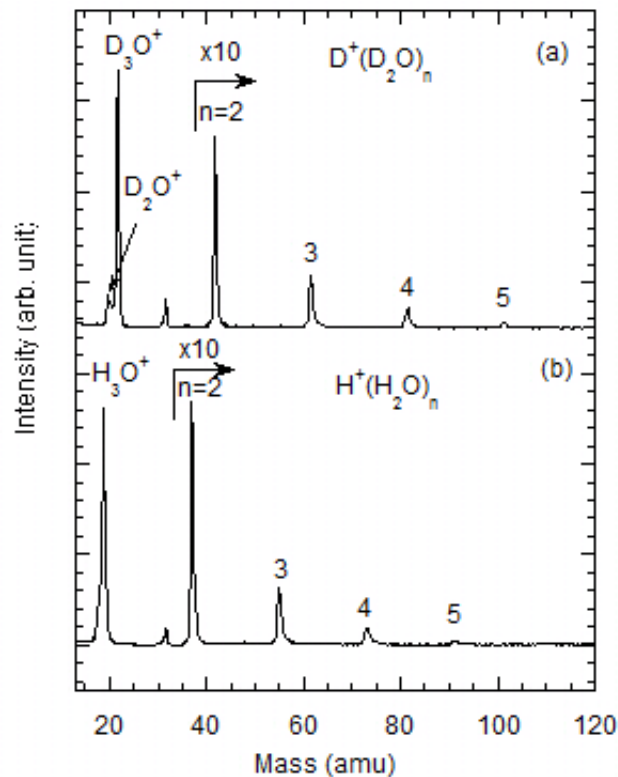


Figure 4.4: Time-of-flight mass spectrum of ions ejected during photoionization of a) D₂O and b) pure water. Cation clusters of the type H⁺(H₂O)_n and D⁺(D₂O)_n are observed respectively for H₂O and D₂O, with $n \leq 6$.

In addition to protonated water clusters, photoionization of both NaCl and NaOH solutions also produced unsolvated Na⁺ and sodium water clusters of the type Na⁺(H₂O)_m. Figure 4.5 shows mass spectra of ions ejected into the gas phase after photoionization of 10⁻⁴, 10⁻³ and 5×10⁻³ M NaCl and NaOH solutions. H₃O⁺ and H⁺(H₂O)_n intensities decrease with concentration while both unsolvated Na⁺ and Na⁺(H₂O)_m clusters increase with concentration.

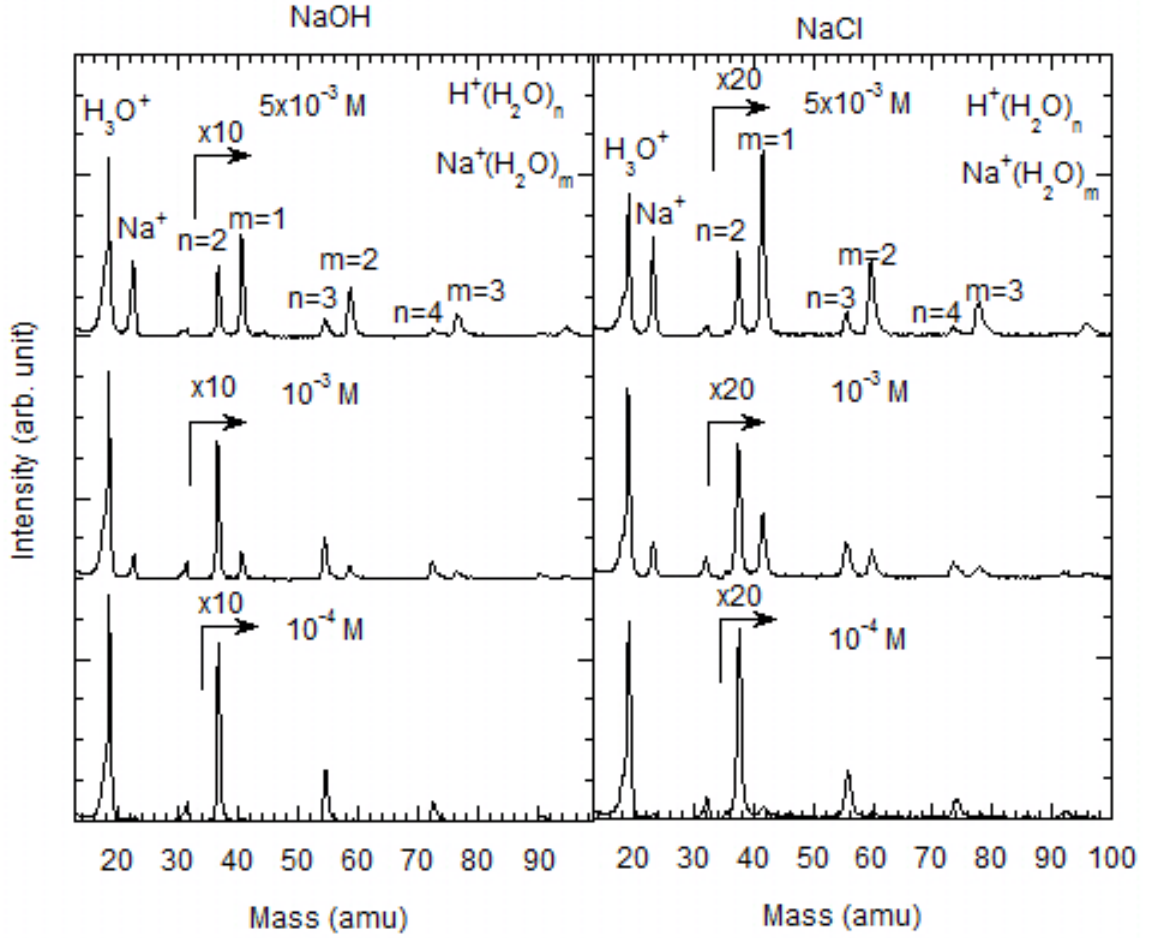


Figure 4.5: Typical TOF spectrum of ions ejected during photoionization of 10^{-4} , 10^{-3} and 5×10^{-3} M NaCl and NaOH. Unsolvated H_3O^+ and Na^+ and both water clusters of the type $\text{H}^+(\text{H}_2\text{O})_n$ and $\text{Na}^+(\text{H}_2\text{O})_m$ are observed ($n, m \leq 6$). H_3O^+ and protonated water clusters decreases with concentration while Na^+ and sodium water clusters increases with concentration.

Figure 4.6 shows the integrated intensities of ejected ions as a function of salt concentrations. For both aqueous solutions of NaCl (top panel), and NaOH (lower panel), H_3O^+ and protonated water clusters of the type $\text{H}^+(\text{H}_2\text{O})_n$ ($n > 2$) dominates at the lowest concentration (10^{-4} M) whereas primarily Na^+ and $\text{Na}^+(\text{H}_2\text{O})_m$ clusters are observed at the highest concentration studied (2.5×10^{-2} M). A similar experiment was performed for aqueous solution of HCl. Irradiating the liquid jet with laser

resulted in the ejection of unsolvated H_3O^+ and $\text{H}^+(\text{H}_2\text{O})_n$ ($n = 2-6$) for all concentrations. The yield of these ions remained constant and showed no significant change as a function of concentration (figure 4.7). The total yield of ejected ions for all solutions is approximately the same at all concentration studied. As shown in figure 4.8, the ratio of unsolvated H_3O^+ and the total yield of measurable protonated water cluster ($\text{H}^+(\text{H}_2\text{O})_n$, $n = 2-4$) increases with concentration for both NaOH, NaCl while that of HCl solution remained constant. Also, for both NaOH and NaCl aqueous solutions, the ratio of unsolvated Na^+ and the sum of measurable sodium water cluster ($\text{Na}^+(\text{H}_2\text{O})_m$, $m = 1-3$) remained relatively constant as the concentration is increased (data not shown).

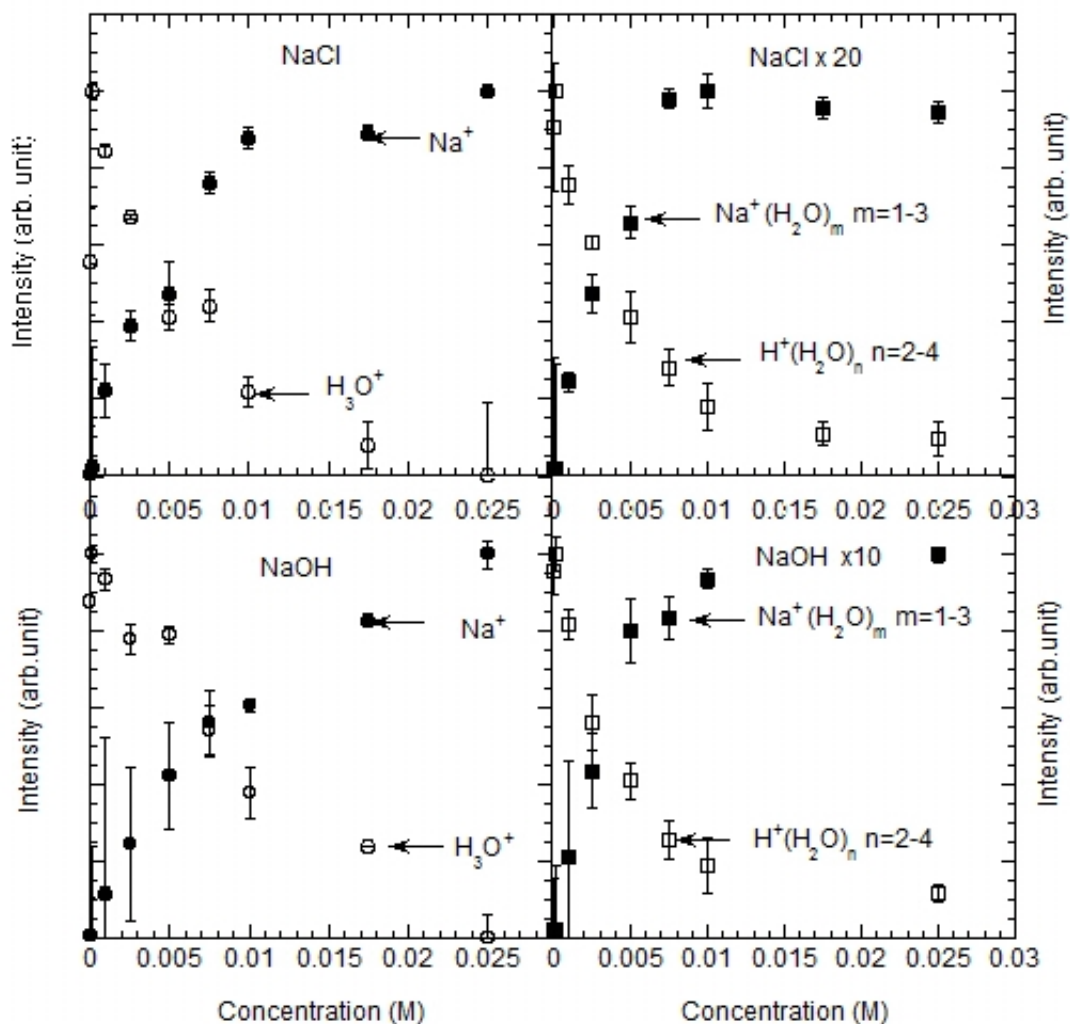


Figure 4.6: Experimentally observed ion yield as a function of concentration of aqueous NaCl (top panel) and NaOH (bottom panel) solutions. Shown are yields of unsolvated ions: H_3O^+ and Na^+ ; protonated water clusters $\text{H}^+(\text{H}_2\text{O})_n$, $n = 2-4$ and sodium water clusters $\text{Na}^+(\text{H}_2\text{O})_m$, $m = 1-3$. Both the hydronium ion and protonated water clusters yield varied inversely with increasing concentration while both sodium ion and sodium water clusters yield was proportional to concentration.

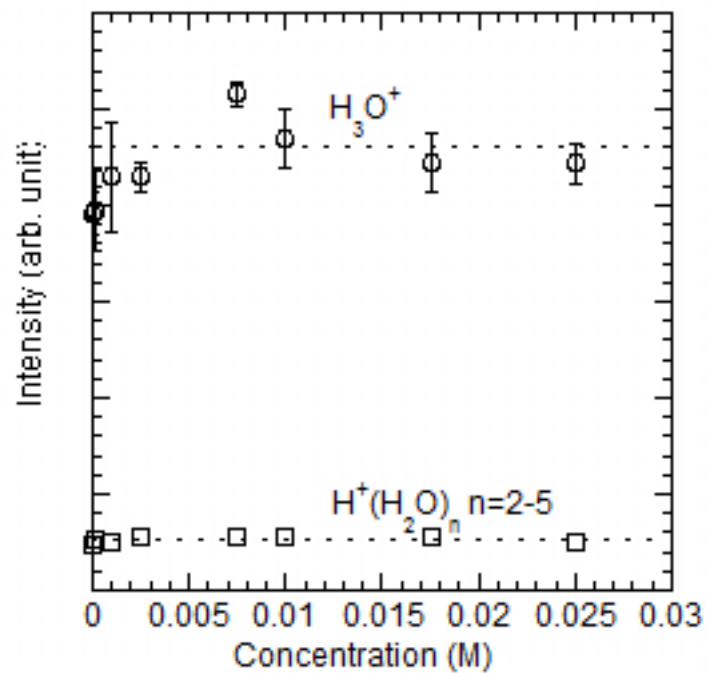


Figure 4.7: Experimentally observed H_3O^+ and $H^+(H_2O)_n$ $n = 2-5$ yields as a function of concentration for aqueous solution of HCl. Unlike aqueous solution of NaCl and NaOH, the protonated water cluster yield remains constant with increasing HCL concentration.

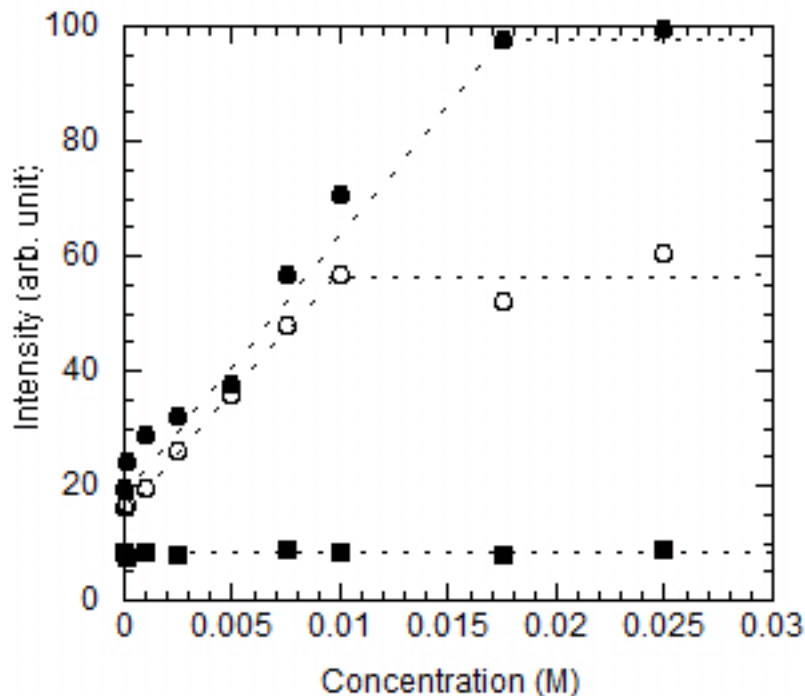


Figure 4.8: Plots of the ratio of unsolvated hydronium ion (H_3O^+) and the sum of measurable protonated water clusters as a function of concentration for HCl (solid square), NaCl (solid circle) and NaOH (open circle). Each data set represents $\text{H}_3\text{O}^+ / \Sigma \text{H}^+(\text{H}_2\text{O})_n$ for $n > 2$. While the yield of both H_3O^+ and protonated water cluster decreases with concentration, their ratios increases with concentration for both NaOH and NaCl but remains constant for HCl solutions(dashed lines serve as guides).

4.4 Discussion

4.4.1 Characterization of liquid jet

The ejected ions reported in this study are only observed when the focused laser beam irradiates the liquid jet. This implies that ejected ions originate from the liquid jet and not in the gas phase. By moving the liquid jet in small increments ($10 \mu\text{m}$) across the laser beam the ejection of ions as function of the effective overlap of both the focused laser beam and liquid jet can be monitored. Because the liquid jet and the laser were placed on x-y-z stages, the relative positions of both beams are known. Figure 4.9 (a) shows the yield of unsolvated ions (H_3O^+ , Na^+) observed from the

photoionization of pure water and 5×10^{-3} M NaCl. No ion signal was observed when the liquid jet was positioned near the focused laser beam while the maximum yield is observed when the laser and liquid jet overlaps. Solvated ions ejected from the liquid jet also have similar trends (data not shown). Since the focused laser beam is much larger than the liquid jet (Figure 4.9 b), contributions from the gas phase can not be completely ruled out. However, ions that originate from the liquid jet can be easily distinguished from those that originate from the vapor phase because ions ejected from the liquid jet are expected to contain more than one solvent molecule while those from the vapor phase are not.[44, 112] Figure 1a shows that the yield of gas phase D_2O^+ signal compared to the D_3O^+ signal is negligible. The D_2O^+ signal is attributed to the gas phase because in liquid phase the initial ion formed, D_2O^+ reacts rapidly with surrounding D_2O molecules to yield D_3O^+ and OD radical.[113]

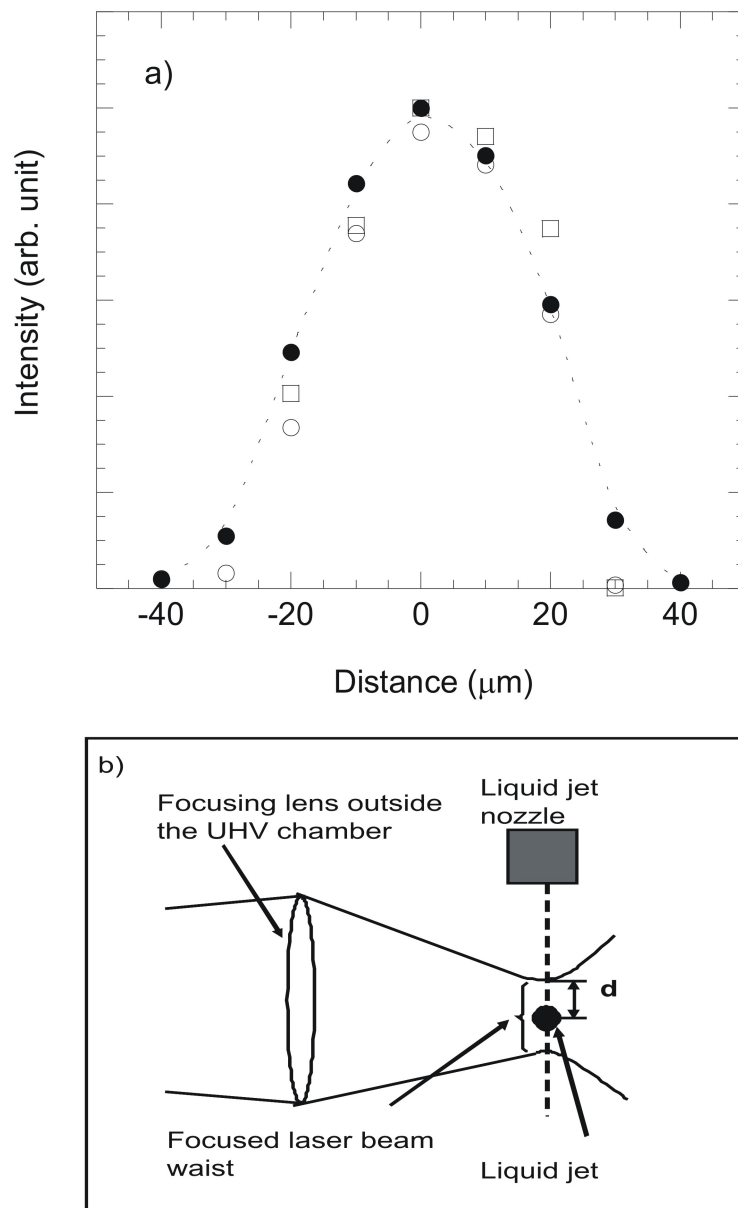


Figure 4.9: a) Intensities of unsolvated H_3O^+ ejected from photoionization of pure water (solid circle) and 5×10^{-3} M NaCl (open circle); and bare Na^+ (open square) ejected from the photoionization of 5×10^{-3} M NaCl plotted as a function of the distance between the centers of the focused laser beam and the liquid jet. Other water clusters have similar trends. b) Schematic of the effective overlap of the liquid jet ($\sim 6 \mu\text{m}$) and the focused laser beam (\sim spot size $35 \mu\text{m}$).

Upon irradiation, the solvent water molecules are ionized while the photoelectrons formed are either ejected into the vacuum or recombine with cations in the bulk on

the picosecond time scale.[114] The ejection of these photoelectrons results in charge build-up and the accumulation of positive charges on the surface. For pure water and HCl solutions, H_3O^+ accumulates on the surface while in the case of NaOH and NaCl solution both Na^+ and H_3O^+ compete. Since the ejection of photoelectrons can be said to occur on the surface of the liquid (photoelectron mean free path is $\sim 10 \text{ \AA}$) the ejection of ions also occurs primarily from the surface of the liquid jet. If we consider a uniform distribution of ionization throughout the jet, photoelectron ejection from the surface of the liquid jet should lead to uniform distribution of excess positive charge on the surface. The surface concentration of ions is expected to be significantly different from that of the bulk due to evaporative loss of water molecules. The relative amount of the solute-solvent interactions on the liquid jet surface for both NaOH and NaCl at low concentration (10^{-4} M) is considered small because sodium water clusters can not be detected and only protonated water clusters are measurable with our experimental set-up. By increasing the concentration of NaOH and NaCl, both unsolvated Na^+ and sodium water clusters increases as a result of sufficient increase in the relative amount of solute-solvent interactions at the surface of the liquid jet. Figure 4.6 shows that by increasing the hydronium ion concentration of HCl solutions the amount of ions ejected remained constant as the concentration increase. This result suggests that the solvated H_3O^+ in the bulk do not migrate to the surface. With a flow rate of 0.3 ml/min ($\sim 64 \text{ m/s}$), the available time for ions to migrate to the surface is $\sim 78 \mu\text{sec}$ since the liquid jet is irradiated by the laser at distance of 5 mm away from the nozzle. The average distance that ions travel and the number of molecules on the surface of the liquid jet during this time can be calculated. According to Fick's law of diffusion,[115] the average distance (L) that ions travel in liquid medium during a certain time (t) is given by equation 2.

$$L = \sqrt{4Dt} \quad (2)$$

With a diffusion coefficient of $2 \times 10^{-5} \text{ cm}^2/\text{s}$ an average diffusion length (L) of approximately $0.8 \text{ }\mu\text{m}$ is obtained. Hence, only molecules within this distance are able to diffuse to the surface before laser irradiation. A distance of $0.8 \text{ }\mu\text{m}$ corresponds to approximately 2500 monolayers of water. From this calculation, we can also infer that although the ratio of water molecules to Na^+ in the bulk is $\sim 2000:1$ for the highest concentration ($2.5 \times 10^{-2} \text{ M}$) the effect of diffusion and evaporative cooling increases the concentration at the surface considerably. This implies that the ejection of ions occur on the surface of the liquid jet where the ions are mostly likely inhomogeneously solvated.

The propensity for Na^+ to migrate to the surface also limits the amount of water molecules available for the solvation of H_3O^+ formed during laser irradiation. As shown in figure 4.8, the ratio of H_3O^+ and protonated water clusters $\text{H}^+(\text{H}_2\text{O})_n$, $n \geq 2$) increases for both NaOH and NaCl solutions but remain constant for HCl. However, the total ion yield for all 3 solutions and the ratio of Na^+ to sodium water clusters ($\text{Na}^+(\text{H}_2\text{O})_m$, $m \geq 2$) for both NaOH and NaCl solutions remains relatively constant for all concentrations (data not shown). Recent molecular dynamics simulation by Jungwirth and co-workers [35] adapted for bulk liquids predicts the depletion of small cations like Na^+ from the surface of aqueous solutions. However, as discussed above, the ejection of electrons into vacuum during laser irradiation forces positive charges to migrate to the surface. The formation of $\text{Na}^+(\text{H}_2\text{O})_m$ on the surface of the liquid jet will ultimately distort the hydrogen bonded water network found in the bulk. At higher concentration, the Na-water interactions become strong enough that one might expect the formation of clusters containing Na-Cl or Na-OH ion pairs on the surface of the liquid jet. The presence of these ion pairs and the strong Na-water interactions is also known to result into breaking of the water hydrogen bond network.[116] The observed decrease of protonated water clusters and increase of sodium water clusters with concentration can therefore be attributed to the increase in concentration of Na

ions on the surface during laser irradiation.

4.4.2 Ion ejection mechanism

The surface depletion of electrons during laser irradiation results in formation of excess positive charges on the surface of the liquid jet. The Coulomb repulsion generated by these charges causes ejection of ions into the gas phase.[44, 109] The power dependence measurement for ejection of ions from pure water (Figure 4.10 a) shows a threshold value of $\sim 100 \mu\text{J}/\text{pulse}$. As the laser power increases, the intensity of ejected ions increase but levels off at $\sim 300 \mu\text{J}/\text{pulse}$. This result implies that there is a critical charge density below which there is no ion ejection. There is also a maximum number of charges that can be available on the surface; once this value is reached, the ejection of ions remains constant. A derived slope of 2 as shown in Figure 4.10 b indicates a two photon ionization process.

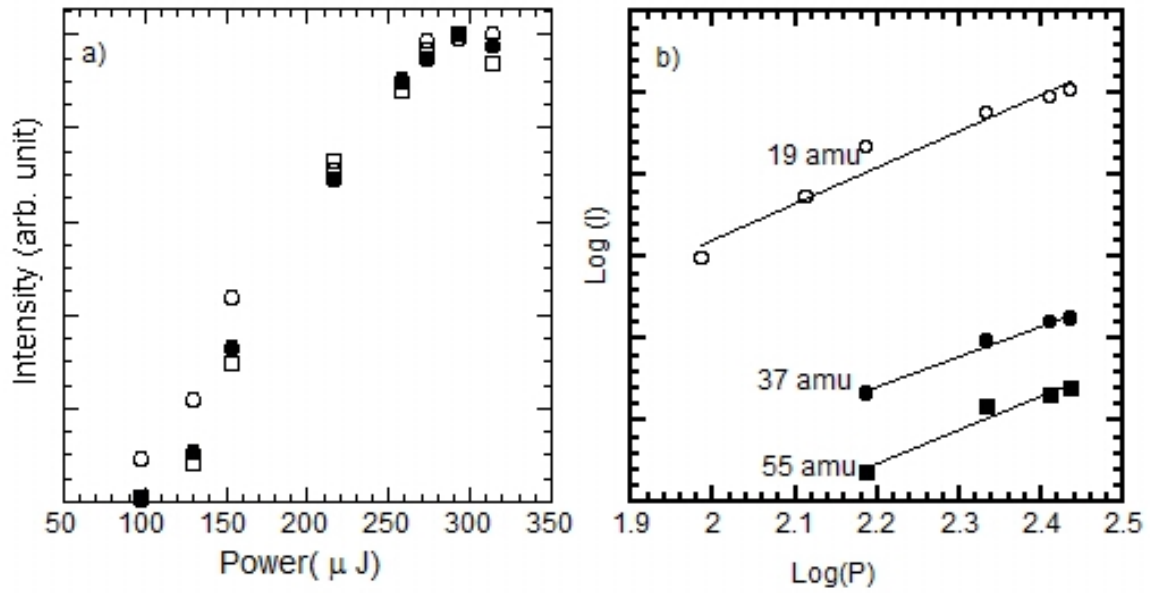


Figure 4.10: Power dependence measurement. a) Ion yield for each ion, H_3O^+ (open circle), $\text{H}^+(\text{H}_2\text{O})_2$ (solid circle) and $\text{H}^+(\text{H}_2\text{O})_3$ (open square) plotted as a function of laser power; a threshold exists around $100\mu\text{J}$. b) Log-log plot with a slope of 2.

As shown in Figure 4.11, the observed water clusters during photoionization of NaCl and NaOH solutions are formed as a result of the photoionization of the solvent water within the first solvation shell and the Coulomb repulsion from the solvated Na^+ . Two possibilities can be considered regarding the ejection of ions observed in the present study. Either they are ejected as a large cluster which subsequently evaporates to the range of ions observed in the time-of-flight mass spectra or they are ejected as ions already in their final size range. A conclusion from earlier investigation in our laboratory is that ions existing on the surface have the probability to extract a number of neighboring water molecules from the bulk during the ionization-ejection event.[109] To extract neighboring water molecules, the energy of hydrogen bonding to the bulk must be overcome but the subsequent formation of ion-dipole bonds to the cluster helps to recover some of the energy lost. The binding energy of water clusters decreases with increasing number of water molecules while the number of bonds required to extract a cluster (hydrogen bond energy) increases geometrically with increasing cluster size. In other words, the probability of extracting ions decreases drastically with increasing cluster size. The ion ejection mechanism suggested by Kondow et al. however, predicts the ejection of a large nascent cluster that breaks into a range of smaller clusters before detection.[117] The model is based on formation of large clusters with hot internal energy which results in unimolecular dissociation and losses in cluster size prior to detection. While this mechanism can not be completely ruled out, the absence of a magic number cluster ion which is supposed to be formed as a result of unimolecular decomposition of an excited large cluster ion suggest this mechanism is not dominant.[118-120] The size of the magic number observed in these studies is known to vary according to the internal energy of the large cluster ion, but in all cases the most stable geometrical structure of the daughter ions are clearly observed as the ion with the highest yield. It remains probable that some ejected ions originate from gas phase and further work is required to fully characterize

the mechanistic details of different processes occurring during ion ejection.

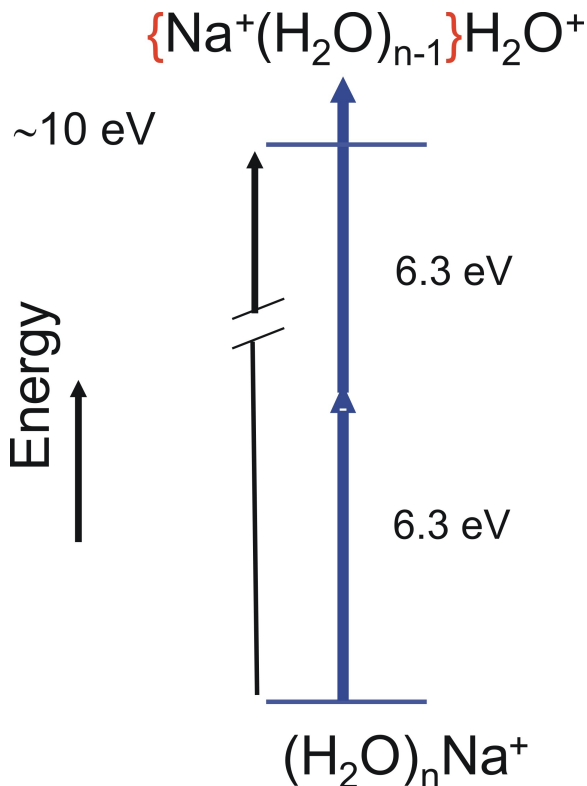


Figure 4.11: Mechanism for photoejection of water clusters from aqueous solutions of NaCl and NaOH.

4.5 Conclusions

Monitoring the ejection of ions from laser irradiation of a liquid jet with time-of-flight mass spectrometer provides a useful approach to probe liquid surfaces under pristine vacuum conditions. The liquid jet technique was employed to investigate the ejection of ions from the surface of pure water, NaCl, NaOH and HCl aqueous solutions. Unsolvated H_3O^+ and protonated water clusters of the type $\text{H}^+(\text{H}_2\text{O})_n$ were produced and ejected from the surface of pure water and aqueous HCl solutions into the gas phase during laser irradiation at 193 nm. In addition to these ions, unsolvated Na^+ and solvated Na^+ clusters ($\text{Na}^+(\text{H}_2\text{O})_m$) were observed for both NaCl and NaOH solutions. The yield of these ejected ions was examined as a function of concentration.

The unsolvated H_3O^+ and protonated water cluster yield varied inversely with increasing concentration while the unsolvated Na^+ and sodium water cluster increases with concentration for both NaOH and NaCl solutions. However for aqueous HCl solutions, the ejected ions (both solvated and solvated) remained constant for all concentration. The trend observed was accounted for by the propensity of solvated Na^+ to migrate to the surface and distort the bulk hydrogen bond network of the bulk water molecules. The ejection of ions is explained by Coulomb expulsion of neighboring positive charged particles.

CHAPTER V

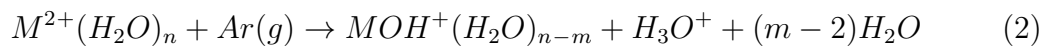
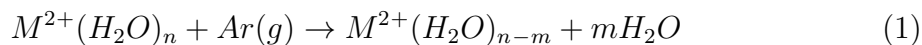
PHOTOIONIZATION OF LIQUID MICRO-JET CONTAINING ALKALINE EARTH METAL CHLORIDE, MCl_2 ($\text{M}=\text{Mg}^{2+}$, Ca^{2+} , Sr^{2+} and Ba^{2+}).

5.1 *Introduction*

Heterogeneous atmospheric reactions involving sea salts are known to be very important in the release of reactive halogens.[121] These reactive halogens are responsible for the destruction of ozone in the marine boundary layer. While NaCl is known to be the major constituent of sea water, it is by no means the only salt present. Apart from NaCl, sea water is composed of a combination of other organic salts such as alkaline earth metal chlorides especially magnesium chloride (MgCl_2). It has been reported that for every eight NaCl molecules present there is one MgCl_2 . [122] Understanding the liquid solvation of alkaline earth salts is not only fundamental to understanding heterogeneous atmospheric reactions, it is also important in biological processes. Aqueous Mg^{2+} is known to play very important roles in enzymes. Mg^{2+} also helps to stabilize complex biological structures like proteins, DNA and RNA.[123]

Given the importance of Mg^{2+} and other alkaline earth metals in atmospheric and biological processes, both experimental and theoretical [124-128] investigations have been done to understand the solvation of these ions mainly in gas phase. The general method used for probing hydration of singly charged ion clusters such as $\text{M}^+(\text{H}_2\text{O})_n$ in gas phase seldom works for doubly charged ions because hydrated divalent ions are less readily formed.[129] These gas-phase reactivity studies involves generation of $\text{M}^+(\text{H}_2\text{O})_n$ by forming M^+ from bare metal in gas phase in which molecular water vapor is present. A more successful technique for studying hydrated

doubly charged ions, $M^{2+}(H_2O)_n$ involves the use of electrospray pioneered by Kerbale et al.[130, 131] Since doubly charged ions exist in solution, the method permits the transfer of these ions from solution into gas phase. Subsequent collision induced dissociation of the $M^{2+}(H_2O)_n$ formed using argon yield a variety of species depending on the experimental conditions. Essentially, the collision activation of $M^{2+}(H_2O)_n$ using argon with a 5 eV collision energy resulted in either loss of water molecules (reaction 1) or proton transfer to form singly charged metal hydroxide and protonated water (reaction 2).[132] For these series of experiment, the number of water molecules observed varied greatly but appears to decrease with the second ionization potential (IP) of the metal.



The direct photoionization of aqueous solutions containing doubly charged ions without any subsequent gas-phase collision induced processes is presented. The experiment involves monitoring ejected ions from aqueous solutions of MCl_2 ($M=Mg, Ca, Sr$ and Ba) during laser irradiation by using a linear time-of-flight mass spectrometer.

5.2 *Experimental Details*

The experiments were carried out in the same liquid jet chamber describe in Chapter 4. Briefly, a liquid jet ($\sim 6 \mu m$) containing aqueous solutions of MCl_2 ($M= Mg, Ca, Sr$ and Ba) was introduced into the vacuum. A constant flow rate was maintained at 0.3 ml/min with a backing pressure of ~ 2.9 MPa inside the nozzle during experiment. After traveling a distance of 5 mm from the nozzle, the liquid jet was irradiated with a 193 nm laser beam focused at the center (by a lens with focal length 10 cm) of the 3 mm extraction region of the TOF mass spectrometer. Ions ejected into the gas

phase were monitored using the linear TOF mass spectrometer. The laser power use for these experiments was set to ($\sim 250 \mu\text{J}/\text{pulse}$) within the linear range reported in chapter 4. Commercially available MCl_2 were used without any further purification to make 10^{-4} M , 10^{-3} M , $5 \times 10^{-3} \text{ M}$ and 10^{-2} M aqueous solutions used for these experiments. A blank experiment which involves photoionization of pure water was done in between runs to eliminate any error due to variation of pressure observed after running the jet for a considerable length of time.

5.3 Results

Typical time-of-flight mass spectra generated from photoionization of liquid jet containing aqueous solutions of MgCl_2 , CaCl_2 , SrCl_2 and BaCl_2 are presented in figures (5.1-5.4) for different concentrations (10^{-4} M , 10^{-3} M , $5 \times 10^{-3} \text{ M}$ and 10^{-2} M). Singly charged unsolvated cations (M^+) are clearly visible for all alkaline earth metal chloride (MCl_2) solutions even at the lowest concentration (10^{-4} M). As shown in Figure 5.1, the photoionization of MgCl_2 solution yields predominantly unsolvated H_3O^+ and protonated water clusters $\text{H}^+(\text{H}_2\text{O})_n$ ($n=2-6$) at very low concentrations (10^{-4}M). Increase in concentration resulted in the decrease of these ions with corresponding increase in yield for unsolvated Mg^+ , MgOH^+ and water cluster ions of the type $\text{Mg}^+(\text{H}_2\text{O})_x$ ($x=1-2$) and $\text{MgOH}^+(\text{H}_2\text{O})_m$ ($m=1-4$). It is important to note that the total ion yield decreases with increase in concentration.

Protonated water clusters ejected from CaCl_2 show a similar trend as those obtained for MgCl_2 . Unsolvated Ca^+ and CaOH^+ and water cluster ions of the type $\text{CaOH}^+(\text{H}_2\text{O})_m$ were observed but $\text{Ca}^+(\text{H}_2\text{O})_x$ was completely absent. Both SrCl_2 and BaCl_2 solutions shows similar trend with the ejection of unsolvated M^+ , MOH^+ and water clusters of the type $\text{MOH}^+(\text{H}_2\text{O})_m$ ($m=1-4$).

In summary, water clusters of the type $\text{M}^+(\text{H}_2\text{O})_x$ was only observed for MgCl_2 solutions. However, unsolvated MOH^+ and water cluster ions of the type $\text{MOH}^+(\text{H}_2\text{O})_m$

were observed for all salt solutions. The relative yield of M^+ and MOH^+ are shown in figure 5.5. M^+ was predominantly observed for Mg, while an equivalent amount of M^+ and MOH^+ are observed for Ca and Sr. However, for Ba, mostly $BaOH^+$ was observed. Unsolvated H_3O^+ and protonated water cluster decrease with increasing in salt concentration while MOH^+ and $MOH^+(H_2O)_m$ increase with increasing concentration. For all salts, the increase in concentrations resulted in the reduction of total ion ejected.

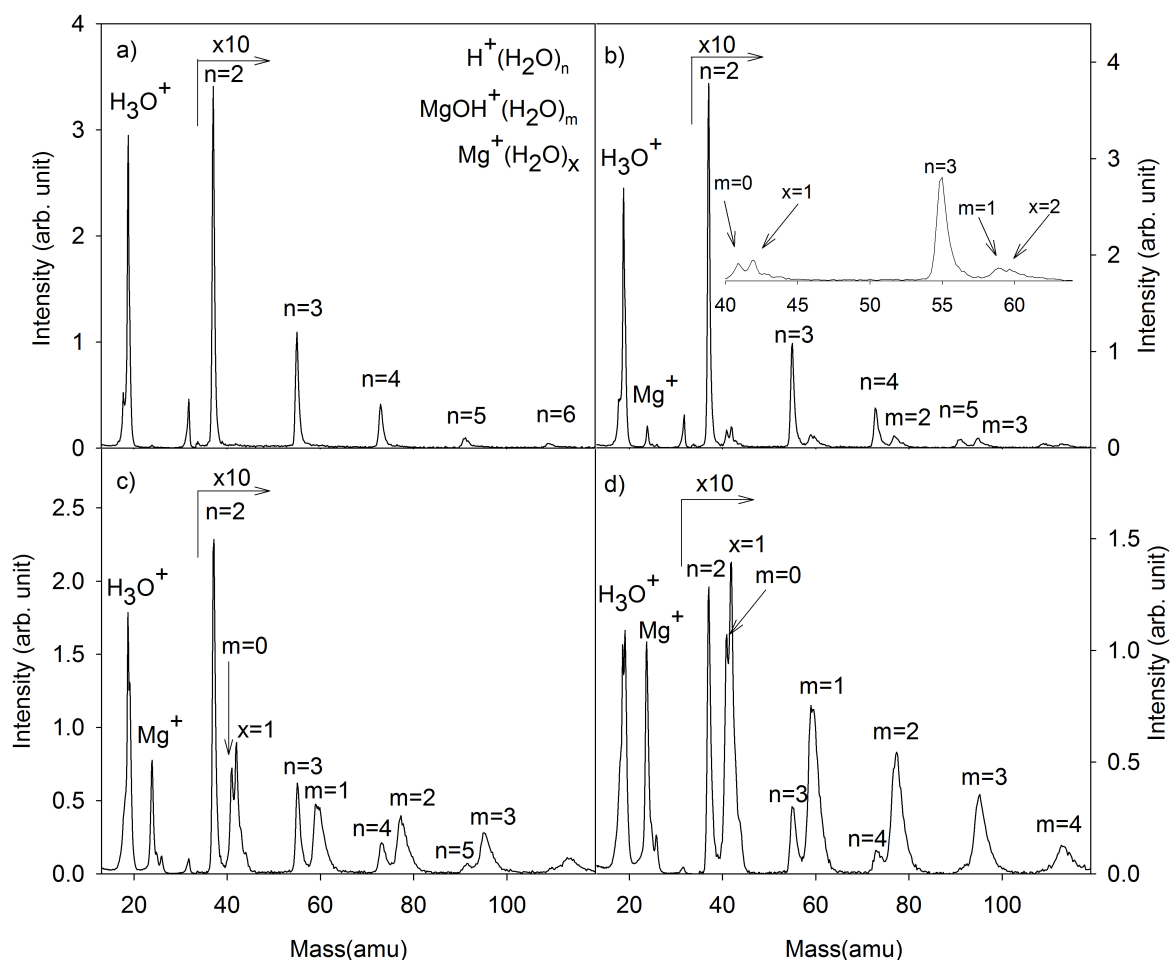


Figure 5.1: Time-of-flight mass spectrum of ions ejected during photoionization of $MgCl_2$ solution a) 10^{-4} M; b) 10^{-3} M; c) 5×10^{-3} M and d) 10^{-2} M. Cation clusters of the type $H^+(H_2O)_n$ ($n = 1-6$) $MgOH^+(H_2O)_m$ ($m = 0-4$) and $Mg^+(H_2O)_x$ ($x=1,2$) are observed.

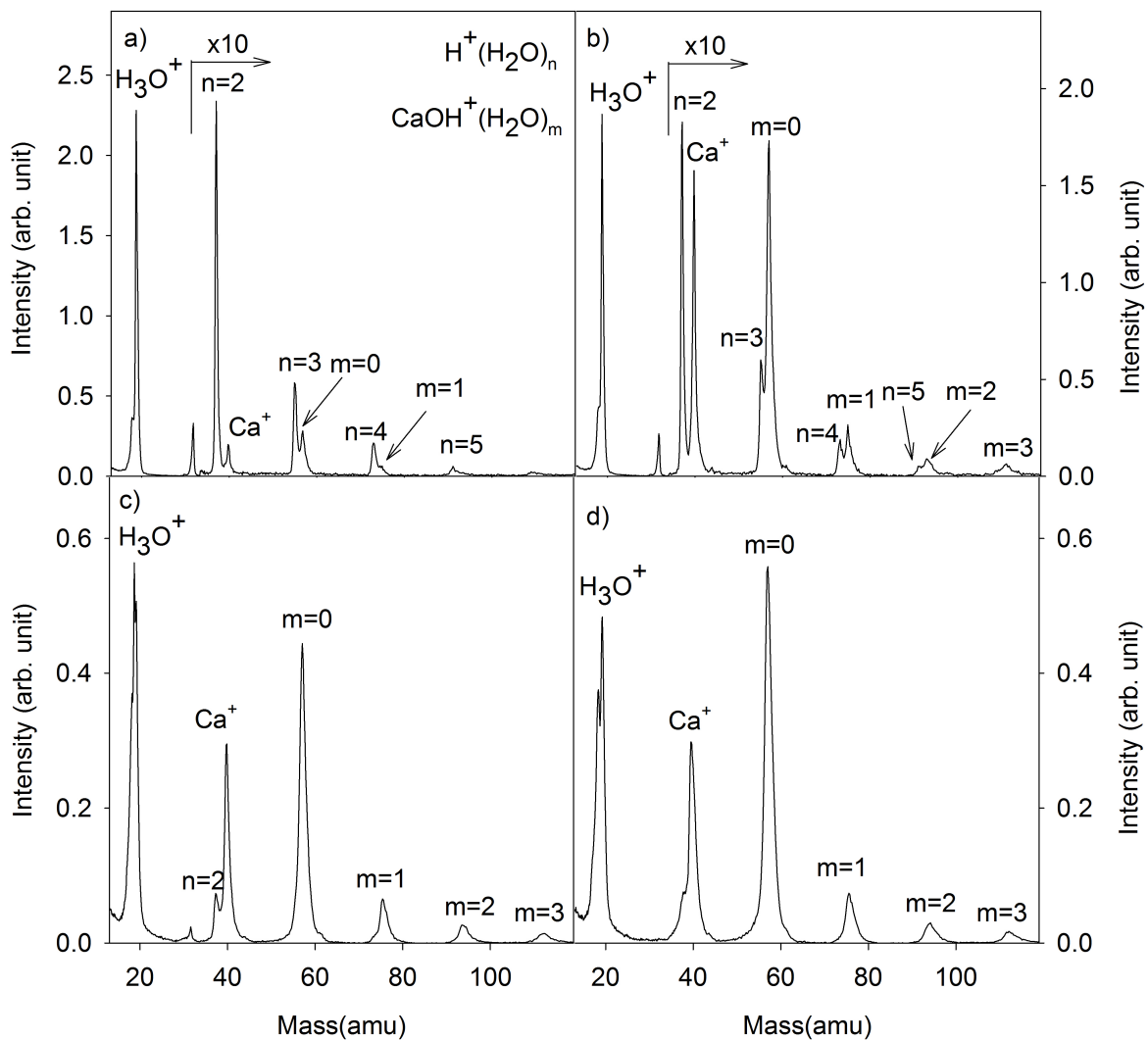


Figure 5.2: Time-of-flight mass spectrum of ions ejected during photoionization of CaCl_2 solution a) 10^{-4} M; b) 10^{-3} M; c) 5×10^{-3} M and d) 10^{-2} M. Cation clusters of the type $\text{H}^+(\text{H}_2\text{O})_n$ ($n = 1-6$) and $\text{CaOH}^+(\text{H}_2\text{O})_m$ ($m = 0-4$) are observed.

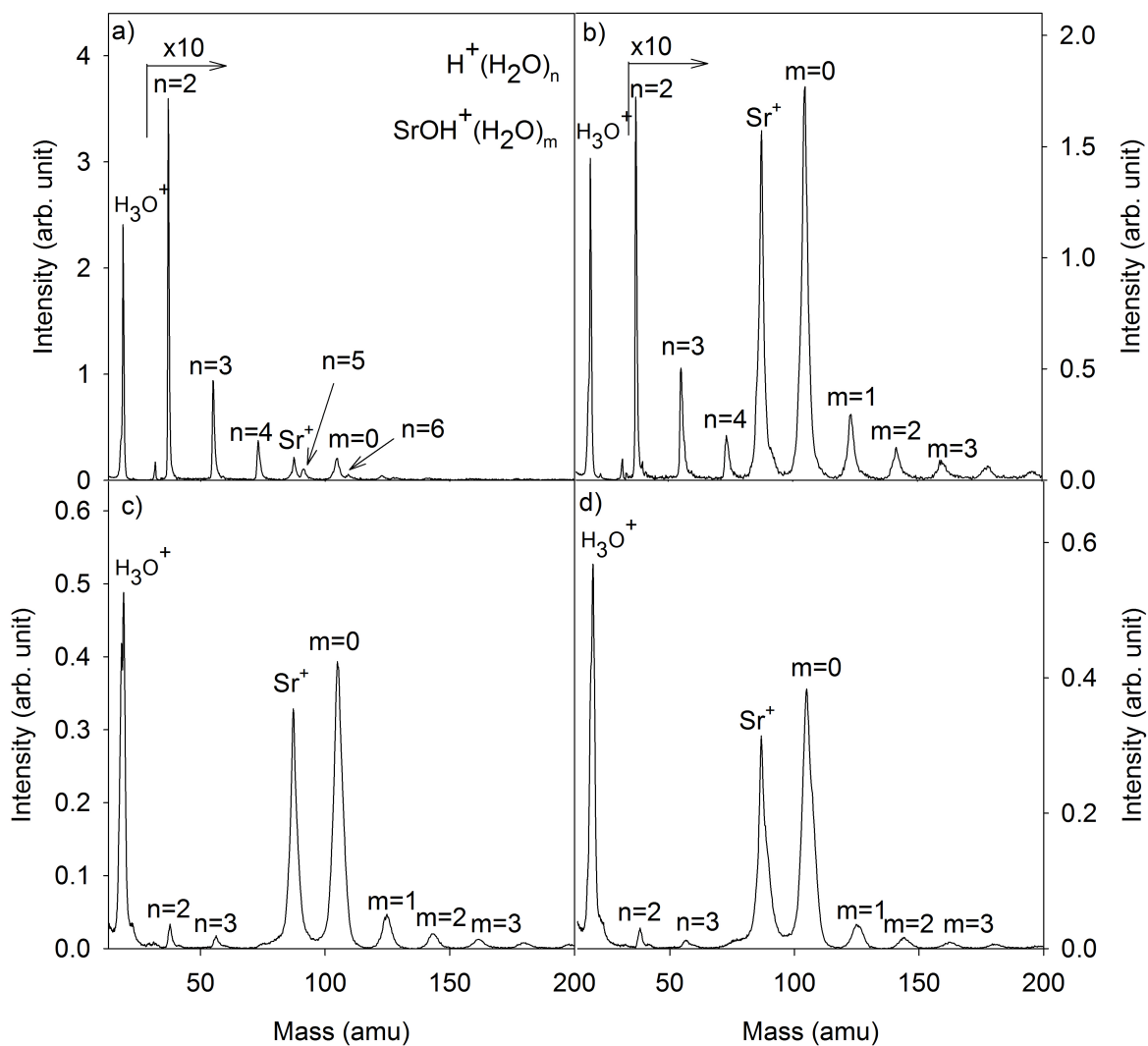


Figure 5.3: Time-of-flight mass spectrum of ions ejected during photoionization of SrCl_2 solution a) 10^{-4} M; b) 10^{-3} M; c) 5×10^{-3} M and d) 10^{-2} M. Cation clusters of the type $\text{H}^+(\text{H}_2\text{O})_n$ ($n = 1-4$) and $\text{SrOH}^+(\text{H}_2\text{O})_m$ ($m = 0-7$) are observed.

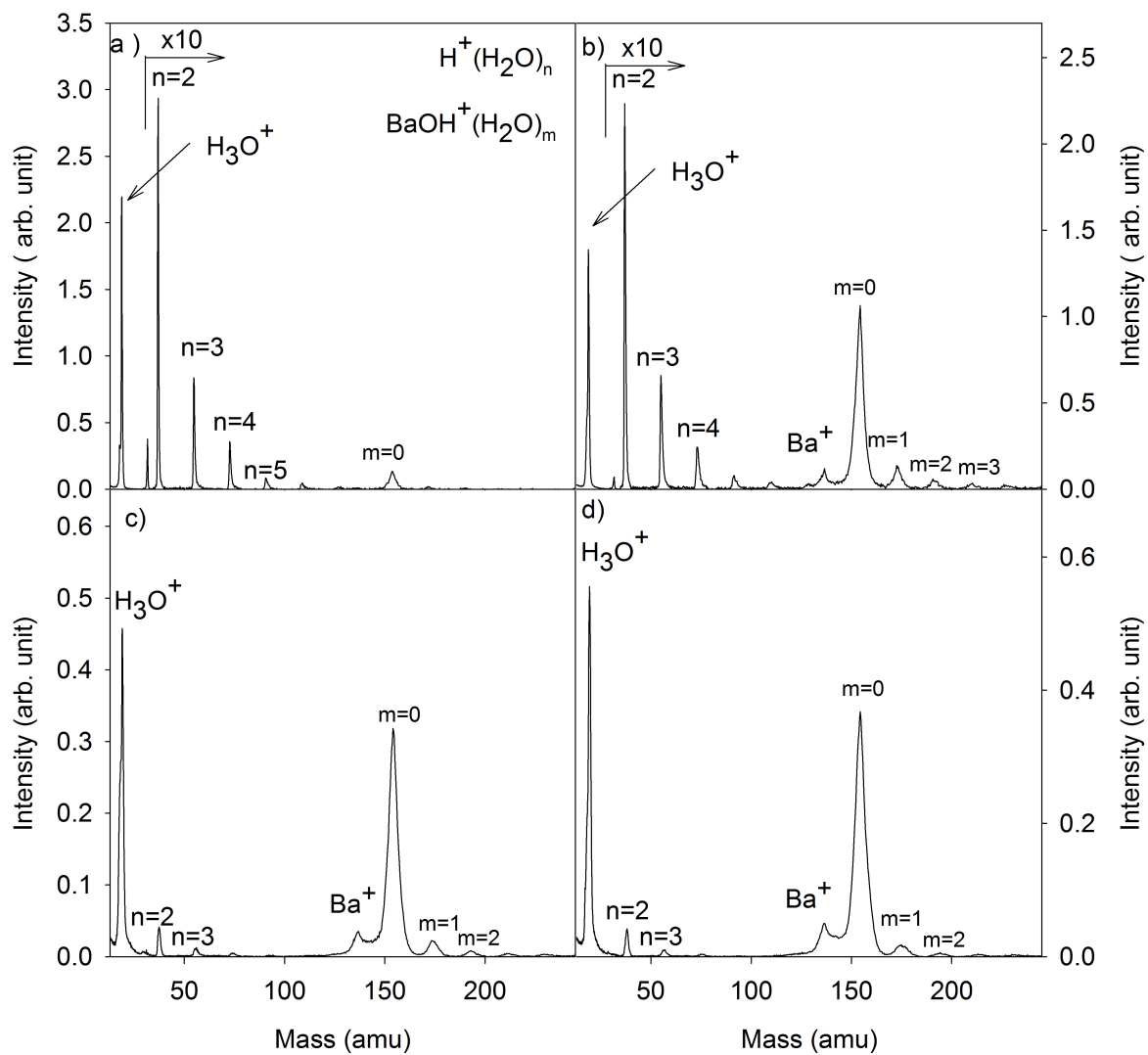


Figure 5.4: Time-of-flight mass spectrum of ions ejected during photoionization of BaCl_2 solution a) 10^{-4} M; b) 10^{-3} M; c) 5×10^{-3} M and d) 10^{-2} M. Cation clusters of the type $\text{H}^+(\text{H}_2\text{O})_n$ ($n = 1-4$) and $\text{BaOH}^+(\text{H}_2\text{O})_m$, ($m = 0-7$) are observed.

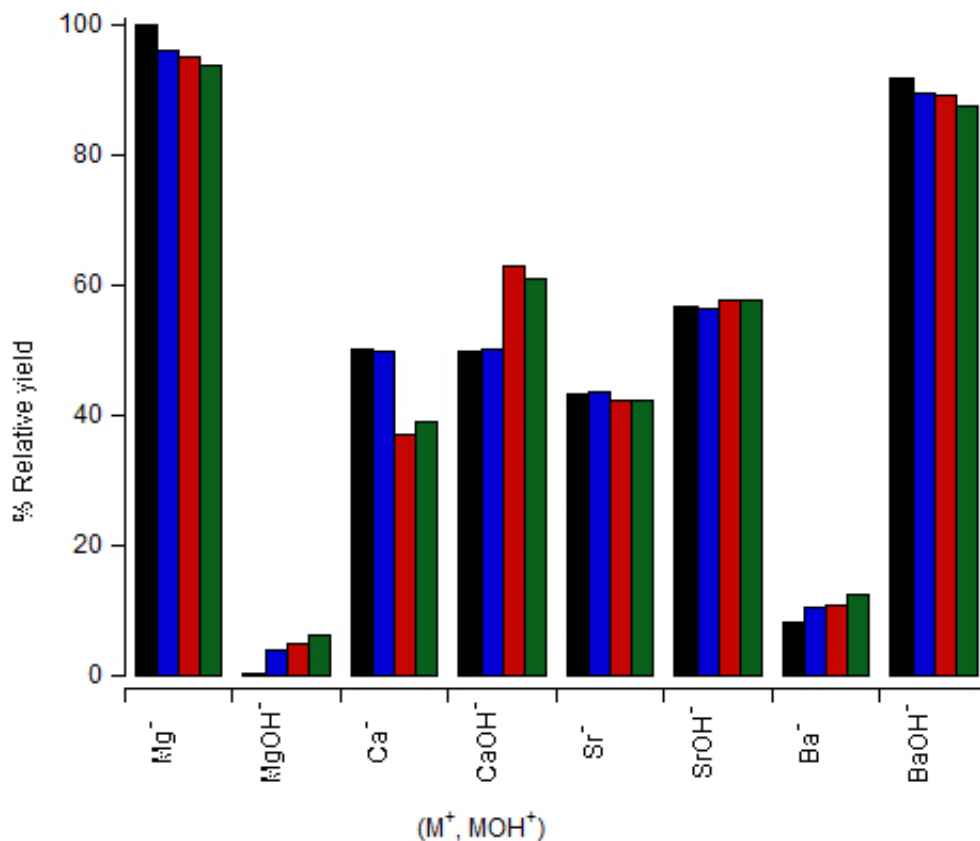


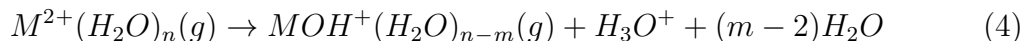
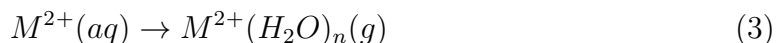
Figure 5.5: The relative yield of M^+ compared to MOH^+ . Mg gives mainly Mg^+ with a small $MgOH^+$. Approximately equal amount of M^+ and MOH^+ are observed for both Ca and Sr while Ba yields mainly $BaOH^+$ and a considerably small amount of Ba^+ . This trend appears to be independent of the salt concentration.

5.4 Discussion

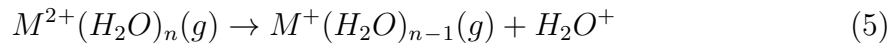
The ejection mechanism of ions observed in this experiment is similar to that discussed in Chapter 4. After electron depletion from the surface of the liquid jet during laser irradiation, ions are ejected into the gas phase due to the Coulomb repulsion of neighboring positive charges. H_3O^+ and protonated water cluster of the type $H^+(H_2O)_n$ decreases with concentration for all divalent ions investigated, a similar trend that was observed in Chapter 4. As the concentration of salt increases in the bulk, the amount of M^{2+} that migrates to the surface increases thereby decreasing the

amount of water molecules available on the surface during laser irradiation. Though the divalent metal ions studied are thought to assume a formal oxidation state of (+2) in aqueous solutions, ions ejected into the gas phase do not exhibit unsolvated M^{2+} or protonated water clusters of the type $M^{2+}(H_2O)_n$ in the TOF mass spectra. The calculated relative abundances of MOH^+ compared to M^{2+} in the bulk solution for all concentrations is negligible, therefore the observation of MOH^+ and $MOH^+(H_2O)_m$ is likely not representative of ions existing in the bulk. In gas phase measurement, the absence of $M^{2+}(H_2O)_n$ is justified by either an electron transfer process (when the second IP of metals are higher than the first IP of water) or by proton transfer process. Since ions in the bulk are stabilized by the ion-dipole interaction between the ion and the surrounding water molecules, charge transfer between M^{2+} and water molecules is not favored in liquid phase. However, if the ion is located on the surface of the liquid jet where the M^{2+} is not completely solvated then this local structure could favor similar charge/electron transfer processes observed in gas phase.

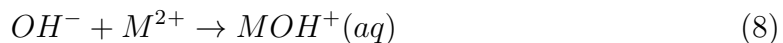
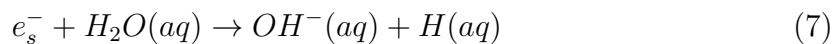
Laser induced Coulomb expulsion can cause ejected cluster ions to gain some internal energy subsequently resulting in dissociation of ejected $M^{2+}(H_2O)_n$ ions similar to that observed in the gas phase. [132] Just after leaving the surface of the liquid jet $M^{2+}(H_2O)_n$ can undergo proton transfer and dissociates into $MOH^+(H_2O)_m$ [133] as shown in reactions 3 and 4.



In contrast to other metals, Mg also undergoes electron transfer to give $Mg^+(H_2O)_x$, $x = 1, 2$ as shown in reaction 5. Electron transfer from neighboring water molecule to Mg^{2+} is energetically favorable and occurs spontaneously in gas phase [134] because the second IP of Mg^{2+} (15.6 eV) is larger than the first IP of water (12.6 eV).



The absence of unsolvated Mg^{2+} could also indicate the reduction of Mg^{2+} to M^+ by solvated electrons, e_s^- , generated by charge transfer to solvent (CTTS) band of Cl^- during laser irradiation (reaction 6).[135, 136] Also, the solvated electron reacts with H_2O to form OH^- which further reacts to form MOH^+ as shown below in reactions 7 and 8 :



According to Table 5.1, Mg^{2+} has the highest 2nd ionization potential and will react faster with solvated electron. The formation of MOH^+ therefore increases while the formation of M^+ decreases from Mg to Ba. Figure 5.5 shows there is a competition between the two processes.

Table 5.1: Second ionization potentials of alkaline-earth metal.

Element	Second IP,eV
Mg	15.6
Ca	11.9
Sr	11.0
Ba	10.0
$H_2O(g)^1$	12.6

5.5 Conclusion

Ion ejection from liquid jet surface by laser irradiation of aqueous solution of MCl_2 ($\text{M}=\text{Mg}$, Ca , Sr and Ba) have been studied by monitoring ejected ions using linear time of flight mass spectrometer. The observed ions were unsolvated ions (M^+ , MOH^+) and water clusters of the type $\text{MOH}^+(\text{H}_2\text{O})_m$, $\text{H}^+(\text{H}_2\text{O})_n$ and $\text{M}^+(\text{H}_2\text{O})_x$ (observed for aqueous solution of MgCl_2 only). The absence of unsolvated M^{2+} reveals the presence of solvated electron formed via the CTTS band of Cl^- during laser irradiation. The formation of $\text{MOH}^+(\text{H}_2\text{O})_m$ and $\text{M}^+(\text{H}_2\text{O})_x$ is justified by the energetics of the ejected ions in the gas phase. Although, the results presented represent the first time ions ejected from aqueous solutions of alkaline earth metal have been investigated without any gas phase collision induced fragmentation, further investigation is required to provide more insight into the predominant reactions that result in the ions detected by the time-of-flight mass spectrometer.

¹The first IP of $\text{H}_2\text{O}(\text{g})$ is added for comparison

CHAPTER VI

CONCLUSION

Heterogeneous reactions on Polar Stratospheric Cloud and sea salt aerosols found in the marine boundary layer have been implicated as a major source of ozone depletion episodes in the stratosphere and troposphere, respectively. Though the general importance of surface reactions on ice is well recognized; however, the fundamental and quantitative information concerning the non-thermal processes of adsorbates on ice is not fully understood. The low temperature ice studies provide the opportunity to investigate the effect morphology and hydrogen bonding network at the ice surface on the reactivity of adsorbates. The use of traditional surface science techniques limits the temperature range of ice that can be studied but by using the liquid jet technique the surface of aqueous solutions has been investigated. An attempt has been made to understand the nature of the vacuum-surface interface and the nature of ion solvation by monitoring the ejection of ions during laser irradiation of liquid jet.

Photodissociation dynamics of methyl iodide (CH_3I) adsorbed on both amorphous solid water (ASW) and porous amorphous solid water (PASW) has been investigated with the aim of understanding the effect of ice porosity on the release of neutral iodine species. The ejected ground state $\text{I}(^2\text{P}_{3/2})$ and excited state $\text{I}(^2\text{P}_{1/2})$ photofragments were detected using resonance enhanced multiphoton ionization (REMPI). Irradiating with either 260 nm or 290 nm produces iodine photofragments with complicated velocity distributions that depend upon the ice morphology. Temperature programmed desorption (TPD) results demonstrate that an increase in porosity enhances the ice's ability to trap adsorbed CH_3I molecules while pore-free ice enhances collisions of iodine containing surface precursors resulting in the formation of I_2 products. The

presence of an ice solid matrix also resulted in the ejection of iodine photofragments with higher kinetic energies compared to the gas phase photodissociation of CH_3I . The observed difference in photodissociation dynamics of condensed CH_3I compared to gas phase is ascribed to the enhancement of the ground state $\text{I}(^2\text{P}_{3/2})$ production compared to the excited state $\text{I}(^2\text{P}_{1/2})$ caused by the velocity and orientation of the I atoms from adsorbed CH_3I molecules on the ice surface.

The interaction and autoionization of HCl on low-temperature (80–140 K) water ice surfaces has also been studied using low-energy (5–250 eV) electron-stimulated desorption (ESD) and temperature programmed desorption (TPD). There is a reduction of H^+ and H_2^+ and a concomitant increase in $\text{H}^+(\text{H}_2\text{O})_n$, $n = 1\text{--}7$ ESD yields due to the presence of sub-monolayer quantities of HCl. These observed changes are as a result of reduction of dangling bonds and increased hole localization induced by the presence of HCl. This non-activated autoionization of HCl occurs at temperatures as low as 80 K; well below those typical of polar stratospheric cloud particles. The uptake and facile autoionization of HCl is further supported by TPD studies which show that for adsorbed HCl on ice, the desorption of HCl begins at 115 K and peaks at 180 K. The former is associated with adsorption of molecular HCl and is strongly dependent on the annealing history of the ice, the latter is commensurate with the desorption of HCl produced by recombinative desorption of solvated separated ion-pairs.

Photoionization of pure water and aqueous solutions of NaOH, NaCl, and HCl were also investigated using a liquid jet apparatus that injects a thin ($\sim 6\text{ }\mu\text{m}$) stream of liquid into vacuum. Ejected ions from laser irradiation of the liquid jet were monitored using a linear time-of-flight (TOF) mass spectrometer. Unsolvated hydronium ion (H_3O^+) and protonated water cluster ($\text{H}(\text{H}_2\text{O})_n$) were observed from photoionization of pure water and HCl solutions. Along with these ions, both unsolvated sodium

ion (Na^+) and sodium water clusters ($\text{Na}^+(\text{H}_2\text{O})_m$) were observed from photoionization of aqueous solutions of NaCl and NaOH. Both H_3O^+ and $\text{H}^+(\text{H}_2\text{O})_n$, ($n=2-6$) observed varied inversely with increasing concentration of NaOH and NaCl, but remained unchanged with HCl concentration. However, Na^+ and $\text{Na}^+(\text{H}_2\text{O})_m$ ($m=1-6$) observed increases with NaOH and NaCl concentration. These results are discussed in terms of the propensity of solvated Na^+ to migrate to the surface and distort the bulk hydrogen bond network of the bulk water molecules.

The direct monitoring of ions ejected from the surface of aqueous solution of alkaline-earth metal chloride (MCl , $\text{M}=\text{Mg}^{2+}$, Ca^{2+} , Sr^{2+} and Ba^{2+}) have also been investigated. The application of time of flight mass spectrometry to monitor ejection of ions during laser irradiation of liquid jet provides a novel way of probing hydrated divalent ions in aqueous phase without any interference of surrounding equilibrium vapor. The ejection of solvated divalent ions into gas phase without a subsequent collision induced fragmentation was investigated. A comparison of the TOF mass spectra with aqueous solutions containing monovalent cations presented in Chapter 4 shows a similar trend of decreasing yield of unsolvated H_3O^+ and protonated water clusters with concentration. Other ions ejected from MCl_2 solutions include unsolvated ions (M^+ and MOH^+) and water clusters of the type $\text{MOH}^+(\text{H}_2\text{O})_m$. In contrast to others, MgCl_2 solutions (at low concentrations) also yields water clusters of the type $\text{Mg}^+(\text{H}_2\text{O})_x$. The result obtained and the obvious absence of unsolvated M^{2+} and M^{2+} containing water clusters is explained in terms of the discontinuity of hydrogen bond network on the surface of the liquid jet, the presence of solvated electrons and the energetics of ions formed.

The research presented though fundamental, serves as a ground work for extensive investigation of both ice and aqueous liquid interface. The work presented should be extended to other halogenated organic compounds stable in both the stratosphere and the marine boundary layer. Also, detailed investigation of other acidic particles

(HBr, HNO₃ and H₂SO₄) and aqueous aerosols (brine solutions) co-deposited with ice on cold substrates should be carried out. A unique problem with surface science techniques and the use of ‘model environments’ is the subtle but important deviation from atmospheric ‘real world’ samples. Utilizing liquid phase/aerosol injection system compared to the gas phase dosing system used in the present study would help reduce this gap.

The liquid jet technique provides a very good probe of interfacial ion concentrations and the perturbations on the hydrogen bonding network on the surface of liquids. The use of electron stimulated desorption (ESD) would serve as a better probe (compared to photons) of interfacial reactions on liquids because of the low penetration depth of electrons. Investigation of electron-induced ion ejection from liquid jets as a function concentration, temperature of the jet and the presence of multiply charged cations (such as Mg²⁺, Ca²⁺) and anions (such as SO₄²⁻, PO₄²⁻) should be explored.

REFERENCES

- [1] U. Platt and G. Hönninger, “The role of halogen species in the troposphere,” *Chemosphere*, vol. 52, no. 2, pp. 325–338, 2003.
- [2] W. R. Simpson, R. Von Glasow, K. Riedel, P. Anderson, P. Ariya, J. Bottenheim, J. Burrows, L. Carpenter, U. Frieß, M. Goodsite, *et al.*, “Halogens and their role in polar boundary-layer ozone depletion,” *Atmospheric Chemistry and Physics Discussions*, vol. 7, no. 2, pp. 4285–4403, 2007.
- [3] T. Tang and J. C. McConnell, “Autocatalytic release of bromine from Arctic snow pack during polar sunrise,” *Geophysical Research Letters*, vol. 23, no. 19, pp. 2633–2636, 1996.
- [4] A. L. Swanson, N. J. Blake, J. E. Dibb, M. R. Albert, D. R. Blake, and F. Sherwood Rowland, “Photochemically induced production of CH_3Br , CH_3I , $\text{C}_2\text{H}_5\text{I}$, ethene, and propene within surface snow at Summit, Greenland,” *Atmospheric Environment*, vol. 36, no. 15-16, pp. 2671–2682, 2002.
- [5] D. R. Hanson, “Surface-specific reactions on liquids,” *Journal of Physical Chemistry B*, vol. 101, no. 25, pp. 4998–5001, 1997.
- [6] J. Boniface, Q. Shi, Y. Li, J. Cheung, O. V. Rattigan, P. Davidovits, D. R. Worsnop, J. T. Jayne, and C. E. Kolb, “Uptake of gas-phase SO_2 , H_2S , and CO_2 by aqueous solutions,” *Journal of Physical Chemistry A*, vol. 104, no. 32, pp. 7502–7510, 2000.
- [7] J. T. Jayne, P. Davidovits, D. R. Worsnop, M. S. Zahniser, and C. E. Kolb, “Uptake of sulfur dioxide (g) by aqueous surfaces as a function of pH: the effect of chemical reaction at the interface,” *The Journal of Physical Chemistry*, vol. 94, no. 15, pp. 6041–6048, 1990.
- [8] T. L. Tarbuck and G. L. Richmond, “Adsorption and Reaction of CO_2 and SO_2 at a Water Surface,” *Journal of the American Chemical Society*, vol. 128, no. 10, pp. 3256–3267, 2006.
- [9] D. R. Hanson and A. R. Ravishankara, “Reactive uptake of ClONO_2 onto sulfuric acid due to reaction with HCl and H_2O ,” *The Journal of Physical Chemistry*, vol. 98, no. 22, pp. 5728–5735, 1994.
- [10] M. A. Zondlo, P. K. Hudson, A. J. Prenni, and M. A. Tolbert, “Chemistry and microphysics of polar stratospheric clouds and cirrus clouds,” *Annual Review of Physical Chemistry*, vol. 51, no. 1, pp. 473–499, 2000.

- [11] J. G. Calvert and S. E. Lindberg, "Potential influence of iodine-containing compounds on the chemistry of the troposphere in the polar spring. I. Ozone depletion," *Atmospheric Environment*, vol. 38, no. 30, pp. 5087–5104, 2004.
- [12] I. W. M. Smith, "Laboratory studies of atmospheric reactions at low temperatures," *Chemical Reviews*, vol. 103, no. 12, pp. 4549–4564, 2003.
- [13] Y. Sohn, W. Wei, and J. M. White, "Thermal and photochemistry of tert-butyl iodide on ice films," *Surface Science*, vol. 602, no. 15, pp. 2706–2712, 2008.
- [14] Y. Lilach and M. Asscher, "Photochemistry of caged molecules: CD₃Cl@ Ice," *The Journal of Chemical Physics*, vol. 119, pp. 407–412, 2003.
- [15] M. L. Grecea, E. H. G. Backus, H. J. Fraser, T. Pradeep, A. W. Kleyn, and M. Bonn, "Mobility of haloforms on ice surfaces," *Chemical Physics Letters*, vol. 385, no. 3-4, pp. 244–248, 2004.
- [16] C. C. Perry, N. S. Faradzhev, T. E. Madey, and D. H. Fairbrother, "Electron stimulated reactions of methyl iodide coadsorbed with amorphous solid water," *The Journal of Chemical Physics*, vol. 126, pp. 2047011–20470114, 2007.
- [17] J. E. Schaff and J. T. Roberts, "Adsorbed states of acetonitrile and chloroform on amorphous and crystalline ice studied with X-ray photoelectron spectroscopy," *Surface Science*, vol. 426, no. 3, pp. 384–394, 1999.
- [18] Y. Sohn and J. M. White, "Thermal and Photochemistry of Methyl Iodide on Ice Film Grown on Cu (111)," *Bulletin of the Korean Chemical Society*, vol. 30, no. 7, pp. 1470–1474, 2009.
- [19] M. L. Grecea, E. H. G. Backus, A. W. Kleyn, and M. Bonn, "Surface photochemistry of bromoform on ice: cross section and competing reaction pathways," *Journal of Physical Chemistry B*, vol. 109, no. 37, pp. 17574–17578, 2005.
- [20] M. L. Grecea, E. H. G. Backus, A. W. Kleyn, and M. Bonn, "Adsorption and photochemistry of multilayer bromoform on ice," *Surface Science*, vol. 600, no. 16, pp. 3337–3344, 2006.
- [21] J. Herring, A. Aleksandrov, and T. M. Orlando, "Stimulated desorption of cations from pristine and acidic low-temperature water ice surfaces," *Physical Review Letters*, vol. 92, no. 18, pp. 1876021–1876024, 2004.
- [22] V. Sadtchenko, K. Knutsen, C. F. Giese, and W. R. Gentry, "Interactions of CCl₄ with Thin D₂O Amorphous Ice Films, Part I: A Nanoscale Probe of Ice Morphology," *Journal of Physical Chemistry B*, vol. 104, no. 11, pp. 2511–2521, 2000.
- [23] H. Kang, T. H. Shin, S. Park, I. K. Kim, and S. J. Han, "Acidity of Hydrogen Chloride on Ice," *Journal of the American Chemical Society*, vol. 122, no. 40, pp. 9842–9843, 2000.

- [24] P. U. Andersson, M. B. Nagard, and J. B. C. Pettersson, “Molecular beam studies of HCl interactions with pure and HCl-covered ice surfaces,” *Journal of Physical Chemistry B*, vol. 104, no. 7, pp. 1596–1601, 2000.
- [25] S. C. Park and H. Kang, “Adsorption, ionization, and migration of hydrogen chloride on ice films at temperatures between 100 and 140 K,” *Journal of Physical Chemistry B*, vol. 109, no. 11, pp. 5124–5132, 2005.
- [26] S. F. Banham, J. R. Sodeau, A. B. Horn, M. R. S. McCoustra, and M. A. Chesters, “Adsorption and ionization of HCl on an ice surface,” *Journal of Vacuum Science & Technology A: Vacuum, Surfaces, and Films*, vol. 14, no. 3, pp. 1620–1626, 2009.
- [27] L. Delzeit, B. Rowland, and J. P. Devlin, “Infrared spectra of hydrogen chloride complexed/ionized in amorphous hydrates and at ice surfaces in the 15-90 K range,” *The Journal of Physical Chemistry*, vol. 97, no. 40, pp. 10312–10318, 1993.
- [28] H. A. Donsig and J. C. Vickerman, “Dynamic and static secondary ion mass spectrometry studies of the solvation of HCl by ice,” *Journal of the Chemical Society, Faraday Transactions*, vol. 93, no. 16, pp. 2755–2761, 1997.
- [29] J. D. Graham and J. T. Roberts, “Interaction of hydrogen chloride with an ultrathin ice film: Observation of adsorbed and absorbed states,” *The Journal of Physical Chemistry*, vol. 98, no. 23, pp. 5974–5983, 1994.
- [30] J. Harnett, S. Haq, and A. Hodgson, “Desorption from thin films of amorphous HCl hydrate,” *Surface Science*, vol. 532, pp. 478–482, 2003.
- [31] S. Haq, J. Harnett, and A. Hodgson, “Adsorption and solvation of HCl into ice surfaces,” *Journal of Physical Chemistry B*, vol. 106, no. 15, pp. 3950–3959, 2002.
- [32] M. J. Isakson and G. O. Sitz, “Adsorption and Desorption of HCl on ice,” *Journal of Physical Chemistry A*, vol. 103, no. 13, pp. 2044–2049, 1999.
- [33] M. Faubel, S. Schlemmer, and J. P. Toennies, “A molecular beam study of the evaporation of water from a liquid jet,” *Zeitschrift für Physik D Atoms, Molecules and Clusters*, vol. 10, no. 2, pp. 269–277, 1988.
- [34] M. Faubel and B. Steiner, “Strong bipolar electrokinetic charging of thin liquid jets emerging from 10 μm PtIr nozzles,” *Berichte der Bunsengesellschaft für physikalische Chemie*, vol. 96, no. 9, pp. 1167–1172, 1992.
- [35] B. Winter and M. Faubel, “Photoemission from liquid aqueous solutions,” *Chemical Reviews*, vol. 106, no. 4, pp. 1176–1211, 2006.

- [36] B. Winter, R. Weber, I. V. Hertel, M. Faubel, P. Jungwirth, E. C. Brown, and S. E. Bradforth, "Electron binding energies of aqueous alkali and halide ions: EUV photoelectron spectroscopy of liquid solutions and combined ab initio and molecular dynamics calculations," *Journal of the American Chemical Society*, vol. 127, no. 19, pp. 7203–7214, 2005.
- [37] B. Winter, R. Weber, W. Widdra, M. Dittmar, M. Faubel, and I. V. Hertel, "Full valence band photoemission from liquid water using EUV synchrotron radiation," *Journal of Physical Chemistry A*, vol. 108, no. 14, pp. 2625–2632, 2004.
- [38] R. Weber, B. Winter, P. M. Schmidt, W. Widdra, I. V. Hertel, M. Dittmar, and M. Faubel, "Photoemission from Aqueous Alkali-Metal- Iodide Salt Solutions Using EUV Synchrotron Radiation," *Journal of Physical Chemistry B*, vol. 108, no. 15, pp. 4729–4736, 2004.
- [39] K. R. Wilson, B. S. Rude, T. Catalano, R. D. Schaller, J. G. Tobin, and R. J. Saykally, "X-ray spectroscopy of liquid water microjets," *Journal of Physical Chemistry B*, vol. 105, no. 17, pp. 3346–3349, 2001.
- [40] K. R. Wilson, B. S. Rude, J. Smith, C. Cappa, R. D. Schaller, M. Larsson, T. Catalano, and R. J. Saykally, "Investigation of volatile liquid surfaces by synchrotron x-ray spectroscopy of liquid microjets," *Review of Scientific Instruments*, vol. 75, pp. 725–736, 2004.
- [41] B. M. Messer, C. D. Cappa, J. D. Smith, W. S. Drisdell, C. P. Schwartz, R. C. Cohen, and R. J. Saykally, "Local hydration environments of amino acids and dipeptides studied by X-ray spectroscopy of liquid microjets," *Journal of Physical Chemistry B*, vol. 109, no. 46, pp. 21640–21646, 2005.
- [42] A. Charvat and B. Abel, "How to make big molecules fly out of liquid water: applications, features and physics of laser assisted liquid phase dispersion mass spectrometry," *Physical Chemistry Chemical Physics*, vol. 9, no. 26, pp. 3335–3360, 2007.
- [43] A. Wattenberg, F. Sobott, H. D. Barth, and B. Brutschy, "Studying noncovalent protein complexes in aqueous solution with laser desorption mass spectrometry," *International Journal of Mass Spectrometry*, vol. 203, no. 1-3, pp. 49–57, 2000.
- [44] T. Kondow and F. Mafuné, "Structures and dynamics of molecules on liquid beam surfaces," *Annual Review of Physical Chemistry*, vol. 51, no. 1, pp. 731–761, 2000.
- [45] L. M. Dobeck, D. E. Otten, M. A. Buntine, G. F. Metha, and W. L. Holstein, "Ultraviolet laser irradiation of low concentration liquid microjets: Solute evaporation and solvent initiated reactivity," *Australian Journal of Chemistry*, vol. 56, no. 5, pp. 481–487, 2003.

- [46] J. F. Black and I. Powis, "Photofragment investigations of the 280 nm photodissociation of methyl iodide using REMPI atom detection," *Chemical Physics*, vol. 125, no. 2-3, pp. 375–388, 1988.
- [47] J. F. Black and I. Powis, "Competing ionization and dissociation of methyl iodide in the one-photon A-band region," *Chemical Physics Letters*, vol. 148, no. 6, pp. 479–485, 1988.
- [48] D. M. Szaflarski and M. A. El-Sayed, "Kinetic energy and formation mechanisms of I^+ and CH_3^+ from 266-nm picosecond versus nanosecond laser multiphoton absorption," *The Journal of Physical Chemistry*, vol. 92, no. 8, pp. 2234–2239, 1988.
- [49] Y. Jiang, M. R. Giorgi-Arnazzi, and R. B. Bernstein, "Concurrent photodissociation and multiphoton ionization processes in CH_3I from 266–307 nm," *Chemical Physics*, vol. 106, no. 1, pp. 171–178, 1986.
- [50] A. M. Woodward, S. D. Colson, W. A. Chupka, and M. G. White, "Vibrational analysis of the $\tilde{A}-X^{\sim}$ photodissociation spectrum of CH_3I^+ ," *The Journal of Physical Chemistry*, vol. 90, no. 2, pp. 274–278, 1986.
- [51] G. N. A. Van Veen, T. Baller, and N. J. A. De Vries, "The excitation of the umbrella mode of CH_3 and CD_3 formed from photodissociation of CH_3I and CD_3I at 248 nm," *Chemical Physics*, vol. 87, no. 3, pp. 405–417, 1984.
- [52] A. B. Alekseyev, H. P. Liebermann, R. J. Buenker, and S. N. Yurchenko, "An ab initio study of the CH_3I photodissociation. I. Potential energy surfaces," *The Journal of Chemical Physics*, vol. 126, no. 23, pp. 2341021–23410211, 2007.
- [53] G. Li and H. J. Hwang, "State-to-state correlated study of CD_3I photodissociation at 266 and 304 nm," *The Journal of chemical Physics*, vol. 124, pp. 2443061–2443068, 2006.
- [54] G. Li, Y. K. Shin, and H. J. Hwang, "State-to-state reaction dynamics of CH_3I photodissociation at 304 nm," *Journal of Physical Chemistry A*, vol. 109, no. 41, pp. 9226–9231, 2005.
- [55] S. R. Coon, K. B. Myli, and V. H. Grassian, "Photoproduct characterization and dynamics in the 248 nm photolysis of CH_3I thin films on Ag (111)," *The Journal of Physical Chemistry*, vol. 99, no. 44, pp. 16416–16424, 1995.
- [56] D. H. Fairbrother, K. A. Briggman, P. C. Stair, and E. Weitz, "Molecular Orientation and Surface Morphology in Methyl Iodide Films Grown on MgO (100) Probed by Photodissociation," *The Journal of Physical Chemistry*, vol. 98, no. 49, pp. 13042–13049, 1994.
- [57] S. J. Garrett, V. P. Holbert, P. C. Stair, and E. Weitz, "The adsorption and photochemistry of CD_3I on TiO_2 (110)," *The Journal of Chemical Physics*, vol. 100, no. 6, pp. 4615–4625, 1994.

- [58] S. J. Garrett, V. P. Holbert, P. C. Stair, and E. Weitz, "Wavelength dependence of the photodissociation and photodesorption of CD_3I adsorbed on the TiO_2 (110) surface," *The Journal of Chemical Physics*, vol. 100, no. 6, pp. 4626–4636, 1994.
- [59] V. P. Holbert, S. J. Garrett, P. C. Stair, and E. Weitz, "The photochemistry of CD_3I adsorbed on the TiO_2 (110) surface," *Surface Science*, vol. 346, no. 1-3, pp. 189–205, 1996.
- [60] E. T. Jensen, "Near-UV photodissociation of oriented CH_3I adsorbed on Cu (110)–I," *The Journal of chemical physics*, vol. 123, pp. 2047091–2047098, 2005.
- [61] S. H. Kim, K. A. Briggman, P. C. Stair, and E. Weitz, "Photoreactions of methyl iodide multilayers on the TiO_2 (110) surface," *Journal of Vacuum Science and Technology-Section A-Vacuum Surfaces and Films*, vol. 14, no. 3, pp. 1557–1561, 1996.
- [62] S. H. Kim, P. C. Stair, and E. Weitz, "UV-induced desorption of CH_3X ($\text{X}=\text{I}$ and Br)/ TiO_2 (110)," *Journal of Chemical Physics*, vol. 108, pp. 5080–5088, 1998.
- [63] A. Srivastava and R. M. Osgood Jr, "State-resolved dynamics of 248 nm methyl-iodide fragmentation on GaAs (110)," *The Journal of Chemical Physics*, vol. 119, pp. 10298–10306, 2003.
- [64] X. L. Zhou and J. M. White, "Alkyl halide photochemistry on Ag (111):: III. Methyl iodide," *Surface Science*, vol. 241, no. 3, pp. 270–278, 1991.
- [65] L. J. Carpenter, "Iodine in the marine boundary layer," *Chemical Reviews*, vol. 103, no. 12, pp. 4953–4962, 2003.
- [66] Y. J. Jung, Y. S. Kim, W. K. Kang, and K. H. Jung, "Photoelectron imaging spectroscopy for $(2+1)$ resonance-enhanced multiphoton ionization of atomic iodine produced from A-band photolysis of CH_3I ," *The Journal of Chemical Physics*, vol. 107, pp. 7187–7193, 1997.
- [67] R. S. Smith, C. Huang, E. K. L. Wong, and B. D. Kay, "The molecular volcano: abrupt CCl_4 desorption driven by the crystallization of amorphous solid water," *Physical Review Letters*, vol. 79, no. 5, pp. 909–912, 1997.
- [68] C. D. Lane and T. M. Orlando, "Low-energy electron stimulated desorption of neutrals from multilayers of SiCl_4 on Si (111)," *The Journal of Chemical Physics*, vol. 124, pp. 1647021–1647029, 2006.
- [69] J. L. Blanchard and J. T. Roberts, "Interaction of CCl_4 with the Surface of Amorphous Ice," *Langmuir*, vol. 10, no. 9, pp. 3303–3310, 1994.

- [70] V. Sadtchenko, K. Knutsen, C. F. Giese, and W. R. Gentry, "Interactions of CCl_4 with Thin D_2O Amorphous Ice Films. 2. Variation of Desorption Kinetics with Ice Preparation Conditions and Evidence for Distinct Structures of Low-Density Amorphous Ice," *Journal of Physical Chemistry B*, vol. 104, no. 20, pp. 4894–4902, 2000.
- [71] A. T. J. B. Eppink and D. H. Parker, "Energy partitioning following photodissociation of methyl iodide in the A band: A velocity mapping study," *The Journal of Chemical Physics*, vol. 110, pp. 832–844, 1999.
- [72] F. M. Zimmermann and W. Ho, "State resolved studies of photochemical dynamics at surfaces," *Surface Science Reports*, vol. 22, no. 4-6, pp. 127–247, 1995.
- [73] T. M. Orlando, A. B. Aleksandrov, and J. Herring, "Electron-Stimulated Desorption of H^+ , H_2^+ , OH^+ , and $\text{H}^+(\text{H}_2\text{O})_n$ from Water-Covered Zirconia Surfaces," *Journal of Physical Chemistry B*, vol. 107, no. 35, pp. 9370–9376, 2003.
- [74] D. P. Woodruff and T. A. Delchar, *Modern techniques of surface science*. Cambridge Univ Pr, 1994.
- [75] N. Timneanu, C. Caleman, J. Hajdu, and D. Van Der Spoel, "Auger electron cascades in water and ice," *The journal of Chemical Physics*, vol. 299, no. 2-3, pp. 277–283, 2004.
- [76] D. Ajitha, M. Wierzbowska, R. Lindh, and P. A. Malmqvist, "Spin-orbit ab initio study of alkyl halide dissociation via electronic curve crossing," *The Journal of Chemical Physics*, vol. 121, pp. 5761–5766, 2004.
- [77] M. I. McCarthy, R. B. Gerber, K. A. Trentelman, P. Strupp, D. H. Fairbrother, P. C. Stair, and E. Weitz, "Photodissociation dynamics of CH_3I adsorbed on MgO (100): Theory and experiment," *The Journal of Chemical Physics*, vol. 97, pp. 5168–5176, 1992.
- [78] A. T. J. B. Eppink and D. H. Parker, "Methyl iodide A-band decomposition study by photofragment velocity imaging," *The Journal of Chemical Physics*, vol. 109, pp. 4758–4767, 1998.
- [79] D. H. Fairbrother, K. A. Briggman, P. C. Stair, and E. Weitz, "The role of adsorbate structure in the photodissociation dynamics of adsorbed species: Methyl iodide/ MgO (100)," *The Journal of Chemical Physics*, vol. 102, pp. 7267–7276, 1995.
- [80] F. L. Tabares, E. P. Marsh, G. A. Bach, and J. P. Cowin, "Laser photofragmentation and photodesorption of physisorbed CH_3Br on lithium fluoride," *The Journal of Chemical Physics*, vol. 86, pp. 738–744, 1987.

- [81] J. Kutzner, G. Lindeke, K. H. Welge, and D. Feldmann, “Dissociative desorption from CH_3I by ultraviolet-laser radiation,” *The Journal of Chemical Physics*, vol. 90, pp. 548–555, 1989.
- [82] Z. H. Huang and H. Guo, “The orientation of adsorbed methyl halides on a LiF (001) surface: A Monte Carlo study,” *The Journal of Chemical Physics*, vol. 98, pp. 7412–7419, 1993.
- [83] Z. H. Huang and H. Guo, “Theoretical modeling of photodissociation dynamics of CH_3I on LiF (001),” *The Journal of Chemical Physics*, vol. 98, pp. 3395–3409, 1993.
- [84] G. Vaidyanathan, M. Y. M. Lykтей, J. J. Stry, R. L. DeLeon, and J. F. Garvey, “Production of I_2^+ from methyl iodide: ion-molecule reactions under multiple collision conditions vs cluster chemistry,” *The Journal of Physical Chemistry*, vol. 98, no. 31, pp. 7475–7478, 1994.
- [85] V. Buch, J. Sadlej, N. Aytemiz-Uras, and J. P. Devlin, “Solvation and Ionization Stages of HCl on Ice Nanocrystals,” *Journal of Physical Chemistry A*, vol. 106, no. 41, pp. 9374–9389, 2002.
- [86] F. Bournel, C. Mangeney, M. Tronc, C. Laffon, and P. Parent, “Acidity of hydrogen chloride at the surface of low-temperature (40–150 K) water-ice films,” *Physical Review B*, vol. 65, no. 20, pp. 2014041–2014044, 2002.
- [87] B. J. Gertner and J. T. Hynes, “Molecular dynamics simulation of hydrochloric acid ionization at the surface of stratospheric ice,” *Science*, vol. 271, no. 5255, pp. 1563–1566, 1996.
- [88] K. Bolton, “A QM/MM study of HCl adsorption at ice surface defect sites,” *Journal of Molecular Structure: THEOCHEM*, vol. 632, no. 1-3, pp. 145–156, 2003.
- [89] M. T. Sieger, W. C. Simpson, and T. M. Orlando, “Production of O_2 on icy satellites by electronic excitation of low-temperature water ice,” *Nature*, vol. 394, no. 6693, pp. 554–556, 1998.
- [90] M. T. Sieger, W. C. Simpson, and T. M. Orlando, “Electron-stimulated desorption of D^+ from D_2O ice: Surface structure and electronic excitations,” *Physical Review B*, vol. 56, no. 8, pp. 4925–4937, 1997.
- [91] T. M. Orlando and G. A. Kimmel, “The role of excitons and substrate temperature in low-energy (5–50 eV) electron-stimulated dissociation of amorphous D_2O ice,” *Surface Science*, vol. 390, no. 1-3, pp. 79–85, 1997.
- [92] J. Herring-Captain, G. A. Grieves, A. Alexandrov, M. T. Sieger, H. Chen, and T. M. Orlando, “Low-energy (5–250eV) electron-stimulated desorption of H^+ , H_2^+ , and $\text{H}^+(\text{H}_2\text{O})_n$ from low-temperature water ice surfaces,” *Physical Review B*, vol. 72, no. 3, pp. 354311–3543110, 2005.

- [93] M. T. Sieger and T. M. Orlando, “Effect of surface roughness on the electron-stimulated desorption of D^+ from microporous D_2O ice,” *Surface Science*, vol. 390, no. 1-3, pp. 92–96, 1997.
- [94] M. Akbulut, T. E. Madey, and P. Nordlander, “Low energy (<5 eV) F^+ and F^- ion transmission through condensed layers of water,” *The Journal of Chemical Physics*, vol. 106, pp. 2801–2810, 1997.
- [95] K. H. Tan, C. E. Brion, P. E. Van der Leeuw, and M. J. Van der Wiel, “Absolute oscillator strengths (10-60 eV) for the photoabsorption, photoionisation and fragmentation of H_2O_s ,” *Chemical Physics*, vol. 29, no. 3, pp. 299–309, 1978.
- [96] M. N. Piancastelli, A. Hempelmann, F. Heiser, O. Gessner, A. Rüdél, and U. Becker, “Resonant photofragmentation of water at the oxygen K edge by high-resolution ion-yield spectroscopy,” *Physical Review A*, vol. 59, no. 1, pp. 300–306, 1999.
- [97] H. Rottke, C. Trump, and W. Sandner, “Multiphoton ionization and dissociation of H_2O ,” *Journal of Physics B: Atomic, Molecular and Optical Physics*, vol. 31, pp. 1083–1096, 1998.
- [98] J. Bernholc and J. C. Phillips, “Kinetics of cluster formation in the laser vaporization source: Carbon clusters,” *The Journal of Chemical Physics*, vol. 85, pp. 3258–3267, 1986.
- [99] R. Scott Smith, C. Huang, E. Wong, and B. Kay, “Desorption and crystallization kinetics in nanoscale thin films of amorphous water ice,” *Surface Science*, vol. 367, no. 1, pp. L13–L18, 1996.
- [100] M. Svanberg, J. B. C. Pettersson, and K. Bolton, “Coupled QM/MM Molecular Dynamics Simulations of HCl Interacting with Ice Surfaces and Water Clusters—Evidence of Rapid Ionization,” *J. Phys. Chem. A*, vol. 104, no. 24, pp. 5787–5798, 2000.
- [101] V. Sadtschenko, C. F. Giese, and W. R. Gentry, “Interaction of hydrogen chloride with thin ice films: The effect of ice morphology and evidence for unique surface species on crystalline vapor-deposited ice,” *Journal of Physical Chemistry B*, vol. 104, no. 40, pp. 9421–9429, 2000.
- [102] J. D. Graham and J. T. Roberts, “Formation of $HCl \cdot 6H_2O$ from ice and HCl under ultrahigh vacuum,” *Chemometrics and Intelligent Laboratory Systems*, vol. 37, no. 1, pp. 139–148, 1997.
- [103] J. Harnett, S. Haq, and A. Hodgson, “Uptake and reaction of $ClONO_2$ on water ice and HCl trihydrate at low temperatures,” *Journal of Physical Chemistry A*, vol. 106, no. 40, pp. 9226–9232, 2002.

- [104] P. A. Thiel and T. E. Madey, “The interaction of water with solid surfaces: fundamental aspects,” *Surface Science Reports*, vol. 7, no. 6-8, pp. 211–385, 1987.
- [105] W. Kuch, W. Schnurnberger, M. Schulze, and K. Bolwin, “Equilibrium determination of H₂O desorption kinetic parameters of H₂O/K/Ni(111),” *The Journal of chemical physics*, vol. 101, no. 2, pp. 1687–1692, 1994.
- [106] J. W. He and P. R. Norton, “Interaction of water with a Pd (110) surface, studied by thermal desorption spectroscopy, LEED and $\Delta\varphi$,” *Surface science*, vol. 238, no. 1-3, pp. 95–104, 1990.
- [107] P. Jungwirth and D. J. Tobias, “Ions at the air/water interface,” *Journal of Physical Chemistry B*, vol. 106, no. 25, pp. 6361–6373, 2002.
- [108] J. H. Kim, T. Shin, K. H. Jung, and H. Kang, “Direct observation of segregation of sodium and chloride ions at an ice surface,” *ChemPhysChem*, vol. 6, no. 3, pp. 440–444, 2005.
- [109] G. A. Grieves, N. Petrik, J. Herring-Captain, B. Olanrewaju, A. Aleksandrov, R. G. Tonkyn, S. A. Barlow, G. A. Kimmel, and T. M. Orlando, “Photoionization of Sodium Salt Solutions in a Liquid Jet,” *The Journal of Physical Chemistry C*, vol. 112, no. 22, pp. 8359–8364, 2008.
- [110] B. Winter, R. Weber, P. M. Schmidt, I. V. Hertel, M. Faubel, L. Vrbka, and P. Jungwirth, “Molecular Structure of Surface-Active Salt Solutions: Photoelectron Spectroscopy and Molecular Dynamics Simulations of Aqueous Tetra-butylammonium Iodide,” *Journal of Physical Chemistry B*, vol. 108, no. 38, pp. 14558–14564, 2004.
- [111] A. Charvat, A. Bógehold, and B. Abel, “Time-resolved micro liquid desorption mass spectrometry: Mechanism, features, and kinetic applications,” *Australian Journal of Chemistry*, vol. 59, no. 2, pp. 81–103, 2006.
- [112] J. Kohno, F. Mafune, and T. Kondow, “Mechanisms of Ion Ejection from Liquid Beam under Irradiation of Laser by Simultaneous Detection of Ions Produced inside a Liquid Beam and Ejected into a Vacuum,” *Journal of Physical Chemistry A*, vol. 104, no. 2, pp. 243–248, 2000.
- [113] C. G. Elles, A. E. Jailaubekov, R. A. Crowell, and S. E. Bradforth, “Excitation-energy dependence of the mechanism for two-photon ionization of liquid H₂O and D₂O from 8.3 to 12.4 eV,” *The Journal of Chemical Physics*, vol. 125, no. 4, pp. 0445151–04451512, 2006.
- [114] K. R. Siefermann, Y. Liu, E. Lugovoy, O. Link, M. Faubel, U. Buck, B. Winter, and B. Abel, “Binding energies, lifetimes and implications of bulk and interface solvated electrons in water,” *Nature Chemistry*, vol. 2, pp. 274–279, 2010.

- [115] P. Atkins, "Physical chemistry. 1994."
- [116] S. Bouazizi, S. Nasr, N. Jaïdane, and M. Bellissent-Funel, "Local order in aqueous NaCl solutions and pure water: X-ray scattering and molecular dynamics simulations study," *Journal of Physical Chemistry B*, vol. 110, no. 46, pp. 23515–23523, 2006.
- [117] F. Mafuné, J. Kohno, T. Nagata, and T. Kondow, "Mechanism of ion ejection from a liquid beam following laser photoionization," *Chemical Physics Letters*, vol. 218, no. 1-2, pp. 7–12, 1994.
- [118] J. W. Christiansen, I. S. T. Tsong, and S. H. Lin, "Ion-induced desorption of $(\text{H}_2\text{O})\text{NH}^+$ ion clusters," *The Journal of Chemical Physics*, vol. 86, pp. 4701–4705, 1987.
- [119] S. H. Nam, H. S. Park, M. A. Lee, N. R. Cheong, J. K. Song, and S. M. Park, "Photoinduced evaporation of mass-selected aniline (water) $_n$ ($n= 4\text{--}20$) clusters," *The Journal of chemical physics*, vol. 126, pp. 2243021–2243029, 2007.
- [120] O. Echt, D. Kreisle, M. Knapp, and E. Recknagel, "Evolution of magic numbers in mass spectra of water clusters," *Chemical Physics Letters*, vol. 108, no. 4, pp. 401–407, 1984.
- [121] N. N. Casillas-Ituarte, K. M. Callahan, C. Y. Tang, X. Chen, M. Roeselová, D. J. Tobias, and H. C. Allen, "Surface organization of aqueous MgCl_2 and application to atmospheric marine aerosol chemistry," *Proceedings of the National Academy of Sciences*, vol. 107, no. 15, pp. 6616–6621, 2010.
- [122] K. M. Callahan, N. N. Casillas-Ituarte, M. Xu, M. Roeselová, H. Allen, and D. J. Tobias, "Effect of magnesium cation on the interfacial properties of aqueous salt solutions," *The journal of Physical Chemistry. A*, vol. 114, no. 32, pp. 8359–8368, 2010.
- [123] K. M. Callahan, N. N. Casillas-Ituarte, M. Roeselova, H. C. Allen, and D. J. Tobias, "Solvation of magnesium dication: molecular dynamics simulation and vibrational spectroscopic study of magnesium chloride in aqueous solutions," *The Journal of Physical Chemistry A*, vol. 114, no. 15, pp. 5141–5148, 2010.
- [124] M. Xu, R. Spinney, and H. C. Allen, "Water Structure at the Air- Aqueous Interface of Divalent Cation and Nitrate Solutions," *The Journal of Physical Chemistry B*, vol. 113, no. 13, pp. 4102–4110, 2009.
- [125] A. T. Blades, P. Jayaweera, M. G. Ikonou, and P. Kebarle, "Studies of alkaline earth and transition metal M gas phase ion chemistry," *The Journal of Chemical Physics*, vol. 92, pp. 5900–5906, 1990.
- [126] N. Okai, H. Ishikawa, and K. Fuke, "Hydration process of alkaline-earth metal atoms in water clusters," *Chemical Physics Letters*, vol. 415, no. 1-3, pp. 155–160, 2005.

- [127] G. N. Merrill, S. P. Webb, and D. B. Bivin, "Formation of Alkali Metal/Alkaline Earth Cation Water Clusters, $M(\text{H}_2\text{O})_{(1-6)}$, $M = \text{Li}^+, \text{Na}^+, \text{K}^+, \text{Mg}^{2+}$, and Ca^{2+} : An Effective Fragment Potential (EFP) Case Study," *Journal of Physical Chemistry A*, vol. 107, no. 3, pp. 386–396, 2003.
- [128] J. P. Larentzos and L. J. Criscenti, "A Molecular Dynamics Study of Alkaline Earth Metal- Chloride Complexation in Aqueous Solution," *The Journal of Physical Chemistry B*, vol. 112, no. 45, pp. 14243–14250, 2008.
- [129] M. Sanekata, F. Misaizu, K. Fuke, S. Iwata, and K. Hashimoto, "Reactions of singly charged alkaline-earth metal ions with water clusters: Characteristic size distribution of product ions," *Journal of the American Chemical Society*, vol. 117, no. 2, pp. 747–754, 1995.
- [130] M. Peschke, A. T. Blades, and P. Kebarle, "Hydration Energies and Entropies for Mg^{2+} , Ca^{2+} , Sr^{2+} , and Ba^{2+} from Gas-Phase Ion- Water Molecule Equilibria Determinations," *Journal of Physical Chemistry A*, vol. 102, no. 48, pp. 9978–9985, 1998.
- [131] E. D. Glendening and D. Feller, "Dication- Water Interactions: $\text{M}^{2+}(\text{H}_2\text{O})_n$ Clusters for Alkaline Earth Metals $M = \text{Mg}, \text{Ca}, \text{Sr}, \text{Ba}$, and Ra ," *The Journal of Physical Chemistry*, vol. 100, no. 12, pp. 4790–4797, 1996.
- [132] M. Beyer, E. R. Williams, and V. E. Bondybey, "Unimolecular reactions of dihydrated alkaline earth metal dications $\text{M}^{2+}(\text{H}_2\text{O})_2$, $M = \text{Be}, \text{Mg}, \text{Ca}, \text{Sr}$, and Ba : salt-bridge mechanism in the proton-transfer reaction $\text{M}^{2+}(\text{H}_2\text{O})_2 \rightarrow \text{MOH}^+ + \text{H}_3\text{O}^+$," *Journal of the American Chemical Society*, vol. 121, no. 7, pp. 1565–1573, 1999.
- [133] J. Kohno, F. Mafune, and T. Kondow, "Cluster Ion Formation from Alcohol Solutions of CaI_2 ," *Journal of Physical Chemistry A*, vol. 103, no. 11, pp. 1518–1522, 1999.
- [134] A. A. Shvartsburg and K. W. M. Siu, "Is there a minimum size for aqueous doubly charged metal cations?," *Journal of the American Chemical Society*, vol. 123, no. 41, pp. 10071–10075, 2001.
- [135] J. Kohno, F. Mafune, and T. Kondow, "Formation of $\text{Ca}^+(\text{EtOH})_m$ from Alcohol Solutions of CaCl_2 ," *Journal of Physical Chemistry A*, vol. 104, no. 6, pp. 1079–1084, 2000.
- [136] D. Majumdar, J. Kim, and K. S. Kim, "Charge transfer to solvent (CTTS) energies of small $\text{X}^-(\text{H}_2\text{O})_{n=1-4}$ ($\text{X} = \text{F}, \text{Cl}, \text{Br}, \text{I}$) clusters: Ab initio study," *Journal of Chemical Physics*, vol. 112, pp. 101–105, 2000.